Topside Ionosphere/Plasmasphere Tomography Using Space-Borne Dual Frequency Gps Receivers

Pinto Jayawardena, Talini

Award date:
2015

Awarding institution:
University of Bath

TOPSIDE IONOSPHERE/PLASMASPHERE TOMOGRAPHY USING SPACE-BORNE DUAL FREQUENCY GPS RECEIVERS

Talini S. Pinto Jayawardena

A thesis submitted for the degree of Doctor of Philosophy

University of Bath

Department of Electronic and Electrical Engineering

April 2015

COPYRIGHT

Abstract

This research demonstrates the potential of novel technology for space-based remote sensing of the topside ionosphere-plasmasphere, supported by ionospheric imaging, which can augment and enhance our current understanding of the Earth's plasmasphere.

The research was conducted in two phases. The first was the development of a technology demonstrator 'TOPCAT' that installed a dual-frequency GPS receiver dedicated for topside ionosphere-plasmasphere imaging into a Low Earth Orbit (LEO). The novelties of TOPCAT were that it was designed from commercial-off-the-shelf (COTS) components and was installed on-board the CubeSat 'UKube-1', greatly reducing development and launch costs of the instrument. The successful launch of TOPCAT for space-borne remote sensing of the topside ionosphere and plasmasphere could provide the necessary proof of concept for the installation of a constellation of CubeSats – a possible next phase that may be implemented in the future. Thus, in its first stage, the thesis discusses the development of TOPCAT, together with design challenges encountered from constraints imposed by CubeSat technology. The discussion also includes the series of qualification tests performed to successfully qualify TOPCAT as a space-worthy payload design that can remotely image regions beyond the ionosphere.

The second phase of research was the validation of the Multi-Instrument Data Analysis System (MIDAS) for the topside ionosphere and plasmasphere. A tomography algorithm originally developed for the ionosphere, MIDAS uses total electron content (TEC) measurements from differential phase of GPS signals, and inverts them to derive the electron density of the region. The thesis investigates the extension of MIDAS to image regions beyond the ionosphere by validating the algorithm for the topside ionosphere and plasmasphere. The process was carried out by first reconstructing a simulation by Gallagher et al. [1988] to verify the quality of the images. This was followed by the use of real GPS phase data from the COSMIC constellation to reconstruct the topside ionosphere-plasmasphere, and the qualitative comparison of the images with previous independent observations obtained through COSMIC and Jason-1 missions. Results showed that MIDAS can successfully reconstruct the undisturbed (quiet) topside

ionosphere-plasmasphere using COSMIC data. However, imaging the storm-time topside ionosphere-plasmasphere requires better data coverage (i.e. more receivers) as the resolution offered by COSMIC was not sufficient to reconstruct fast-evolving structures – thereby emphasising the need for more data sources providing high resolution global coverage, such as a constellation of CubeSats with LEO-based GPS receivers.

Acknowledgements

I would like to thank a number of people whose contribution and assistance was invaluable for this research.

I wish to express my most sincere gratitude to my supervisor, Prof Cathryn Mitchell, whose patience, understanding and constant support and guidance made this thesis possible.

Thank you to Dr Robert Watson and Dr Nathan Smith for finding the time to lend their expertise during my research. I also wish to extend my appreciation to my friends and colleagues of the Invert group for their support, particularly during the development and test phases of TOPCAT.

I thank Ms Chelsey Cooper and Mr Andrew Bacon for their timely support in proof-reading my thesis.

I am particularly grateful for the assistance provided by Mr Mark Jessop and Prof Christopher Coleman from the University of Adelaide, Australia, and Dr Paolo Spalla from Instituto de Fisica, Italy during the development phase of TOPCAT; and Ms Jamie Lee and Mr Dave Parker for their timely actions during much needed design modifications. Thank you to Prof Allan Weatherwax and Mr Joe Kujawski of Siena College, Albany for the provision of much needed resources and guidance during ground testing.

Special thanks are extended to Mr Berend Winter and Mr Alex Rousseau at MSSL, and Mr Jiri Hofman and Dr Richard Sharp at Synergy Health PLC for facilitating vibration/thermal/vacuum tests and radiation tests, respectively, that were crucial to qualify the TOPCAT design as space-ready.

I also acknowledge the UK Space Agency (UKSA) who enabled and oversaw the UKube-1 project, and Clyde Space Ltd., responsible for the development of the satellite platform.

Finally, I wish to thank my parents and sister for their advice, constant guidance and encouragement throughout my PhD. Your support was greatly appreciated.

Table of Contents

Abstract i

Acknowledgements iii

List of Figures viii

List of Tables x

List of Abbreviations xi

List of Symbols xiv

1 Introduction 1

2 The Solar-Terrestrial Environment 4

2.1 Introduction 4

2.2 The Solar Wind and the IMF 4

2.2.1 The Solar Wind 4

2.2.2 The Interplanetary Magnetic Field 6

2.3 The Geomagnetic Field 6

2.3.1 Particle Retention (Trapped Particles) 8

2.3.2 Azimuthal Drift and the L-Parameter 9

2.4 The Magnetosphere 11

2.4.1 The Structure of the Magnetosphere 11

2.4.2 Current Systems 13

2.4.2.1 Ring Current 14

2.4.2.2 Field-Aligned (Birkeland) Currents 15

2.4.3 Magnetic Reconnection 15

2.5 Summary 17

3 The Ionised Upper Atmosphere 18

3.1 Introduction 18

3.2 The Topside Ionosphere 18

3.2.1 The Light Ion Trough 20
3.3 The Plasmasphere 22
3.3.1 Morphology of the Plasmasphere 24
3.4 Recent Observations of the Topside Ionosphere and Plasmasphere 27
3.4.1 CHAMP 29
3.4.2 COSMIC 30
3.4.3 Jason-1 34
3.5 Summary 36
4 Ionospheric Imaging with GPS 38
4.1 Introduction 38
4.2 An Introduction to GPS 38
4.2.1 Ionospheric Effects on GPS Signals 40
4.3 Ionospheric (TEC) Tomography 42
4.4 Ionospheric Tomography with MIDAS 45
4.5 Summary 49
5 TOPCAT – In-Situ Imaging of the Topside Ionosphere and Plasmasphere 51
5.1 Introduction 51
5.2 UKube-1 52
5.3 Payload Design 54
5.3.1 Power and Control Hardware 55
5.3.1.1 Power 55
5.3.1.2 The Microcontroller 56
5.3.2 The Communication System & Signal Servicing 57
5.3.3 Operational Procedure and Firmware 58
5.3.4 Mechanical Design 61
5.4 Design Challenges 61
5.4.1 Antenna Performance and Installation in UKube-1 62

5.4.2 Conformity of Receiver and Antenna Specifications 63
5.4.3 Timing Conflicts between Communication Buses 64
5.5 Space Qualification of TOPCAT 64
5.5.1 Vibration Testing 66
5.5.1.1 Results 67
5.5.1.2 Discussion 71
5.5.2 Thermal/Vacuum (T/V) Testing 71
5.5.2.1 Results 73
5.5.2.2 Discussion 74
5.5.3 Radiation Testing 75
5.5.3.1 Results 76
5.5.3.2 Discussion 77
5.6 Summary and Conclusion 78
6 Topside Ionosphere-Plasmasphere Imaging with MIDAS 80
6.1 Introduction 80
6.2 MIDAS for the Topside Ionosphere-Plasmasphere 81
6.3 Validation of MIDAS for the Topside Ionosphere-Plasmasphere 82
6.3.1 Reconstruction of the Gallagher Model 83
6.3.1.1 Method 84
6.3.1.2 Results 85
6.3.2 Reconstruction of the Topside Ionosphere-Plasmasphere 89
6.3.2.1 Method 89
6.3.2.2 Results 90
6.4 Discussion 95
6.5 Summary and Conclusion 96
7 Conclusions & Future Work 98
References 103

Appendix 1 – TOPCAT Design Documents 110

A1.1 Schematic and PCB Layout 111

A1.2 Parameter and Error Handling 114

A1.3 Data Packet Breakdown 119

A1.4 Hardware Design Challenges 125

Appendix 2 – Test Results 130

A2.1 Mechanical Vibration Test Results 131

A2.2 Thermal/Vacuum Test Results 155

List of Figures

Figure 2.1. A real-time coronagraph from the instrument LASCO C3 of the SOHO satellite. 5

Figure 2.2. Factors contributing to particle retention by closed magnetic field lines [*Hargreaves*, 1992] 9

Figure 2.3. Illustration of the motion of particles trapped by closed geomagnetic fields [*SPENVIS*, 2013] 11

Figure 2.4. An illustration of the Earth's magnetosphere, with the main particle regions highlighted [*Reiff*, 1999] 12

Figure 2.5. The structure of the magnetosphere 14

Figure 2.6. Current systems in the polar regions 15

Figure 2.7. Dayside and nightside magnetic reconnection [*COMET et al.*, 2004a][1] 16

Figure 3.1. Light ion (H+/He+) and electron density distribution in the topside ionosphere 22

Figure 3.2. Electron density distribution and plasma flow at the plasmapause/plasmatrough 24

Figure 3.3. An EUV image of the plasmasphere from the IMAGE satellite showing a distinct dusk-side plasma bulge and tail [Credit: B.Sandel and T. Forrester, University of Arizona]. 26

Figure 3.4. Images taken by the NASA IMAGE satellite showing several structures within the plasmasphere [*Gallagher*, 2005b] 27

Figure 3.5. Plasmaspheric signatures derived from ground GPS receivers 28

Figure 3.6. 2-D electron density map of the ionosphere and plasmasphere, produced from CHAMP TEC data assimilated for a period of one full orbit [*Heise et al.*, 2002]. 30

Figure 3.7. Longitudinal variations for the year 2008 observed by COSMIC over equatorial magnetic latitudes (±10°) above 800 km [*Pedatella et al.*, 2011]. 32

Figure 3.8. COSMIC observation of a wave 4 longitudinal structure seen during September equinox [*Pedatella et al.*, 2011] 33

Figure 3.9. Reconstruction of the global plasmaspheric electron density with and without IMF disturbances [*Spencer and Mitchell*, 2011] 34

Figure 4.1. The GPS satellite constellation, as produced by Lockheed Martin Corp [*Kaplan and Hegarty*, 2006]. 39

Figure 4.2. The concept of ionospheric tomography 43
Figure 4.3. Grid-based tomography implemented in MIDAS 47
Figure 4.4. 3-D mapping of the ionosphere for October 30, 2003, 2100 UT using MIDAS [Mitchell et al.]. 49
Figure 5.1. UKube-1 ready to be shipped to the launch site. [Credit: Clyde Space Ltd.] .. 54
Figure 5.2. TOPCAT architecture and design 55
Figure 5.3. Detailed operational architecture of TOPCAT and its interaction with the OBC. 60
Figure 5.4. Evolution of the mechanical design of the aluminium shield, antenna and antenna housing 63
Figure 5.5. TOPCAT secured on the shaker for vibration tests. 67
Figure 5.6. Vibration test results for x-axis 68
Figure 5.7. Vibration test results for y-axis 70
Figure 5.8. Vibration test results for z-axis 71
Figure 5.9. Profile of the thermal cycling specifications for T/V testing [*Greenland and Warren*, 2011]. 72
Figure 5.10. TOPCAT under preparation for T/V testing 73
Figure 5.11. TOPCAT thermal profile during T/V testing 74
Figure 5.12. TID radiation test results for TOPCAT 76
Figure 6.1. Simulated average electron concentration by MIDAS of the topside ionosphere and plasmasphere over 3 hours for ±90° geomagnetic latitude at two time steps described by the Gallagher model 84
Figure 6.2. 3-hour reconstructions of the Gallagher simulation 86
Figure 6.3. 1-hour reconstructions of the Gallagher simulation 87
Figure 6.4. Comparison of the percentage error between the simulation and reconstruction for 3-hour and 1-hour mean TEC at two instances on 22 May 2009 89
Figure 6.5. Seasonal TEC maps showing variation with local time 91
Figure 6.6. Average TEC distribution over the year 2009 92
Figure 6.7. Variation in annual TEC with longitude for the year 2009 93
Figure 6.8. Longitudinal and L-shell variations in TEC for June and December 94
Figure 6.9. Diurnal and seasonal variations in TEC with longitude 95

List of Tables

Table 5.1. Operational modes of TOPCAT 58

Table 5.2. Dimensions and clearances around TOPCAT displaying the small profile..... 61

Table 5.3. Vibration test specifications as determined by the launch providers. 66

Table 5.4. Thermal specifications for T/V testing. 72

List of Abbreviations

2-D	2-Dimensional
3-D	3-Dimensional
4-D	4-Dimensional
ADCS	Attitude Determination and Control System
AL	Acceptance Level
AMSAT-UK	Radio Amateur Satellite Corporation – UK
BatV	Unregulated battery rail
C/A	Coarse/Acquisition
C3D	Compact CMOS Camera Demonstrator
CDMA	Code Division Multiple Access
CERTO	Coherent Electromagnetic Radio Tomography
CHAMP	Challenging Minisatellite Payload
COSMIC	Constellation Observing System for Meteorology, Ionosphere, and Climate
COTS	Commercial-off-the-shelf
CT	Computer Tomography
DE-1	Dynamics Explorer-1
Dst	Disturbance storm time
EEPROM	Electrically Erasable Programmable Read-Only Memory
EOFs	Empirical Orthonormal Functions
ESA	European Space Agency
EUV	Extreme Ultra Violet
GNSS	Global Navigation Satellite System
GPS	Global Positioning System
GPS-RO	Global Positioning System-Radio Occultation
HE	High Energy
Hrs (or hrs)	Hours
IFB	Inter-Frequency Biases
IGS	International GNSS Service
IMF	Interplanetary Magnetic Field

LASCO C3	Large Angle and Spectrometric Coronagraph Experiment – visible spectrum imaging from 3.7 to 32 solar radii
LEO	Low Earth Orbit
LIT	Light Ion Trough
LOS	Line-Of-Sight
LT	Local Time
MEO	Medium Earth Orbit
MIDAS	Multi Instrument Data Analysis System
MLI	Multi-Layer Insulation
MLT	Magnetic Local Time
MSSL	Mullard Space Science Laboratory
NASA	National Aeronautics and Space Administration
NIMS	Navy Ionosphere Monitoring System
NNSS	Navy Navigation Satellite System
OBC	On-Board Computer
oTEC	Occultation TEC
PIM	Parameterized Ionospheric Model
POD	Precise Orbit Determination
PRN	Pseudo-Random Number
PRT	Platinum Resistor Thermometer
PVT	Position, Velocity and Timing
QL	Qualification Level
RAM	Random Access Memory
RIMS	Retarding Ion Mass Spectrometer
RO	Radio-Occultation
SED	Storm Enhanced Density
SEEs	Single Event Effects
SEUs	Single Event Upsets
SOHO	Solar and Heliospheric Observatory
sTEC	Slant TEC
T/V	Thermal/Vacuum
TEC	Total Electron Content

TECu or TECU	TEC Unit
TID	Total Ionising Dose
TOPCAT	TOPside ionosphere and plasmasphere Computer Assisted Tomography
TRN	True Random Number
UCAR	University Corporation for Atmospheric Research
UCL	University College London
UHF	Ultra High Frequency
UKSA	UK Space Agency
UT	Universal Time
UTH	Upper Transition Height
VHF	Very High Frequency
vTEC	Vertical TEC
WDT	Watchdog Timer

List of Symbols

λ	Geomagnetic latitude
ϕ	Geomagnetic longitude
Λ	Geographic latitude
Φ	Geographic longitude
Λ_0	Geographic latitude of geomagnetic north pole in 2010 (80.0°N)
Φ_0	Geographic longitude of geomagnetic north pole in 2010 (72.2°W)
B	Magnetic intensity or magnetic flux density (T)
H_0	Tangential component of the equatorial magnetic potential (T)
R_E (or R_E)	Radius of the Earth (or surface radius) (m)
r	Radial distance from the centre of the Earth (m)
ML_i	Magnetic longitude of the point of interest
ML_{ant}	Magnetic longitude of the antipode of the sub-solar point
ω_B	Angular gyrofrequency (rad/s)
e	Electronic charge (C)
m_p	Mass of the particle (kg)
R	Radial distance from the centre of the Earth in earth radii units (R_E)
L (or L)	L-shell parameter (R_E)
μ_0	Magnetic permeability of free space (Hm^{-1})
N_p	Particle density (m^{-3})
k	Boltzmann constant (JK^{-1})
T	Plasma temperature (K)
B_T	Total magnetic flux density in the magnetosphere (T)
B_d	Geomagnetic flux density (T)
B_{rc}	Flux density induced by the ring current (T)
B_{tail}	Flux density induced by the cross-tail current (T)
B_{mpause}	Flux density induced by the magnetopause (Chapman-

	Ferraro) current (T)
B_{FAC}	Flux density induced by the field-aligned currents (T)
Dst	Disturbance storm time index
N_e	Electron density (m^{-3})
N_0	Reference electron density (m^{-3})
g_0	Acceleration due to gravity at the Earth's surface (m/s^2)
m_+	Mean ion mass (kg)
z'	Height as a geopotential altitude (km)
K_P	Global geomagnetic storm (Planetary K) index
K	Geomagnetic storm index
L_{PP}	L-value of the plasmapause
$K_{P_{max}}$	Maximum K_P in the 24 hours before measurements
E x B	Charged particle drift experienced due to perpendicular external electric and magnetic fields
B_Z	Component of the interplanetary magnetic field parallel to the Earth's magnetic North (T) (i.e. z-component in solar magnetic coordinates)
B_Y	Component of the interplanetary magnetic field perpendicular to the plane of the dipole axis and the Earth-Sun line (T) (i.e. y-component in solar magnetic coordinates)
F10.7	Solar radio flux per unit frequency at a wavelength = 10.7 cm (SFU)
L1 and L1C	GPS frequency at 1575.42 MHz. L1C – L1 Civil for civilian applications
L2 and L2C	GPS frequency at 1227.6 MHz. L2C – L2 Civil for civilian applications
L5	GPS frequency at 1176 MHz
$n\ (n_1, n_2)$	Refractive index (refractive index for frequency 1 and 2, respectively)
c	Velocity of light in free space (m/s)
v	Propagation velocity of the electromagnetic wave (m/s)
v_p	Velocity of the signal carrier phase (i.e. phase velocity) (m/s)

v_g	Velocity of the modulating information signal (i.e. group velocity) (m/s)
n_p	Phase refractive index
n_g	Group refractive index
f	Carrier frequency of the transmitted signal (Hz)
a	Ionospheric dispersion constant = $40.3N_e$ (Hz^2)
Tx	Transmitter
Rx	Receiver
θ (and θ_1, θ_2)	Phase of signal propagating between Tx and Rx (phase of signals 1 and 2, respectively) (rad)
ds	Straight line path element between Tx and Rx (m)
t	Time (s)
ψ (and ψ_1, ψ_2)	Phase constant (phase constant of signals 1 and 2, respectively)
Θ	Differential phase from two transmitted signals (rad)
f_r	Reference frequency (Hz)
p	Integer constant relating f_r to transmitted signal 1
q	Integer constant relating f_r to transmitted signal 2
f_p	Plasma frequency (Hz)
m_e	Mass of an electron (kg)
ε_0	Permittivity of free space (F/m)
A	Ionospheric dispersion constant = 80.6 (m^3/s^2)
c_{cal}	Calibration constant for TEC
i	Vertical TEC elements calculated from observed slant TEC (TECU)
j	Number of voxels
$\boldsymbol{b}$	Vector of i vertical TEC (TECU)
$\mathbf{A}$	Matrix of ray path geometry
$\boldsymbol{x}$	Column vector of j components of electron concentration in each voxel (m^{-3})
$\boldsymbol{c}$	Unknown cycle offset in each voxel
$\mathbf{X}$	Mapping matrix of empirical orthonormal basis functions

	(EOFs)
$\boldsymbol{w}$	Unknown relative contribution of the basis functions
$\boldsymbol{\Delta TEC}$	Observed change in TEC within the voxel
$\mathbf{D}$	Difference in ray path geometry at consecutive time intervals
$\boldsymbol{y}$	Unknown change in electron concentration with time
α	Euler potential function for geomagnetic latitude and radius
β	Euler potential function for geomagnetic longitude
$\delta\alpha$	Reconstruction resolution of α at each time step
$\delta\beta$	Reconstruction resolution of β at each time step
r_{Vox}	Radius of the voxel of interest
$\mathbf{R}$	Regularization matrix
η	Relative weighting between observations and regularization

1 Introduction

Solar Extreme Ultra Violet (EUV) and X-ray radiation, together with particles carried by the solar wind produce the ionosphere – a region in the upper atmosphere where neutral atoms are ionized to produce free electrons and ions (plasma). The charged particles interact with the Earth's magnetic field to create a region of low energy plasma above the ionosphere, known as the plasmasphere.

Electrons produced in the ionosphere and plasmasphere can drastically affect properties of radio signals traversing the medium. The effects on radio systems change with varying concentrations of charged particles within the upper atmosphere, and the eleven-year periodic activity of the Sun has a direct impact on the composition of the ionosphere. Measuring and imaging the total electron content (TEC) – the total number of free electrons in a unit cross sectional area – helps to provide a better understanding of these upper atmospheric regions and improve current models developed through a suite of ground-based measurements. Signals of the Global Positioning System (GPS), a Global Navigation Satellite System (GNSS), have proven to be a valuable source for measuring TEC along their paths of propagation. Indeed, given the ionized region is the dominant cause of GNSS signal degradation, the derived TEC also has a turnaround impact on the accuracy and integrity of GPS; whereby the ionospheric error can be measured and removed. To these ends, the research presented here suggests the installation of dual-frequency GPS receivers in nano-satellites (CubeSats) that will measure TEC and quantify the free electron concentration in the dayside topside ionosphere and plasmasphere.

Two aspects are considered in this research. The first is the development of technology. The topside ionosphere starts from an altitude of ~600 km, with the plasmasphere extending up to ~20,000 km above the ionosphere. Isolating the topside and near-Earth plasmasphere from the lower atmosphere requires GPS receivers placed in Low Earth Orbit (LEO) altitudes of 600-800 km. A relatively cost-effective method of reaching such altitudes is by means of CubeSat technology – nano-satellites defined as miniaturised satellites of low mass (<500 kg) and size. This provides a unique viewing geometry of the

near-Earth space environment and thus improved vertical resolution of the electron concentration in the topside ionosphere and plasmasphere. As the method is yet untested, an initial pilot receiver is launched as a payload in a single CubeSat. This phase of the research considers the development of the payload, and key design challenges encountered. The satellite placed in LEO will serve as a technology demonstrator for a future constellation of CubeSats, which will enable improved global vertical electron profiling of the near-Earth-Space environment.

With the instrument in place to obtain a new set of measurements, a setup needs to be established that can process the data and enable imaging of the region. Thus, the second aspect of the research is tomographic imaging of the topside ionosphere and plasmasphere – an inverse problem that constructs a multi-dimensional image from multiple measurements of an object. Ionospheric (TEC) tomography uses the integral of the number of free electrons between satellite and receiver, measured by radio signals propagating through the medium. For GPS-based tomography, TEC measurements are derived from the differential phase of dual-frequency transmissions of GPS satellites. The final TEC allows four-dimensional (4-D – i.e. 3-D spatial and time evolving) mapping of the ionosphere [*Bust and Mitchell*, 2008]. In the work presented here, this is carried out using the software, 'MIDAS' (Multi-Instrument Data Analysis System) [*Mitchell and Spencer*, 2003]. Originally developed solely for the ionosphere, the algorithm is modified to implement a priori knowledge of the topside and plasmasphere, thus providing improved imaging of the upper ionized regions.

To give an overview of the research presented in this thesis, Chapter 2 gives an introduction to the solar-terrestrial environment that impacts the topside ionosphere and plasmasphere. In particular, it discusses the solar wind and the interplanetary magnetic field, followed by the geomagnetic field and the magnetosphere.

Chapter 3 provides a review of the topside ionosphere and plasmasphere – the upper reaches of the Earth's ionised atmosphere. First it explores the structure of the topside ionosphere, and its coupling to the plasmasphere and the underlying main ionosphere, followed by the structure and morphology of the plasmasphere. The chapter also provides an overview of recent observations of the regions, with emphasis on GPS observations and the data sources responsible for these measurements.

Chapter 4 discusses imaging of the ionosphere with GPS. First, an introduction to the concept of GPS is given, including the effects of the ionised atmosphere on the signals. It then moves on to ionospheric tomography as a method of imaging the electron concentration of the region, followed by a description of the imaging algorithm suite MIDAS.

Chapter 5 is dedicated to the first phase of the research – the development of the low-cost technology demonstrator 'TOPCAT' to exclusively image the topside ionosphere and plasmasphere. First, the chapter discusses the CubeSat platform on which the instrument is installed as a payload. It then moves on to the design and development of TOPCAT, followed by a section on challenges encountered during its design life-cycle. The chapter concludes with a discussion of the qualification tests and their results, which successfully qualified the technology to be used in a space application.

Chapter 6 addresses the second phase of the research, which validates MIDAS for the topside ionosphere and plasmasphere. First, it describes the adaptation of MIDAS for the higher altitudes. Next, the chapter presents the steps taken to validate the inversion algorithm through reconstructions of a simulated plasmasphere, and the true topside ionosphere-plasmasphere (with real GPS measurements from the COSMIC constellation). The results of the validation are then presented, achieved through the qualitative comparison of the images with independent observations.

Finally, the thesis is concluded with Chapter 7, which summarises the results and discusses potential future work that may be undertaken based on this research.

Research Objectives:

The thesis aims to develop the first stages of a system capable of studying the ionised upper regions – from providing a data source to imaging electron concentrations by:

- Developing a GPS-based CubeSat payload to be placed in LEO as a cost-effective technology demonstrator, realised through the design of control electronics to operate a commercially available receiver controlled by the satellite platform.
- Validating MIDAS for topside ionosphere-plasmasphere by reconstructing the electron concentration of first, a simulated plasmaspheric model, followed by the true plasmasphere with measured TEC from the COSMIC constellation.

2 The Solar-Terrestrial Environment

2.1 Introduction

The Earth's upper atmosphere is strongly coupled with solar activity. Radiation and particle emissions from the Sun reach the Earth by means of the solar wind and interact with the Earth's neutral atmosphere and magnetic field to form the ionized atmosphere – the ionosphere and plasmasphere – and the magnetosphere. Understanding these regions and their effects on radio propagation thus requires an appreciation of the entire solar-terrestrial environment.

This chapter gives a brief overview of the interplanetary constituents, the solar wind and interplanetary magnetic field (IMF), which have the largest impact on the ionized upper atmosphere. It then follows on to discuss the Earth's magnetic field and the magnetosphere, including some of the current systems that interact with the ionosphere and plasmasphere. The chapter concludes with a summary that sets the stage for the following chapters.

2.2 The Solar Wind and the IMF

The interplanetary medium is defined as the space between celestial bodies in the solar system. It carries interplanetary dust, cosmic rays, solar wind plasma, and the IMF originating from the solar magnetic field. The solar wind and IMF, in particular, are of importance to this thesis due to its contribution to the ionised atmosphere of the Earth.

2.2.1 The Solar Wind

The Sun is not in a state of equilibrium. The active nature results in the Sun's continuous expulsion of matter and radiation into space, giving rise to a permanent solar wind consisting of a stream of particles, and electromagnetic and thermal radiation from radio emissions. The solar wind transports matter across the solar system.

Although comprising both partially and fully ionised molecules, the solar wind is considered to be quasi-neutral. Since lighter particles can escape the Sun's gravitational

forces more readily, the main constituents of the solar wind at a distance of 1 AU (distance between the Sun and Earth) are fully ionised protons (H^+) and ∝-particles (He^{2+}). A small component of heavier molecules is also present that is only partially ionised. The density of the ions is matched by a similar number of free electrons whose equivalent negative charge equals the positive charge from the ions. This quasi-neutral plasma, at 1 AU from the Sun, has been observed to travel with a speed between 200 and 800 km/s [*Hargreaves*, 1992].

The permanent solar wind may be enhanced by phenomena occurring in the Sun's atmosphere. The activity of the Sun is observed to have an 11-year cycle, over which it rises to a peak and return to a minimum. During periods of high activity there is more chance of solar flares – a sudden brightening of small areas of the photosphere caused by the release of highly compressed plasma during the break-down of magnetic fields. The energy released is of a magnitude of ~10^{25} J [*Hargreaves*, 1992] and may take the form of electromagnetic radiation or particles. The latter is responsible for a majority of sporadic enhancements of the solar wind.

The *effects* of the solar wind on the Earth's atmosphere, as with the solar wind itself, are strongly influenced by solar activity. Some upper atmospheric disturbances can be particularly attributed to certain types of solar emissions. For example, X-rays are observed to cause sudden ionospheric disturbances, while low energy plasma is closely associated with magnetic storms and aurorae [*Hargreaves*, 1979]. Figure 2.1 shows a coronagraph taken by the SOHO satellite (instrument: LASCO C3) which displays the radially expelled plasma [*NASA*, 2013].

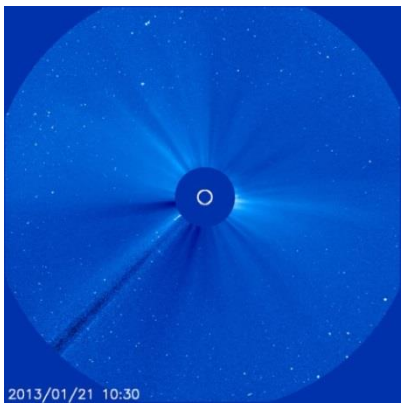

Figure 2.1. A real-time coronagraph from the instrument LASCO C3 of the SOHO satellite. The expulsion of plasma as solar wind was imaged on 21/01/2013 at 1030 hours [Credit: SOHO (ESA & NASA), accessed from [*NASA*, 2013]].

2.2.2 The Interplanetary Magnetic Field

As the solar wind travels outwards from the Sun, it carries with it a 'frozen-in' weak Interplanetary Magnetic Field (IMF), which is an extension of the solar magnetic field. The field is frozen in because the plasma electrical conductivity is large, and its energy density is greater than the magnetic flux density. Consequently, the plasma flow carries the IMF along with it. Although the solar wind travels radially outward from the Sun, the rotation of the Sun results in a spiral ejection pattern for matter and the IMF. The angle of trajectory of the solar wind at Earth orbit is observed to be ~45°.

The IMF is an important contributor to the dynamics of geospace – the region encompassing the upper atmosphere up to the outer extents of the geomagnetic field (i.e. the magnetopause). The interaction of the IMF with the Earth's magnetic field has a twofold effect: aided by the solar wind, the field-interaction maintains the structure of the magnetosphere; and the orientation of the IMF and its regions of anti-parallel reconnection with the geomagnetic field influence ionospheric plasma convection patterns, particularly in the polar regions. For example, a southward IMF reconnects with the geomagnetic field in the dayside to form open field lines in the polar cap region, causing a magnetospheric flow from the magnetopause to magnetotail. This results in a corresponding ionospheric flow across the polar cap from local noon to local midnight. Following eventual reconnection of the open field in the magnetotail, the newly formed closed field line approaches Earth and move back toward the dayside. This induces the ionospheric plasma to flow from local midnight back to local noon, thus completing the convection pattern. Conversely, a northward IMF follows a similar process, but produces a flow opposite in direction, particularly at very high latitudes [*COMET et al.*, 2004a]. It must be noted that, although the IMF has the most impact at high-latitudes, coupling between the ionosphere and plasmasphere ensures plasma dynamics in the topside ionosphere and plasmasphere – the regions of interest in this research – are also affected. Further information on the interaction between the IMF and geomagnetic field is given in Section 2.4.

2.3 The Geomagnetic Field

The magnetic field structure of the Earth, to a first order approximation, is a dipole. The primary source (>99.9%) of magnetism is considered to be electric currents generated by

the motion of the metallic liquid within the core. A small proportion is attributed to ionospheric currents. Disturbances in these currents give rise to transient (periodic) and diurnal variations in the magnetic intensity measured on Earth [*Tascione T.F.*, 1994].

The poles of the magnetic dipole, although generally aligned in the geographic South-North direction, do not coincide with the rotational axis. Consequently, two magnetic poles are defined, giving rise to the geomagnetic coordinate system which is used extensively in plasmaspheric studies due to its strong coupling with the geomagnetic field. The pole positions are derived from the best fit of a hypothetical earth-centred dipole and the measured magnetic field strengths. The relationship between the geographic and geomagnetic coordinates is given as: [*Tascione T.F.*, 1994]

Let geomagnetic latitude $= \lambda$ and geomagnetic longitude $= \phi$

geographic latitude $= \Lambda$ and geographic longitude $= \Phi$

At a point P, $$\sin\lambda = \sin\Lambda \sin\Lambda_0 + \cos\Lambda \cos\Lambda_0 \cos(\Phi - \Phi_0) \quad (2.1)$$

and $$\sin\varphi = \frac{\cos\Lambda \sin(\Phi - \Phi_0)}{\cos\lambda} \quad (2.2)$$

where $\Lambda_0 = 80.0°N$ and $\Phi_0 = 72.2°W$ are the geographic latitude and longitude of the geomagnetic north pole for the year 2010.

It can be derived from the definition of the dipolar magnetic potential [*Tascione T.F.*, 1994] that the magnetic intensity B at a given geomagnetic latitude is,

$$B = H_0 \left(\frac{R_E}{r}\right)^3 \{1 + 3sin^2\lambda\}^{1/2} \text{ (T)} \quad (2.3)$$

where, H_0 is the tangential component of the equatorial magnetic potential (T), R_E is the surface radius (m), and r is the radial distance from the centre of the Earth (m).

From equation (2.3) it can be inferred that the strength of the magnetic field decreases with the cube of the height from the Earth's centre, and the magnitude at the poles is a factor of two higher than at the equator.

In addition to a spatial reference system in geomagnetic coordinates, a corresponding temporal reference is also needed for plasmaspheric studies. This is known as the

Magnetic Local Time (MLT), which is analogous to the Local Time (LT) of a geographic location. MLT is calculated by using the antipode of the sub-solar point (MLT = 0000 hrs) as the reference, with the local noon defined as when the Sun crosses the local geomagnetic meridian. The mathematical definition of MLT in terms of the magnetic longitude is given in equation (2.4) [*Bhavnani and Vancour*, 1991]:

$$MLT = \frac{ML_i - ML_{ant}}{15^\circ} \tag{2.4}$$

where, ML_i is the magnetic longitude of the point of interest and ML_{ant} is magnetic longitude of the antipode of the sub-solar point.

2.3.1 Particle Retention (Trapped Particles)

The closed field lines of the Earth's magnetic dipole extend to >3 Earth radii (R_E), with different extents in the dayside and nightside hemispheres. This region is capable of trapping charged particles which gyrate around the magnetic field lines. Beyond this altitude the field lines are distorted due to interactions with the solar wind and the IMF. The particles contained within the magnetic field define the extent of the plasmasphere.

Two factors contribute to the trapping mechanism. If the Earth's magnetic flux density is considered as static, it can be shown that a moving electric charge gyrates around the magnetic field at an (angular) gyrofrequency ω_B due to the Lorentz force acting normal to the velocity of the particle and the magnetic flux [*Hargreaves*, 1992]. The velocity must contain a component normal to the direction of the magnetic flux. The gyrofrequency of a trapped particle is defined as,

$$\omega_B = {}^{eB}/_{m_p} \quad (rad/s) \tag{2.5}$$

where, e is the electronic charge (C), B is the magnetic flux density (T) and m_p is the mass of the particle (kg). Since particles in geospace typically have both normal and tangential velocity components relative to the magnetic flux, this results in a helical motion of the charged particles around the magnetic field lines.

The second factor is the magnetic mirror phenomenon. The density of the magnetic flux varies between the poles, with the highest density at the poles and the lowest at the magnetic equator. As a particle travels towards a pole, it experiences a force that opposes the tangential velocity. This results in the charged particles bouncing back equatorward from the stronger field at higher latitudes, thereby being trapped within the Earth's

magnetic field. The point at which the particle reverses its path is known as the mirror point. This is illustrated in Figure 2.2 [*Hargreaves*, 1992])

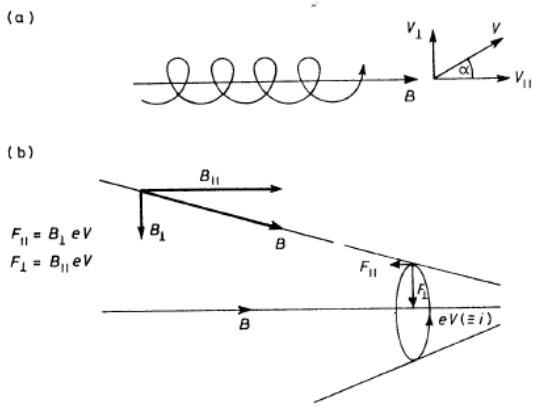

Figure 2.2. Factors contributing to particle retention by closed magnetic field lines [*Hargreaves*, 1992]. (a) The spiral motion caused by the normal (gyration) and tangential velocity (spiral movement). (b) Retarding force experienced closer to poleward higher flux density that opposes the tangential velocity towards the poles.

The particle retention property of the magnetic field is the principle means by which plasma is confined within the plasmasphere. Noteworthy is that the same mechanism is responsible for the Van Allen radiation belts of higher energy particles, which are found in the altitude ranges of 1.25-2 R_E (inner belt) and 3-7 R_E (outer belt) [*Masson et al.*, 2009]. Although overlapping with the low energy (cold) plasma of the plasmasphere, the radiation belts are beyond the scope of this research and will not be discussed further. Additional details may be found in related literature such as [*Darrouzet et al.*, 2009; *Ganushkina et al.*, 2011].

2.3.2 Azimuthal Drift and the L-Parameter

Particles retained by closed field lines experience an azimuthal drift (i.e. a motion of the guiding centre) as they oscillate between the poles. The drift is caused by a combination of two mechanisms: The gradient of the magnetic field (gradient drift) and the centrifugal force experienced by particles due to the curvature of the field (curvature drift). The geomagnetic field is stronger closer to the Earth and weakens with increasing distance from the Earth. This gradient causes a varying gyroradius of the particles, which decreases in a strong magnetic field and vice versa. The resulting drift is perpendicular to both the magnetic field and gradient, and is charge-dependent, thus causing the electrons and ions to travel in opposite directions. Conversely, the curvature drift is caused by the centrifugal force the particles experience due to their parallel

motion along field lines. This is also perpendicular to the magnetic field and the curvature, effectively contributing to the gradient drift. A rigorous explanation of the motion of trapped particles can be found in [*Baumjohann and Treumann*, 1997]. Figure 2.3 [*SPENVIS*, 2013] summarises the paths taken by particles trapped within the geomagnetic field.

A particle's azimuthal drift path effectively outlines a (hypothetical) 'shell' as it traverses around the Earth, which is defined by the magnetic fields around which it is gyrating. In the presence of a perfect dipole, a given particle will have a constant drift-distance from the Earth (e.g. a drift-distance is equal to the geomagnetic equatorial crossing of the field line at the geomagnetic equator) directed only in the longitudinal direction. Within the Earth's magnetic field however, drift patterns deviate from that of a dipole and the 'shell' structure becomes more complex. Thus, to accurately map and better understand particle distribution in the trapped region *McIlwain*, [1961] defined the 'L' parameter that describes 'shells' formed by a set of field lines having the same spatial mirror-point location. This is based on the fact that two particles on the same field line but with different mirror points will drift to different longitudinal lines of field. It must be noted that, under the same definition, shell-splitting may be observed during spatial mapping of particle densities. Shell-splitting is the drift of particles to a different shell (or escape from the trapping region altogether) to maintain drift along the field lines of the same intensity; which may occur when the field lines are compressed by the solar wind in the dayside hemisphere [*Hargreaves*, 1992].

The L-parameter is defined as ([*McIlwain*, 1961]):

$$R = Lcos^2\lambda \tag{2.6}$$

where, R is the radial distance from the centre of the Earth in Earth radii units (R_E) and λ is the geomagnetic latitude. L has the dimension of length in R_E.

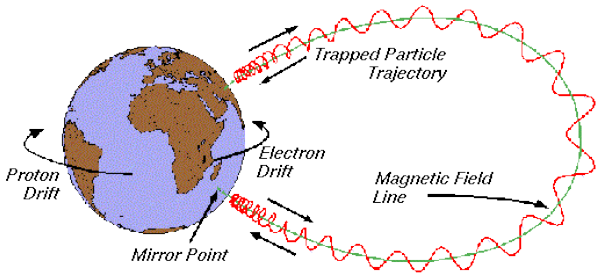

Figure 2.3. Illustration of the motion of particles trapped by closed geomagnetic fields [*SPENVIS*, 2013]. The diagram highlights gyration around field lines, trapped motion along the field lines between conjugate points on the two hemispheres (with the mirror point shown), and longitudinal drift of charged particles – ions, westward and electrons, eastwards.

2.4 The Magnetosphere

The magnetosphere is a 'cavity' surrounding the Earth, where the motion of particles is largely determined by the geomagnetic field rather than plasma properties. It is defined as the region where plasma density is exceeded by the magnetic flux density [*Hargreaves*, 1979], i.e.

$$\frac{B^2}{2\mu_0} > N_p kT \tag{2.7}$$

where, B is the magnetic flux density (T), μ_0 is the magnetic permeability in free space (H/m), N_p is the particle density (m^{-3}), k is the Boltzmann constant (JK^{-1}) and T is the plasma temperature (K).

The magnetosphere encompasses tens of Earth radii and acts as a transitional region between interplanetary space and geospace. This interaction results in complex physics mechanisms, the details of which (especially of the outer magnetosphere) are beyond the scope of this research. However, since by the above definition the topside ionosphere and plasmasphere lie within the inner magnetosphere [*Hargreaves*, 1979], a brief discussion of the region is warranted.

2.4.1 The Structure of the Magnetosphere

In the absence of the solar wind, the geomagnetic field will extend in an isotropic manner into interplanetary space. As the solar wind encounters the geomagnetic field, a shock wave is generated ahead of the magnetosphere and most of the plasma is redirected around the Earth. This is because the geomagnetic field acts as a barrier to the high electrical conductivity of the plasma [*Hargreaves*, 1979]. The physics of plasma

redirection can be explained with the same principles used to describe the IMF within the solar wind (Section 2.2). The boundary at which the barrier occurs is known as the magnetopause. It marks the extent of the magnetosphere, which is determined by the balance of plasma and magnetic pressures of the solar wind and geomagnetic field, respectively. The magnetopause is strongly defined at ~10R_E in the sunward direction (during undisturbed conditions), while a weaker boundary is observed at distances beyond 60R_E in the anti-solar direction. During periods of high solar and geomagnetic activity the dayside magnetopause may be found much closer to Earth, even reaching altitudes comparable to GPS orbits, particularly during strong storms. The dayside termination of the magnetosphere is well-defined because the sunward geomagnetic field becomes compressed by the solar wind pressure, increasing the magnetic flux density of the region. An illustration of the magnetosphere is presented in Figure 2.4 [*Reiff*, 1999].

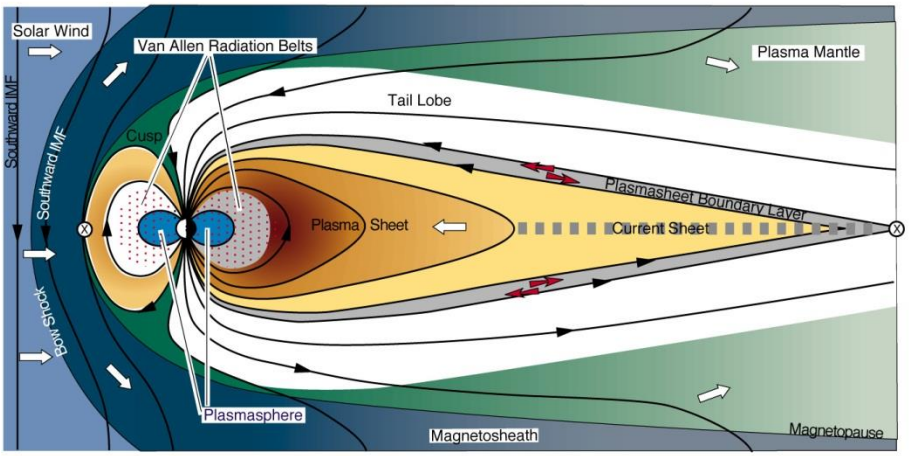

Figure 2.4. An illustration of the Earth's magnetosphere, with the main particle regions highlighted [*Reiff*, 1999]. The solar wind travels from left to right, with a southward IMF embedded within. With these properties, the IMF interacts with the Earth's magnetic field thus forming a region where the solar wind environment mixes with the geospace.

While extensive details of the outer magnetosphere is not relevant to the research, two features are of particular importance as they are significant to the innermost magnetospheric regions, within which lies the plasmasphere [*Hargreaves*, 1979]:

- A magnetically neutral region can be observed between geomagnetic latitudes 70° and 80° in each hemisphere. Models and experiments conducted show the areas as cusps where the magnetic fields of the magnetospheric surface converge. This enables particles from the magnetosheath to enter the lower regions of the

magnetosphere and atmosphere. The polar cusps therefore play a significant role in the direct entry of solar wind matter into the Earth's atmosphere. Effects of particle introduction can be seen in variations/enhancements of the polar ionosphere.

- Below the cusps (i.e. below ~70° geomagnetic latitude) the magnetic field lines are closed between the two hemispheres and capable of trapping particles (Section 2.3). The plasmasphere as well as the Van Allen radiation belts are thus confined to extending between the mid-latitudes of the two hemispheres.

2.4.2 Current Systems

The interaction between moving charged particles and magnetic fields results in a number of current systems within the magnetosphere. These systems facilitate the redistribution of particles in the region as well as contributing to the overall magnetic flux density through current induced magnetic fields. The sources of the different magnetic flux contributing to the total magnetospheric flux density are given in equation (2.8) [*Tascione T.F.*, 1994].

$$B_T = B_d + B_{rc} + B_{tail} + B_{mpause} + B_{FAC} \tag{2.8}$$

where, B_T is the total magnetic flux density in the magnetosphere, B_d is the geomagnetic flux density, B_{rc} is the flux density induced by the ring current, B_{tail} is the flux density induced by the cross-tail (plasma sheet) current, B_{mpause} is the flux density induced by the magnetopause (Chapman-Ferraro) current and B_{FAC} is the flux density induced by the field-aligned currents.

The current systems, while defined discretely in equation (2.8) are not independent, as they interact with each other to form a complex network of global current circuits. However, based on the region of the magnetosphere considered, certain current systems have a more significant effect than others. The topside ionosphere and plasmasphere are mostly influenced by the ring and field-aligned currents as they are found in the inner magnetosphere. As such, these will be discussed further in the following sub-sections. Details on the cross-tail and magnetopause currents, occurring in the outer magnetosphere, may be found in other related literature. A global view of all the current systems is given in Figure 2.5 [*National Academy of Sciences*, 2003; *COMET et al.*, 2004b].

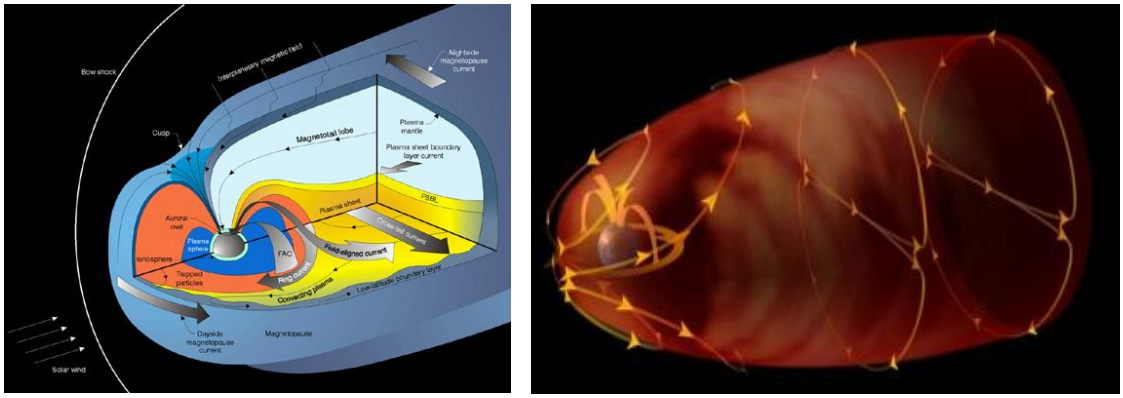

(a) (b)

Figure 2.5. The structure of the magnetosphere. (a) An illustration of the Earth's magnetosphere, including current systems[1] (b) The magnetopause current systems [*COMET et al.*, 2004b][2]

2.4.2.1 Ring Current

The ring current occurs in the inner magnetosphere and is coupled to the plasmapshere. It originates from the longitudinal drift experienced by charged particles trapped within the closed magnetic fields. The current dominates the inner magnetosphere in terms of energy density, and is largely maintained by protons travelling westward. Electrons travelling in the opposite direction maintain the current flow, but have a weaker contribution due to their smaller energy density. The source of particles driving the system is the near-earth magnetotail, having an energy range of hundreds of keV [*Ilie*, 2007]. In addition to the protons and electrons, O^+ ions have also been observed to significantly contribute to the current, particularly during storms. This is attributed to positive ions being accelerated from the ionosphere via field-aligned currents, where the electric field is parallel to the magnetic field [*Tascione T.F.*, 1994].

Due to the drift properties discussed in Section 2.3.2, the current rotates around the Earth and lies between 3 and 7R_E. The magnetic field induced by the ring current acts to oppose the geomagnetic field, thus reducing the overall magnetic field of the Earth. The effect can be measured at the surface of the Earth via the Disturbance storm (Dst) index, which is derived from the horizontal component of the mid- and low-latitude geomagnetic field. During storm times the enhanced ring current can even result in a

[1] Reprinted with permission from *The Sun to the Earth – and Beyond: A Decadal Research Strategy in Solar and Space Physics*, (2003) by the National Academy of Sciences, courtesy of the National Academies Press, Washington, D.C.

[2] The source of this material is the COMET® Website at http://meted.ucar.edu/ of the University Corporation for Atmospheric Research (UCAR), sponsored in part through cooperative agreement(s) with the National Oceanic and Atmospheric Administration (NOAA), U.S. Department of Commerce (DOC). ©1997-2015 University Corporation for Atmospheric Research. All Rights Reserved.

negative Dst index as the surface magnetic field reduces due to the enhancement of the ring current's induced magnetic field.

2.4.2.2 Field-Aligned (Birkeland) Currents

Birkeland currents are vertical current systems that dominate mid to high latitude regions. They flow along electric field lines parallel to the magnetic field, with the charged particles gyrating around the latter. Field-aligned currents have an important role in outer-magnetosphere-ionosphere coupling as the open field lines are connected to the magnetotail field. The currents are mainly carried via electrons accelerated by the electric field. The spatial distribution of the current system is over the auroral ovals, where it is largely arranged as a 'double-layer' structure – poleward and equatorial – defined as regions 1 and 2. Flows along the field lines in the cusp area are called Region 0 currents. Within each region the current contains two components directed into and out of the ionosphere. This enables particle exchange between the atmosphere and the solar wind/magnetosphere, thus coupling the two regions (Figure 2.6 [*Iijima and Potemra*, 1976; *COMET et al.*, 2004b]). The current circuit is closed via the ring current at equatorial latitudes and the Pedersen current at the poles. More information on the polar current can be found in [*Hunsucker and Hargreaves*, 2003].

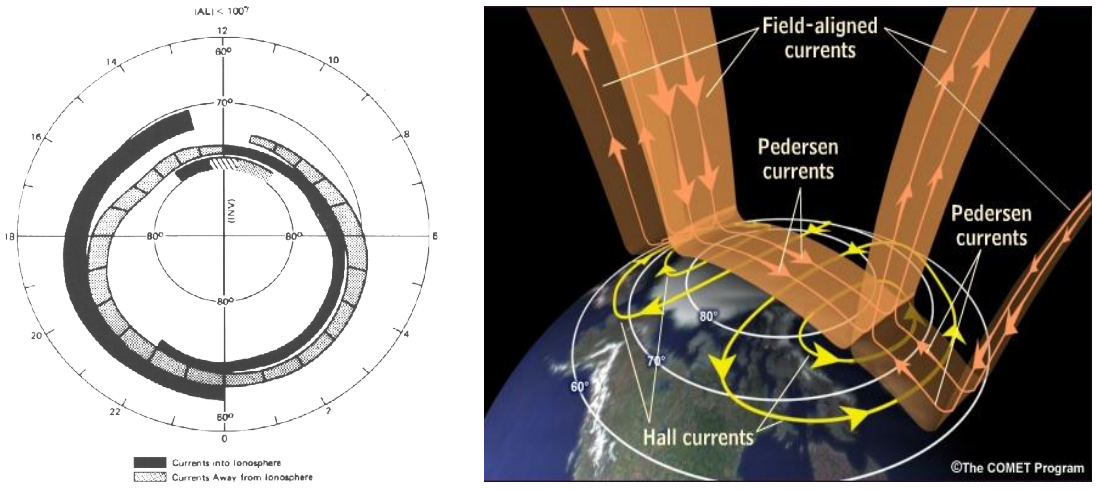

(a) (b)

Figure 2.6. Current systems in the polar regions. (a) Schematic of the field aligned (Birkeland) current in the polar regions [*Iijima and Potemra*, 1976]. (b) Illustration of the high latitude currents – Field-aligned (Birkeland) current, Pedersen current and Hall current [*COMET et al.*, 2004b][2].

2.4.3 Magnetic Reconnection

In addition to the magnetospheric currents, magnetic reconnection also acts as a source of solar wind plasma within the atmosphere. Reconnection is the result of the interaction between two differently oriented magnetic fields. As the two fields meet, they lose their

identity and the fields break down to reconnect and form 'new' field lines with different properties. The nature and behaviour of reconnection at a given instance is determined by the orientation of the interacting field lines.

Magnetic reconnection in the magnetosphere occurs through different mechanisms at the dayside magnetopause and in the anti-solar directed magnetotail. Together with the Earth's rotation, magnetic reconnection is responsible for driving ionospheric convection that influences particle distribution (section 2.2.2). The direction of the IMF encountered by the magnetosphere plays a crucial role in the convection pattern. For example, in the dayside, reconnection occurs when a southward IMF encounters the northward geomagnetic field, where the 'new' field effectively becomes open field lines that are connected to the polar latitudes. The open fields are then swept in the anti-solar direction by the continuous solar wind, within which they are 'frozen-in'. These field lines are responsible for the direct injection of solar wind/magnetosheath matter as discussed earlier, and for coupling the ionosphere with the outer magnetosphere. In contrast, magnetotail reconnection is the result of interactions between oppositely directed geomagnetic field lines from the two hemispheres that occur when the field lines are stretched in the anti-solar direction. If the field lines from the different hemispheres are close enough, they will break-down and reconnect as they are oppositely directed. In this scenario, the 'new' magnetic field is closed and the matter trapped within travels sunward and gyrates along the field lines to enter the atmosphere. An illustration of the dayside and night-side reconnection scenarios are given in Figure 2.7 [*COMET et al.*, 2004a][2].

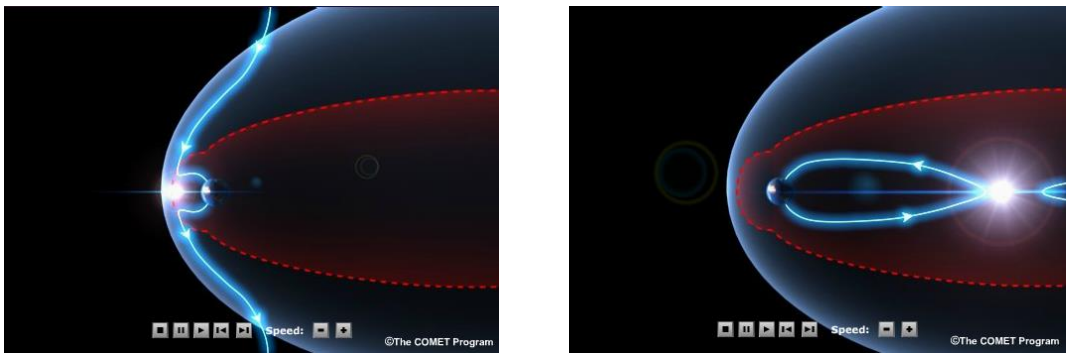

(a) (b)

Figure 2.7. Dayside and nightside magnetic reconnection [*COMET et al.*, 2004a][2]. (a) Reconnection in the dayside when encountering southward IMF, resulting in the coupling between the outer magnetosphere and the Earth's atmosphere through open field lines. (b) Reconnection in the magnetotail when the north and south field components from the two hemispheres meet. The new closed field line move sunward resulting in sunward convection of plasma.

2.5 Summary

This chapter gives an overview of the factors influencing the topside ionosphere and plasmasphere, which lie in the inner magnetosphere. The magnetosphere is a 'cavity' surrounding the Earth, formed by the interaction between the solar wind, IMF and the geomagnetic field. It is governed by the magnetic field and deflects the majority of the solar wind around the Earth. The magnetosphere thus acts as a transitional region coupling the geospace with the solar wind and IMF, while preserving properties inherent to the geomagnetic field.

In contrast to the plasmasphere being maintained primarily through particle retention by the geomagnetic field, morphology of the topside ionosphere and plasmasphere is driven by convection patterns setup by current systems within the magnetosphere. The ring current resulting from the longitudinal drift of trapped particles, and field-aligned currents flowing along magnetic field lines at the poles are of particular importance due to their locations and coupling to each other. Particle distribution is additionally influenced by magnetic reconnection within the magnetosphere, whose properties vary depending on the nature and orientation of the IMF encountered.

It can therefore be reasoned that the topside ionosphere and plasmasphere is the culmination of complex interactions within the solar-terrestrial environment, and requires the consideration of both solar and geospace factors when studying the region.

3 The Ionised Upper Atmosphere

3.1 Introduction

The ionised atmosphere extending from 600 km above the Earth's surface is dominated by the topside ionosphere and plasmasphere, with the latter at higher altitudes acting as an interface between the terrestrial atmosphere and outer geospace. As discussed in Chapter 2, the plasmasphere, by definition, is an integral part of the inner magnetosphere. It is, however, also important to the ionized atmosphere due to the strong coupling with the ionosphere.

The chapter presented here discusses properties and characteristics of the region as they are presently understood. First the topside ionosphere's composition and its coupling with both the main ionosphere and plasmasphere are considered. This is followed by a discussion on the plasmasphere, with emphasis on temporal and density variations within the region. The effect of temperature on the plasmasphere's morphology is not included as it is not directly relevant to the work presented here; although it influences the final electron density distribution. The chapter is concluded with an overview of recent observations of the topside ionosphere-plasmasphere made using TEC measurements from GPS receivers. In particular, those in Low Earth Orbit (LEO) are considered due to their relevance in the research presented in this thesis.

3.2 The Topside Ionosphere

The topside ionosphere, extending upwards from the ionosphere's F-region, is distinguished from the latter by the differences observed in its ion composition. As such, the majority of previous studies of the region have been concerning the morphology of its ion densities. However, as the topside's plasma is considered to be electrically quasi-neutral, the total ion density effectively translates to a complementary distribution of the electrons present. This sub-chapter describes the topside ionosphere primarily in terms of the ions found in the region, with the appreciation that the morphology also extends to its electron composition.

The rates of ionization in the topside ionosphere are negligible relative to the main ionosphere, with very low densities of neutral species found above the F2 peak [*Sibanda*, 2010]. The majority of the topside ionospheric composition is thus considered to be sourced from the lower ionosphere. Given the low neutral molecule density, plasma from the F-region readily diffuses into topside altitudes, with the lighter molecules travelling the furthest [*Sibanda*, 2010]. This gives a general vertical structure of O^+, He^+/H^+ and H^+ as dominating ions (in that sequence) between the F-region and plasmasphere [*Bauer*, 1962b].

The topside ionosphere is identified as the region above the F2 peak consisting of a significant concentration of He^+ ions; although O^+ and H^+ are generally regarded as the major species with He^+ being the minor [*Sibanda*, 2010]. While not distinct, its upper boundary is generally considered to be at an altitude of ~1500 km, or when H^+ and O^+ concentrations are similar. This is also known as the Upper Transition Height (UTH). The topside ionosphere (together with the upper F2 region) is thus considered to be a transition region from heavy ions (O^+) to light ions (He^+/H^+) [*Bauer*, 1962b]. The mixture of ion species implies that the main ionosphere (particularly the F-region) is coupled with the topside, and dynamics of the former region has significant influence on the structure of the topside ionosphere. In particular, processes such as plasma transport, field-aligned plasma flows and chemical processes are important as they provide the means by which the main ionosphere may act as both a source and a sink for topside ionospheric constituents [*Sibanda*, 2010].

The topside ionosphere is approximated to an atmosphere in diffusive equilibrium when considering the major ions (predominantly O^+) in steady-state conditions. This is due to two reasons: The rates of loss and production of ions (i.e. chemical processes) in the region are similar, and at steady state, the transport velocity of particles reaches zero as the plasma approaches a stable distribution due to diffusion [*Bauer*, 1969]. However, this state of balance does not necessarily describe the behaviour of the minor constituents, which can be influenced by all elements of the continuity equation – loss, production and transport. Further, the motion of a given ion species is not independent of the other constituents. The separation of ions and electrons establishes an electric field through which the overall distribution is constrained (ambi-polar diffusion) [*Bauer*, 1962b]. Despite the charge separation however, the plasma throughout the topside ionosphere

and plasmasphere is electrically quasi-neutral, with the ion density matched by the electron density in the medium.

The electron density profile within the upper atmosphere was established by means of theoretical and experimental work carried out by Bauer et al. ([*Bauer*, 1962a, 1962b]). This is expressed as,

$$N_e = N_0 exp\left[-\frac{g_0}{2kT}\int_0^{Z'} m_+ \, dz'\right] \tag{3.1}$$

where, N_e is the electron density (m^{-3}), N_0 is the reference electron density (m^{-3}), g_0 is the acceleration due to gravity at the Earth's surface (m/s^2), k is the Boltzmann constant (JK^{-1}), T is the plasma temperature (K), m_+ is the mean ion mass (kg) and z' is the height as a geopotential altitude (km) that takes into account the variation of g with both elevation and latitude.

From equation (3.1) it can be seen that the electron density at a given height is dependent on the region's positive ion constitution and temperature. Thus, it is important to consider transition regions from O^+ to He^+ and He^+ to H^+, F-region structures and temperature when profiling the electron content in the upper atmosphere. The following discussions within this chapter review density and composition variations within the region. The thermal structure, although correlated with the density profile [*Ganguli et al.*, 2000], is not discussed as it is beyond the scope of this research.

3.2.1 The Light Ion Trough

The presence of a H^+/He^+ Light Ion Trough (LIT) and an electron density trough were observed by [*Taylor and Walsh*, 1972] at topside ionospheric altitudes up to ~1000 km (Figure 3.1 [*Marubashi*, 1970; *Taylor and Walsh*, 1972]), similar to the main trough of O^+ ions found in the F-region. They are usually seen between 55° and 60° latitude, and persist in the night-time hemisphere, while variable but distinct during the day. *Taylor and Walsh*, [1972] found the LIT to correlate well with the boundary of the overlying plasmasphere (the plasmapause), with the depletion of local H^+/He^+ concentrations particularly marked in the equatorward edge. This was in contrast to the *total* ion density in the topside ionosphere, where the relationship between the ion trough and plasmapause was inconsistent, thus emphasising the importance of the LIT and strong coupling between the topside ionosphere and plasmasphere.

Investigations by *Taylor and Walsh*, [1972] showed that the LIT's variations in the structure and position are associated with, as with the main ionospheric trough, to local time, geomagnetic activity and season. Although both the LIT and main troughs are similar in terms of their ion/electron depletion structure, they are not necessarily coincident, and appreciable differences have been observed between the two phenomena. In contrast to the main trough, the LIT is persistent during the day and the equatorward edge of the LIT is measured to be steepest at night-time, even during geomagnetically quiet conditions. Considering dayside features of the trough, seasonal and magnetic activity were observed to have a strong influence on the trough minimum and the boundary gradients. In addition to the rate of decrease of H^+ density being smaller during the day, *Taylor and Walsh*, [1972] found that the LIT is clearly defined during local winter, with a rapid decrease in H^+ densities with latitude. During magnetically active periods, the LIT minimum travels to considerably lower latitudes, with observations showing the minimum as low as 40° [*Taylor and Walsh*, 1972]. The cause of the LIT has been attributed to a combination of escape of light ions into the outer magnetosphere as well as reduced ionization during the night. This is in contrast to the explanation for the main ionospheric trough where depletion of ions is accepted to be almost exclusively via night-time recombination.

With the relatively dominant species being O^+ ions at lower topside ionospheric altitudes, it is important to emphasise the significance of the LIT in plasmaspheric studies. Observations by [*Carpenter et al.*, 1969; *Taylor et al.*, 1969; *Grebowsky et al.*, 1970] have confirmed strong coupling between the LIT and plasmapause, primarily due to similarities in the composition and position of the two phenomena. For example, at altitudes between 600 km and 1000 km, results from satellite measurements have shown that distinct trough structures are seen for light ion concentrations, while the O^+ ions show no discontinuity; and the total ion density does not produce a noticeable trough. Further, the measured night-time position of the trough between latitudes 55° and 60° coincides with the plasmapause located at ~60° latitude [*Taylor and Walsh*, 1972]. This property in particular facilitates the identification of the plasmasphere boundary by means of the LIT, and implies the possibility of studying the plasmasphere and plasmapause through features in the light ion/electron densities in the topside ionosphere. In support of additional correlation between the distribution of light ions

and the plasmasphere/magnetosphere, it has been observed that both the magnetosphere and plasmapause experience similar contractions towards the equator in the presence of high geomagnetic activity [*Taylor and Walsh*, 1972]. Of further advantage is the defined structure of the LIT during all local times, thereby being a global phenomenon. This is beneficial in studies concerning the plasmasphere as the dynamics may be observed continuously in a global scale.

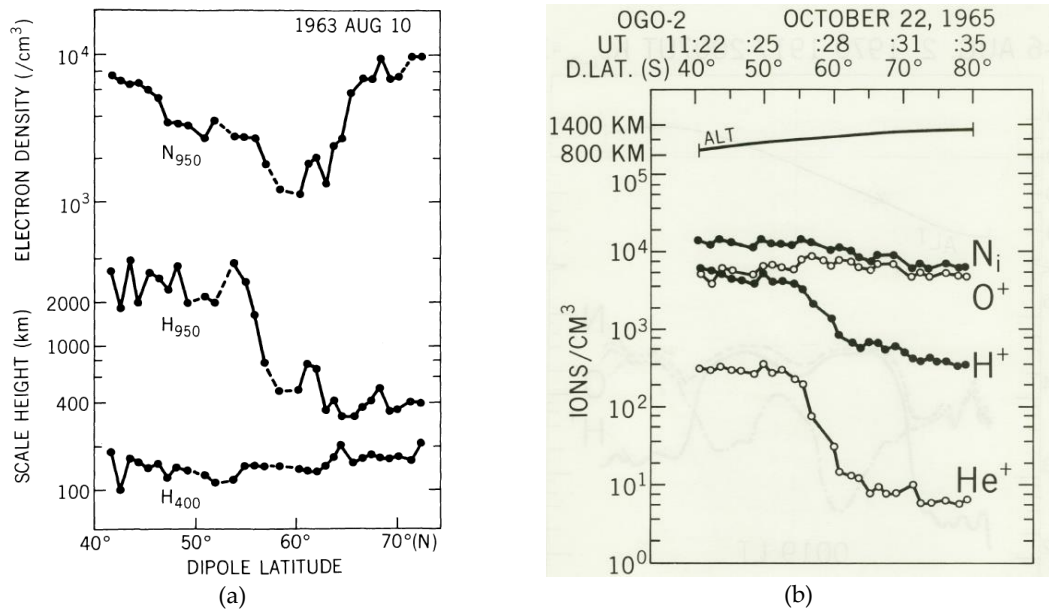

(a) (b)

Figure 3.1. Light ion (H+/He+) and electron density distribution in the topside ionosphere. (a) Electron density variation at 950 km and the scale height at 950 and 400 km, as measured by the Alouette I satellite, indicating the presence of a trough at 950 km [*Marubashi*, 1970]. (b) Ion densities as observed by OGO-2 showing the light ion (He+, H+) trough. The O+ and the total ion density N shows no such variation [*Taylor and Walsh*, 1972].

3.3 The Plasmasphere

As discussed in Section 3.2, electrons and ions experience ambipolar diffusion away from the ionosphere. Their dispersion at high altitudes (>1000 km) however is interrupted by the increasingly dominating geomagnetic field, which prevents the particles from escaping into space (Section 2.3). These trapped ions and electrons, while less dense than the ionosphere, form the plasmasphere [*Gallagher*, 2005a].

The plasmasphere is a toroidal structure situated at a distance of 4-5 R_E [*Lemaire and Gringauz*, 1998] that encompasses the mid and low/equatorial latitudes. As mentioned in Chapter 2, it is found in the region of closed geomagnetic field lines that approximately represents a dipole. The plasmasphere consists of low energy (1-2eV) ions and electrons,

earning its description as an electrically quasi-neutral cold plasma. Its predominant ion constituent is protons (H^+), with smaller proportions of Helium and atomic Oxygen ions present in the medium. The source of the majority of particles is the ionosphere, which flow along the field lines to enter the plasmasphere – hence the toroidal shape. The former also acts as a sink for the plasmasphere, particularly during the night when the ionosphere is depleted due to recombination. Magnetic reconnection contributes a small proportion of solar wind plasma as described in Section 2.4.

The plasmasphere's outer boundary, the plasmapause, is identified with the last closed-field equipotential surface [*Kotova*, 2007]. This is marked by a sharp decrease in the total ion density, although it is less well defined during magnetically quiet periods. The boundary is formed due to the erosion of the outer plasmasphere by sunward convection of plasma that is ultimately driven by dayside magnetic reconnection [*Leblanc et al.*, 2008]. The interaction gives rise to an electron density formation in equatorial regions akin to a 'knee' structure as illustrated in Figure 3.2 [*Brice*, 1967; *Carpenter and Park*, 1973]. The density outside this boundary is very tenuous and is termed the plasmatrough.

The global behaviour of plasma and the definition of the plasmapause are generally governed by its co-rotation with the Earth and with magnetospheric convection. This pattern however is also influenced by other factors, most notable of which are dynamics in the ionosphere and the erosion/refilling of the outer plasmasphere, particularly during sub-storms [*Gringauz*, 1985]. The plasmasphere's interaction with the ring current enhances the complexity of its behaviour. Disturbances in the ring current, reflected by the Dst index, influences the position of the plasmapause in relation to the L-shells. Figure 3.2(a) by [*Carpenter and Park*, 1973] depicts an idealised version of the equatorial electron density profile with variation in the plasmapause position for different Dst values. The plasmapause is indicated by the knee structure in the profiles. The Dst values correspond to different phases of geomagnetic activity, with profile 1 being a quiet time, and profile 2 showing post-storm electron density. A trend is also present in the density, where a gradual decrease is seen radially across L-shells from the inner to outer boundary of the plasmasphere.

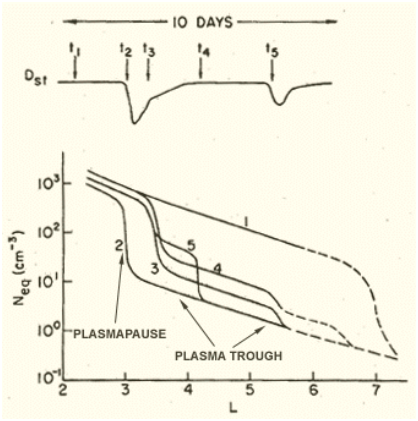

(a)

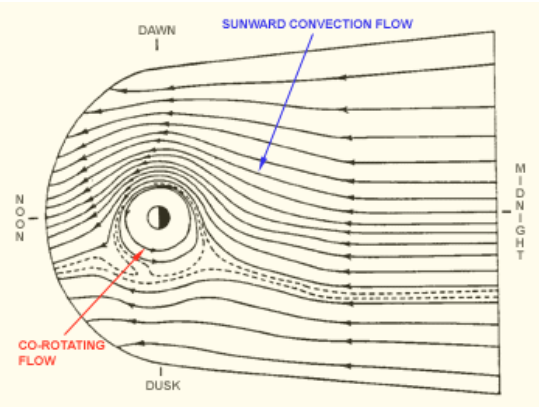

(b)

Figure 3.2. Electron density distribution and plasma flow at the plasmapause/plasmatrough. (a) The variation of electron density with geomagnetic activity, highlighting the location of the plasmapause and plasmatrough in relation to the L-shell. Profile 1 represents quiet time electron density variation with L-shell, and profile 2 is the same during a severe magnetic storm. Other profiles represent intermediate stages, with profile showing a small magnetic storm. The Dst graph above the profiles show the severity of geomagnetic activity [*Carpenter and Park*, 1973]. (b) An illustration of the flow of charged particles at the equatorial plane of the magnetosphere, showing the co-rotation of the plasmapshere and the sunward convection of plasma (modified from [*Brice*, 1967] Southwest Research Institute[3]).

3.3.1 Morphology of the Plasmasphere

Temporal variations in the plasmaspheric density distribution can be seen in both geomagnetically quiet and active times. During quiet periods, co-rotation dominates plasma motion, with upward flow from the ionosphere saturating and extending the plasmasphere up to and beyond L=6 [*Southwest Research Institute*, n.d.] (accessed 2013). Density distributions under these conditions are largely periodic, changing with the local time, geomagnetic latitude and season. The variations closely reflect those of the F-regions. At L≈3, observations show a daily variation of ±10-15% at equatorial latitudes with a minimum density after midnight [*Park et al.*, 1978]. A noon-midnight asymmetry in the shape of the plasmasphere is also seen, with the daytime total ion density with respect to the L-shell (i.e. N(L)) having a gentler profile than at night [*Gringauz and Bezrukikh*, 1976]. The correlation with the ionosphere is seen mainly at dawn, with the patterns diverging towards midnight. This has been attributed to significant recombination in the ionosphere at night, which is not a driving process in the plasmasphere. The night-time density of the plasmasphere sees a significant flow into the F-regions along flux tubes, to replenish ions lost from recombination. The ionosphere thus provides a sink to the proton reservoir in the plasmasphere. Seasonal changes in

[3] Figure 3.2(b) accessed from http://pluto.space.swri.edu/IMAGE/glossary/convection.html

distribution show a peak and trough in December and June, respectively, as well as a dependence on solar activity [*Kotova*, 2007], much like in the ionospheric F-region.

Magnetically active or storm periods see large variations in the plasmasphere. Geomagnetic storms – disturbances in the Earth's magnetosphere due to interactions with a disturbed solar wind – give rise to strong sunward magnetospheric convection, which results in erosion of the outer plasmasphere. The majority of the plasma has been observed to be removed from the dusk side, which creates a bulge and a plasma tail (or plume) that transports charged particles towards the sunward magnetopause (Figure 3.3 [*Southwest Research Institute*, n.d.] accessed 2013). During intense storms, this bulge is seen to shift to earlier hours of the day, and the plume, mainly seen in the equatorial plane, may extend to latitudes up to and beyond 38° [*Carpenter*, 1966]. In addition to the structures, plasma erosion also causes the plasmapause to contract earthward. The relationship between geomagnetic activity and the position of the plasmapause was shown empirically by *Carpenter and Anderson*, [1992] using the 3-hour average geomagnetic planetary (K_P) index (equation 3.2). The K_P index is calculated from K-indices, which gives a measure of fluctuations in the horizontal component of the geomagnetic field over a 3-hour period.

$$L_{PP} = 5.6 - 0.46K_{P_{max}} \tag{3.2}$$

where, L_{PP} is the last L value before a sharp electron density drop is measured and $K_{P_{max}}$ is the maximum K_P in the 24 hours before the measurements. In addition to the removal of outer plasma, depletion is also seen in the inner plasmasphere during the main phase of a storm. Models have attributed the majority of the plasmaspheric content lost (~50-75%) to sinking into the ionosphere, rather than plasmaspheric erosion and subsequent contraction of the plasmapause [*Lemaire and Gringauz*, 1998]; further verifying the strong coupling between the ionosphere and plasmasphere. Following the storm, recovery begins by means of up-flow of field-aligned plasma from the ionosphere. This is a slow process (on the order of days), where refilling is achieved when heated ionospheric matter rises along the geomagnetic field and is trapped in the closed field lines. Various mechanisms have been suggested as sources of thermal energy such as electrostatic shocks and Coulomb collisions [*Southwest Research Institute*, n.d.] (accessed 2015), which require further scientific investigation. Details of such mechanisms, beyond the scope of this research, can be found in [*Singh and Horwitz*, 1992].

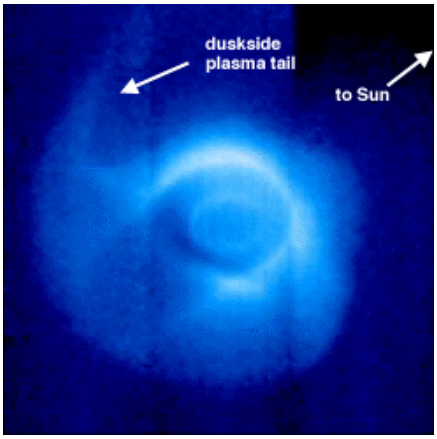

Figure 3.3. An EUV image of the plasmasphere from the IMAGE satellite showing a distinct dusk-side plasma bulge and tail [Credit: B.Sandel and T. Forrester, University of Arizona] [4].

In addition to erosion and the dusk-side bulge, the outer plasmasphere develops numerous density structures during storm activity, particularly in the dusk sector. Formation of the bulge results in the development of plasma patches. These are isolated dense regions of cold plasma that are separated from the main body by areas of tenuous plasma [*Kotova*, 2007]. Investigations by *Kotova et al.*, [2002] into their distribution have shown that these separated plasma structures flow along field lines. Density notches (or cavities) and channels are commonly observed that are characterized by very low plasma densities. Cavities are mainly seen in the dusk-midnight sector following plasma erosion, extending from L=2-3 until a denser region is encountered. [*Sandel et al.*, 2003] described them as regions of broken down flux tubes restricted in latitude to a width of 10°-30°. Channels are narrow regions – suggested to be the result of plumes (plasma tails) twisting around the plasmasphere – that are formed around the pre-midnight sector [*Sandel et al.*, 2003]. A shoulder may develop in the plasmapause boundary, which is an asymmetric bulge, similar, but less intense than the dusk-side bulge. This is believed to be a consequence of the penetration of the solar wind electric field into the inner magnetospheric regions [*Gallagher*, 2005b]. Other structures include 'fingers' and 'crenulations'. These are finger-like thin areas, with 'fingers' having a surrounding plasma of low density and 'crenulations' having ridged low and high density plasma near the outer edge of the plasmasphere [*Gallagher*, 2005b]. The various structures are summarised in Figure 3.4 [*Gallagher*, 2005b].

[4] Figure 3.3 accessed from http://pluto.space.swri.edu/IMAGE/glossary/plasmasphere2.html (accessed 2013)

It can be seen that the majority of density variations are experienced in the outer plasmaspheric regions. As with the general plasmapause position, the formation and variability of these structures have been correlated with K_P rather than the Dst value [*Ganguli et al.*, 2000]. Evidence from density distribution studies has indicated that the plasmasphere's inner regions (L<2.8-3.0) are governed by ionospheric-plasmaspheric processes, and are more stable and resilient against geomagnetic storms [*Kotova*, 2007]. This is in contrast to the outer region, where the behaviour is determined rather by thermal-ring current plasma interactions, thus being more vulnerable to geomagnetic activity [*Kotova*, 2007].

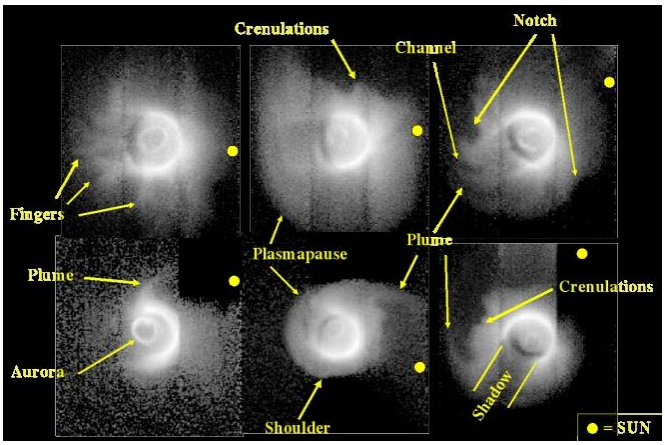

Figure 3.4. Images taken by the NASA IMAGE satellite showing several structures within the plasmasphere [*Gallagher*, 2005b][5].

3.4 Recent Observations of the Topside Ionosphere and Plasmasphere

As mentioned earlier in this chapter, the majority of investigations on the topside ionosphere and plasmasphere have been conducted in terms of their ion densities. While it is appreciated that the plasma exists in a state of quasi-neutrality, it is nevertheless important to independently study the electron distribution to enable a better understanding of the region. This sub-chapter discusses the recent progress made in plasmaspheric imaging using Total Electron Content (TEC) measurements from GPS receivers, with particular emphasis on LEO-based receivers. This is due to its relevance to the research presented in the thesis, which is focused on tomography imaging of the

[5] The image accessed from [*Gallagher*, 2005b] was first used in *Eos Trans. AGU*, 83(47), Fall Meet. Suppl., Abstract SM62B-06, 2002

region using LEO-based GPS data, as discussed in Chapter 6. The concept of the Global Positioning System (GPS), TEC and its use in tomography imaging are discussed in Chapter 4.

Research carried out by [*Foster et al.*, 2002] showed first evidence of the plasmaspheric contribution to TEC derived from ground GPS receivers, through the comparison of vertical TEC (vTEC) results with the co-located Millstone Hill radar. Observations were carried out for the March 31, 2001 storm which showed an ionospheric plume with an enhanced electron density extending into the plasmaspheric tail and toward the noon time magnetopause (Figure 3.5(a) [*Foster et al.*, 2002]). Tomographic imaging for the April 21, 2001 geomagnetic storm also by [*Foster et al.*, 2004] showed substantial evidence of plasmaspheric erosion following the development of a Storm Enhanced Density (SED) plume similar to the March 31 storm. The TEC map result for the erosion from [*Foster et al.*, 2004] is given in Figure 3.5(b).

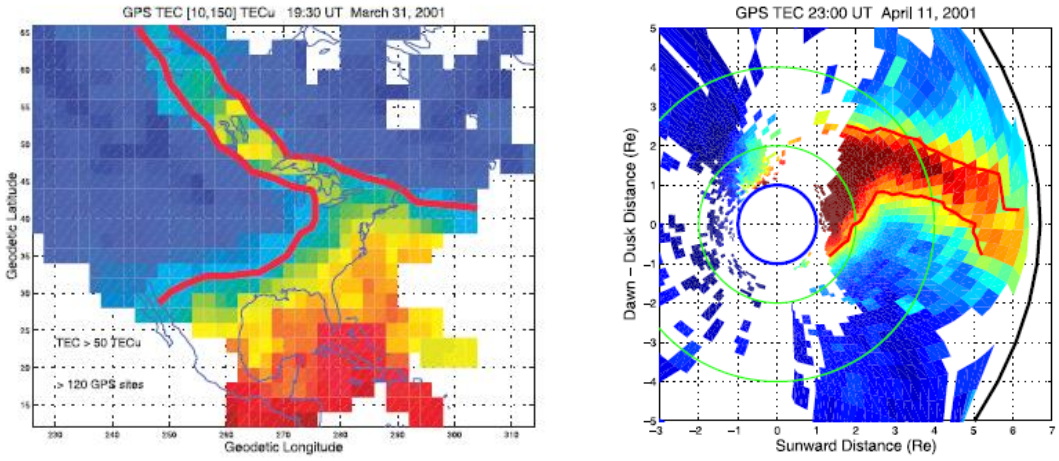

(a) (b)

Figure 3.5. Plasmaspheric signatures derived from ground GPS receivers. (a) TEC map of a storm enhanced density (SED) tail obtained for March 31, 2001 at 1930UT. This was plotted by obtaining the vertical TEC from >120 ground GPS receivers. The red contour marks the instantaneous SED/TEC structure [*Foster et al.*, 2002]. (b) The projection of a plume observed by GPS TEC at 350 km altitude on to the magnetospheric equatorial plane (observed on April 11, 2001 at 2300UT). Plasmaspheric material from the eroded plasmapause extends sunwards [*Foster et al.*, 2004].

In addition to ground-based data, Low Earth Orbit (LEO) receivers intended for GPS Radio Occultation (GPS-RO) and ionospheric sciences, as well as Precise Orbit Determination (POD), enable ray-path geometries to study the topside ionosphere and plasmasphere; which contributes an important data set for the research. Two such LEO satellite systems are CHAMP and COSMIC which have been used extensively for topside ionospheric/plasmaspheric research in recent years. The following sub-sections

give an overview of these satellites and their contribution to the field. An additional satellite – Jason-1, whose primary mission was oceanography – is also discussed due to its significance in the validation of results presented in Chapter 6. The dual-frequency GPS receiver installed within the satellite for POD acts as a data source for plasmaspheric TEC, which has been exploited to image the region.

3.4.1 CHAMP

CHAMP was developed in the interest of advancing GPS occultation TEC (oTEC) imaging techniques, following the success of GPS/MET that provided the first GPS oTEC data. It was launched into a non-sun-synchronous, near polar orbit at an altitude of ~450 km [*ESA*, n.d.]. With a dual-frequency L1/L2 receiver on-board measuring differential carrier phase, its primary focus was profiling the troposphere and ionosphere, whilst studying the Earth's gravity and magnetic fields. During its 10-year lifetime (2000-2010), CHAMP gathered a large data pool of electron density profiles of the ionosphere, while providing vertical temperature profiles for the lower ionosphere.

Imaging the topside ionosphere and plasmasphere with CHAMP data was performed by [*Heise et al.*, 2002] using received GPS signals meant for precise orbit determination. The receiver was capable of simultaneously tracking 8 GPS satellites at a sampling rate of 0.1 Hz. This, together with orbit information of CHAMP (to determine receiver position), was used to derive TEC values for the altitudes between CHAMP and GPS satellites. The TEC measurements were calibrated for various biases via the Parameterized Ionospheric Model (PIM), which includes the Gallagher model for the plasmasphere. A detailed discussion on the use of the models can be found in [*Heise et al.*, 2002]. The biases were the differences between CHAMP TEC measurements and the simulated TEC of PIM. The calibrated TEC for each revolution of the orbit was assimilated into PIM and inverted to provide the electron density. The TEC image produced for a complete revolution on April 23, 2001 is given in Figure 3.6 [*Heise et al.*, 2002]. Results were validated using the in-situ Langmuir probe of CHAMP, which showed a strong correlation between the two data types. A limitation of CHAMP TEC is that, as it is a single satellite, data needed to be collected for the whole orbit (per given orbit); thus necessitating the assumption that the topside ionosphere and plasmasphere are stationary during its period of revolution of ~93 minutes. This meant that while the inversion may be sufficient for quiet periods,

the reconstructed maps were not capable of reproducing dynamic plasma behaviour during geomagnetically active times.

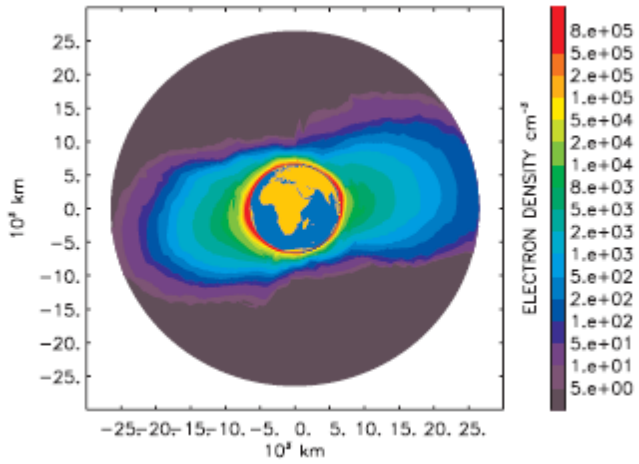

Figure 3.6. 2-D electron density map of the ionosphere and plasmasphere, produced from CHAMP TEC data assimilated for a period of one full orbit [*Heise et al.*, 2002].

3.4.2 COSMIC

The COSMIC constellation comprises six satellites at an altitude of ~800 km. They have an orbit inclination of 72° and are evenly distributed in longitude, providing measurements from 12 different local times on a given day [*Pedatella and Larson*, 2010]. The coverage ensures near-continuous global observation, vital to discerning dynamic structures of the topside ionosphere and plasmasphere. Each satellite consists of two GPS-RO antennas and two POD antennas. In addition to their primary function, the latter can also measure TEC along the LEO-GPS ray paths through differential phase data and 'pseudorange' measurements (derived from the modulating code). The launch of COSMIC thus provided an excellent opportunity to demonstrate the efficacy of satellite-based TEC imaging for detailed plasmaspheric research. To this end, three extensive studies were carried out by [*Pedatella and Larson*, 2010], [*Pedatella et al.*, 2011] and [*Spencer and Mitchell*, 2011], focused on different aspects of imaging the region. The work by [*Pedatella et al.*, 2011] and [*Spencer and Mitchell*, 2011] in particular, are of importance due to their relevance in the research discussed in Chapter 6.

First results were provided by [*Pedatella and Larson*, 2010] with the use of vTEC from the GPS POD antennas. Continuous TEC measurements between LEO and GPS satellites (i.e. ~800 km and ~20,200 km, respectively) taken throughout the year 2008 over the mid-latitude trough provided information on three features of the plasmasphere; the location

of the plasmapause (defined as the equatorward edge of the mid-latitude trough), its variation with geomagnetic activity and local time, and periodic oscillations of the location of the plasmapause. [*Pedatella and Larson*, 2010] observed that the plasmapause location was clearly identified through the latitudinal distribution of vTEC. The plasmapause boundary contracted by 1-2 L-shells with increasing K_P from 0-4, showing the influence of geomagnetic activity. Local time variations were also analysed which showed a deviation from alternative observations. Whereas previous evidence showed noon-midnight and dawn-dusk asymmetries, the COSMIC images of the plasmapause was LT invariant. [*Pedatella and Larson*, 2010] attributed the relative symmetry to the time-averaged nature of COSMIC measurements and the assumption that the plasmapause is collocated with the equatorward edge of the trough at all LTs, although it was observed to separate during daytime; the averaged measurements, in particular, resulting in short-term structures such as the bulge being masked by the overall shape. Annual oscillatory variations in the plasmapause position were associated with geomagnetic disturbances arising from periodic high-speed solar winds caused by solar coronal holes.

Pedatella et al. followed their work on the plasmapause with a COSMIC TEC-based study on the longitudinal variations in the topside ionosphere-plasmasphere ([*Pedatella et al.*, 2011]). They observed that the TEC distribution in the region is both season and LT dependent; with different dynamics in the seasons affecting the ionosphere and topside/plasmasphere differently. The most prevalent feature is the annual anomaly over the American sector observed during solstices, where a maximum is found in the Northern Hemisphere winter and a minimum in the summer (Figure 3.7 [*Pedatella et al.*, 2011]). The feature is seen at all times of the day. A previous study by [*Huang et al.*, 2010] on the ionospheric ion densities also observed a similar distribution in the topside at ~840 km altitude at dusk. They explained the variation as being caused by the large declination of the geomagnetic field over America and the field-aligned component of the neutral wind, which results in a vertical plasma drift.

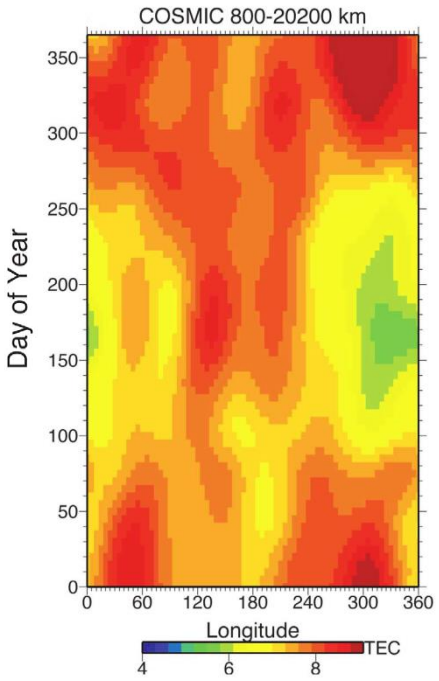

Figure 3.7. Longitudinal variations for the year 2008 observed by COSMIC over equatorial magnetic latitudes (±10°) above 800 km [*Pedatella et al.*, 2011].

Considering the equinox, [*Pedatella et al.*, 2011] saw a wave number 4 structure in March and September that is present only during daytime (Figure 3.8 [*Pedatella et al.*, 2011]). In contrast to the solstices, this was attributed to vertical **E** x **B** drifts and non-migrating tidal waves influences. Previous studies by [*Hartman and Heelis*, 2007; *Huang et al.*, 2010] as well as [*Pedatella et al.*, 2011] also observed a strong wave 4 structure in the **E** x **B** drifts in September at ~840 km altitude, which was collocated with the feature in the equinox's TEC distribution. Plasma temperatures, affected by non-migrating tidal waves, show a similar structure that causes a corresponding change in scale height, resulting in variations in the vertical plasma distribution [*Pedatella et al.*, 2011]. In addition to these mechanisms generating a longitudinal wave 4 structure in the topside ionospheric-plasmaspheric TEC, [*Pedatella et al.*, 2011] also considered the coupling between the F-region and topside ionosphere-plasmasphere. They hypothesized that the diurnal behaviour of the ionosphere – where it acts as a daytime source and a night-time sink to the upper regions – further contributes to the local time dependence of the equinox's longitudinal variations.

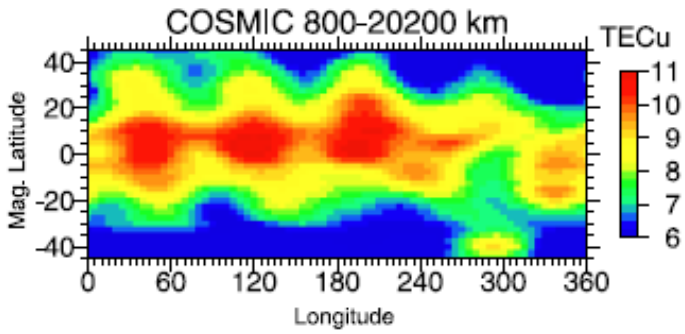

Figure 3.8. COSMIC observation of a wave 4 longitudinal structure seen during September equinox [*Pedatella et al.*, 2011].

Of importance to note is that, while early results on plasmapause studies by Pedatella et al. proved to be highly promising, a limitation exists in GPS TEC derived from pseudorange measurements, where they can be significantly corrupted by multipath. As highlighted by [*Pedatella and Larson*, 2010], this is attributed to signal reflection off the solar panels and the relative susceptibility of the implemented patch antennas (of the receivers) to the undesired signals. Given that the error in pseudorange TEC may be larger than the small TEC values measured in the topside ionosphere-plasmasphere, effects from multipath need to be mitigated in COSMIC data to produce reliable results. [*Pedatella and Larson*, 2010; *Pedatella et al.*, 2011] performed this by calculating the absolute difference between carrier-phase TEC and pseudorange TEC, and weighting the observation points with these values.

Concurrent with the work by Pedatella et al [2011], a complementary study was carried out by [*Spencer and Mitchell*, 2011], where the research focused on global imaging of the plasmaspheric electron density – a first attempt at plasmaspheric tomography. In contrast to the former work, TEC data for plasmaspheric imaging was derived solely from differential phase, which provided the change in TEC along a changing path within the region [*Spencer and Mitchell*, 2011]. Pseudorange information was not used to obtain absolute TEC due to the same vulnerabilities described in Pedatella's research, where the measurement errors are comparable to the region's TEC. The study is of particular importance to this thesis as the results presented in Chapter 6 follow on from this initial work by [*Spencer and Mitchell*, 2011] on plasmaspheric tomography.

Given the study was intended as a demonstration of global plasmaspheric tomography, preliminary results showed only the basic structure of the region; and further work is needed to validate the algorithm for detailed analysis of the plasmasphere. Images

produced showed the toroidal plasmasphere up to ~4R_E with higher densities in the inner plasmasphere for the period December 2008 to January 2009. The plasma is seen to be co-rotating while consisting of a bulge and a somewhat isolated region at lower altitudes depleted of electrons [*Spencer and Mitchell*, 2011]. Although this is as expected, apart from the co-rotation, the presence and properties of the time variant bulge and depleted region was not verified at the time due to insufficient independent data during the period of interest. In addition to the basic profile, an analysis was performed to investigate the relationship between the IMF and overall plasmaspheric properties. Changes in B_Z (i.e. the z-component of the IMF in solar magnetic coordinates) were shown to enhance the post-midnight (and pre-noon, to a lesser extent) plasmasphere at a distance of 3-4 R_E [*Spencer and Mitchell*, 2011]. Particularly, a positive change seems to cause the nightside plasmapause to travel outwards – an observation that may be indirectly corroborated by [*Goldstein et al.*, 2005]. In contrast, changes in B_Y (y-component of the IMF in solar magnetic coordinates) showed asymmetric dynamics where the dayside topside ionosphere is enhanced while the nightside is depleted. Figure 3.9 shows the reconstruction of the global plasmasphere at a specific time as well as the effect of changes in B_Z [*Spencer and Mitchell*, 2011].

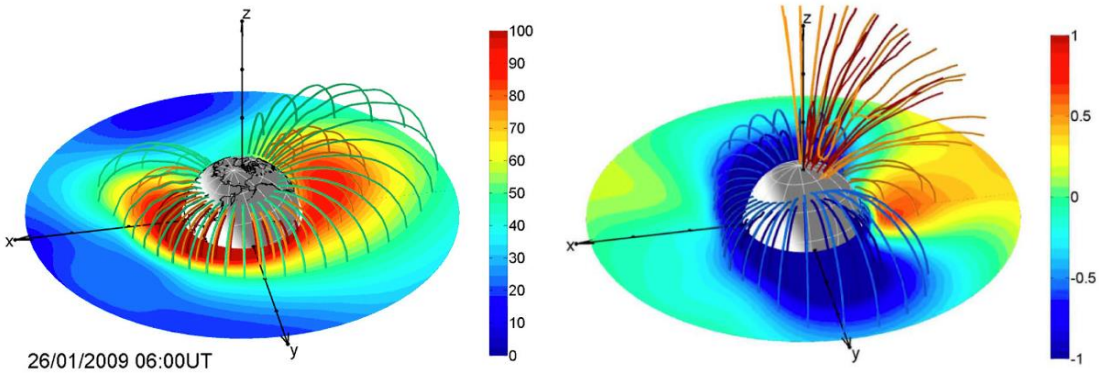

(a) (b)

Figure 3.9. Reconstruction of the global plasmaspheric electron density with and without IMF disturbances [*Spencer and Mitchell*, 2011]. (a) Snapshot of electron density for Jan 26 2009. (b) Effect of a unit change in IMF in Bz, with the diurnal and mean fields removed. The electron density have units 10^8 m^{-3} and Bz is in nT.

3.4.3 Jason-1

Jason-1 was a follow-on mission from the former Topex/Poseidon that studied ocean surface topography. The satellite, which operated from 2002 to 2012, was launched into an altitude of 1336 km with an orbit inclination of 66°, which allowed the majority of oceans to be covered. Jason-1 carried a dual-frequency radar altimeter as its principal

payload to measure sea surface levels and a dual-frequency GPS receiver to support orbit determination. In addition to their primary roles, the dual-frequency capability of the instruments enabled TEC measurements along their signal paths. The altimeter allowed TEC to be measured between the ocean and Jason-1 at 1336 km (effectively, the ionospheric TEC), while the GPS receiver observed plasmaspheric TEC between Jason-1 (1336 km) and GPS satellites (20,200 km). Jason-1 was thus the first satellite to observe both regions simultaneously [*Lee et al.*, 2013], enabling a direct comparison between the ionosphere and plasmasphere and studies of the regions' coupling. The new data set was exploited by [*Lee et al.*, 2013] for this purpose and to characterise global plasmapsheric TEC; the results of which are summarised here. Observations made during low solar activity are used as a source of validation in Chapter 6.

With the operational years of Jason-1 coinciding with the declining phase of solar cycle 23, [*Lee et al.*, 2013] collected data over multiple years to enable TEC observations of the ionosphere and plasmasphere for varying solar activity. GPS measurements from 2002 to 2009 were taken and averaged to analyse diurnal, seasonal and longitudinal variations in the regions. Global behaviour with solar activity was investigated by using 24-hour averaged measurements and F10.7 values across the years. In their analysis [*Lee et al.*, 2013] compared the equatorial plasmasphere with the mid-latitude ionosphere to study the plasma exchange between the regions, particularly at night-time. The difference in latitudes considered within the two regions was because the flux tubes near the magnetic equator at altitudes between Jason-1 and GPS are directly coupled to magnetic latitudes between 20° and 60° at the nominal F-region peak at ~300 km [*Lee et al.*, 2013]. They found that, at night, plasmaspheric TEC decreases by 10%-15% from daytime values (depending on the season), which corresponds to a contribution of 5%-25% F-region TEC. The night-time plasma flow into the ionosphere is largest during the June solstice, while the equinoxes experience the lowest flux. At daytime, although ionospheric TEC nearly doubles with increasing solar activity, the rise in equatorial plasmaspheric TEC is consistently ~30%. [*Lee et al.*, 2013] attributed this difference to a non-linear dependency of the plasmasphere on ionospheric density and the influence of topside ionospheric neutral hydrogen density and neutral plasma temperatures on upward H^+ diffusion within the region [*Richards and Torr*, 1985]. Concerning seasonal and longitudinal variations, [*Lee et al.*, 2013] observed similar features to those seen by [*Pedatella et al.*,

2011] such as the annual anomaly (December TEC > June TEC) over the American sector and an enhancement in June at ~180° longitude. They also noted that the lowest TEC is found around the June solstice under all conditions (i.e. solar/geomagnetic and diurnal). Comparisons between the solstices' TEC over American longitudes showed that the December to June ratio is ~1-3, and is higher at smaller L-shells (typically L<2.5), which supports previous results by [*Park*, 1974; *Clilverd et al.*, 1991; *Richards et al.*, 2000]. High ratios were also observed during night-time and at lower solar activity. Analysis of the global trend with 24-hour averaged data showed an increase in plasmaspheric TEC with solar activity in a nearly logarithmic trend, which is in contrast to a linear increase in the ionosphere. One possible reason, as postulated by [*Lee et al.*, 2013], is that the product-driven upward plasma flow from the ionosphere is restricted once a threshold level is reached in the plasamsphere. In addition, [*Lee et al.*, 2013] emphasized that their analysis defined the ionosphere and plasmasphere in terms of Jason-1's fixed orbit altitude (1336 km). However, the true distinction between the regions is variable, as the ionosphere contracts (expands) with low (high) solar activity, resulting in the lower boundary of the plasmasphere falling or rising accordingly [*Heelis et al.*, 2009]. This means that, in Lee et al.'s study, the plasmasphere below 1336 km during low solar activity contributes to ionospheric plasma, effectively raising the density in the lower regions and reducing the measured TEC between Jason-1 and GPS satellites (and vice-versa); thus explaining another possible cause for the observed rise in global plasmaspheric TEC with increasing solar activity [*Lee et al.*, 2013].

3.5 Summary

The topside ionosphere and plasmasphere are strongly coupled to the main ionosphere below, and the overlying magnetosphere. Density variations in the region are influenced by both ionospheric plasma properties as well as geomagnetic conditions in the magnetosphere. The constant state of transition experienced results in the topside ionosphere-plasmasphere being both similar and distinct from the surrounding areas, with variations in the ion composition regulating much of the density of the region.

The ion composition of the topside ionosphere-plasmasphere varies from heavy ions such as O^+ to the progressively lighter H^+ and He^+ ions with increasing altitude. A light

ion trough of H^+/He^+ ion is found in the topside ionosphere which shows similarities with the mid-latitude ion trough structure in the F-region. The plasmasphere, while generally being governed by the geomagnetic field and activity therein shows strong correlation with ionospheric density variations, mostly during dawn and diverging towards night time when it acts as a source for the F-region.

While the ion composition of the topside ionosphere-plasmasphere is not the focus of this research, a general understanding of the distribution is nevertheless required due to the quasi-neutrality of the plasma. Variations in ion densities are translated to the electron density, which affects radio signal propagation in an ionised medium. Indeed, recent studies have placed much emphasis on the use of dual-frequency GPS signals for topside ionosphere-plasmasphere imaging, as the differential phase gives a measure of the electron density of the region. The results have contributed to a better understanding of the topside ionosphere-plasmasphere, and its coupling to the underlying ionosphere.

4 Ionospheric Imaging with GPS

4.1 Introduction

As discussed in Chapter 3, recent advances in observing the Earth's ionised atmosphere has seen an increased use of GPS TEC to image the region's electron concentration. Imaging the ionosphere using tomography has been a well-established concept since it was first demonstrated with LEO satellites of Russian Cicada and Navy Ionosphere Monitoring System (NIMS). The polar-orbiting satellites, at an altitude of ~1100 km, transmitted signals at nominal frequencies of 150 MHz and 400 MHz [*Bust and Mitchell*, 2008]; which afforded a limited number of passes over a receiver array when measurements could be made. These data sources were later superseded by the Global Positioning System (GPS) constellation following its successful operation in 1995. Orbiting at an altitude of 20,200 km and broadcasting at ~1.2 GHz and ~1.57 GHz, the system ensures the visibility of 8-12 satellites at any given time – thus enabling continuous and global data coverage, and providing much needed measurements for global ionospheric studies.

This chapter briefly presents the concept of GPS and the effects of the ionosphere on its signals that enable them to be exploited to image the electron content of the region. It is followed by an overview on ionospheric tomography. The imaging algorithm suite Multi-Instrument Data Analysis System (MIDAS) is then discussed, which is widely used with both ground- and space-based data sources for ionospheric research. Developed at the University of Bath, it forms the basis for the research presented in the following chapters. The chapter is concluded with a summary of the current state of MIDAS and its potential to image the topside ionosphere and plasmasphere, which can enable comprehensive imaging of the entire ionised atmosphere.

4.2 An Introduction to GPS

The GPS constellation comprises a current total of 31 satellites [*U.S. Naval Observatory*, n.d.] placed in 6 earth-centred near-circular orbital planes, with 4 satellites per orbit

[*Kaplan and Hegarty*, 2006]. The orbits are equally spaced around the equator and separated by 60°, with an inclination relative to the equatorial plane of ~55°. An illustration of the constellation is given in Figure 4.1 [*Kaplan and Hegarty*, 2006]. The orbital period of a given GPS satellite is one-half of a sidereal day (i.e. 11 hours and 58 minutes), while the orbital radius from the centre of mass of the Earth is ~26,600 km. The placement of the satellites ensures 24-hour global coverage and enables users to obtain Position, Navigation and Timing (PVT) solutions virtually worldwide [*Kaplan and Hegarty*, 2006].

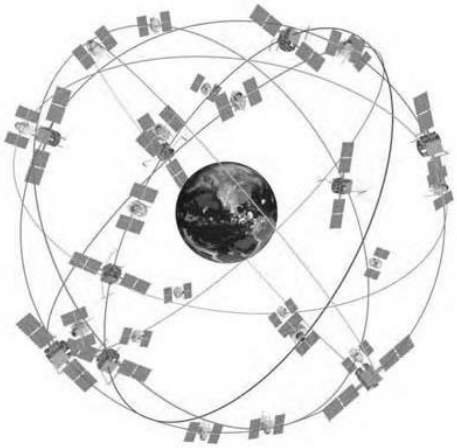

Figure 4.1. The GPS satellite constellation, as produced by Lockheed Martin Corp [*Kaplan and Hegarty*, 2006].

All GPS satellites broadcast information on the two original frequencies, L1 (1575.42 MHz) and L2 (1227.6 MHz). It employs the technique Code Division Multiple Access (CDMA), which allows the satellites to transmit simultaneously on these frequencies, albeit with a code unique to each satellite. Two types of codes are generated through pseudorandom noise (PRN) waveforms – a shorter Coarse/Acquisition (C/A) and a longer P(Y) code. L1 is coded with both C/A and P(Y) PRNs, while L2 is modulated exclusively by P(Y). The L2 signal is encrypted with a Y-code and is primarily used for military applications to gain higher precision. Noteworthy is that recent modernization programmes have introduced additional signals L1C (L1 Civil – 1575.42 MHz), L2C (L2 Civil – 1227.6 MHz) and L5 (1176 MHz) in new satellites that are able to serve civilian applications requiring higher precision and accuracy. Further details on the signals and broadcast information can be found in [*Kaplan and Hegarty*, 2006].

The receivers of GPS signals make up the user segment of the system. These are passive components, capable only of receiving the transmitted signals, and do not communicate

directly with the satellites. Receivers may operate on a single frequency (L1) for general navigation/timing (i.e. PVT) purposes, whilst more expensive multi-frequency receivers may be used for precision applications. The antenna for the receiver may or may not be integrated within the device. The bandwidth of the antenna is generally designed to be between 1% and 2% of the centre frequency to ensure the GPS signal is detected with minimal distortion [*Kaplan and Hegarty*, 2006]. Satellites at low elevations with respect to the receiver are typically disregarded in the PVT solutions as the signals are usually degraded. This is because the horizontal component of the electric field of a received signal is attenuated by the antenna ground plane, resulting in a low gain pattern for low elevation signals [*Kaplan and Hegarty*, 2006]. Once the signals are acquired, the receiver's processer unit tracks the signal and derives PVT solutions required by the user. Details of signal acquisition/tracking and calculation of PVT solutions are beyond the scope of this research, but may be found in additional literature such as [*Kaplan and Hegarty*, 2006] and [*Tsui*, 2000].

4.2.1 Ionospheric Effects on GPS Signals

An electromagnetic wave travelling through the ionized atmosphere interacts with free electrons in the medium as well as the magnetic field; consequently influencing properties of the propagating signal. For radio signals, the impact may be in a number of forms, most significant of which are dispersion, scintillation, Faraday rotation, absorption and/or a Doppler shift observed at the receiver. For GPS signals (the signals of interest in this research), dispersion in the ionized atmosphere is the dominant cause of signal degradation and errors at the receiver. As such, this phenomenon is discussed in more detail in this subsection.

The propagation of electromagnetic waves through a medium is dependent on its refractive index expressed as,

$$n = \frac{c}{v} \tag{4.1}$$

where, n is the refractive index, c is the speed of light and v is the propagation velocity of the electromagnetic wave under consideration. In a dispersive medium the propagation velocity v, and thus the refractive index n, are dependent on the signal frequency. This means, for modulated signals carrying information, the propagation velocity of the signal carrier phase (v_p) is different to the 'group velocity' (v_g) of the

modulating information signal which is at a different frequency. Consequently, signals travelling through a dispersive medium are affected by two different refractive indices – the phase (n_p) and (n_g) refractive index. For GPS signals consisting of a narrow bandwidth compared to the carrier frequency, it can be shown that the phase and group refractive indices in a dispersive medium are related as [*Hofmann-Wellenhof et al.*, 1993],

$$n_g = n_p + f\frac{dn_p}{df} \tag{4.2}$$

where, f is the carrier frequency.

The ionosphere and plasmasphere – the Earth's ionized atmosphere – act as a dispersive medium for GPS signals. Analysis of the region's effects on signal propagation is generally focused on the ionosphere, as its dynamics and structure have been identified to produce the largest errors in GPS systems. However, due to the similarity in the nature of plasma, and strong coupling with the ionosphere, the overlying plasmasphere can also be considered to have similar effects on radio communication.

To understand ionospheric dispersion effects on GPS signals, the relationship between the refractive index for phase propagation and the electron density needs to be considered. Based on work by [*Hofmann-Wellenhof et al.*, 1993], the refractive indices for phase and group can be approximated to [*Kaplan and Hegarty*, 2006]:

$$n_p = 1 - \frac{a}{f^2} \qquad \text{and} \qquad n_g = 1 + \frac{a}{f^2} \tag{4.3}$$

where, a is a constant estimated to be $40.3N_e$ (Hz^2) and N_e is the electron density (m^{-3}). Substituting these expressions in (4.1), the phase and group velocities can be described as:

$$v_p = \frac{c}{1-\frac{40.3N_e}{f^2}} \qquad \text{and} \qquad v_g = \frac{c}{1+\frac{40.3N_e}{f^2}} \tag{4.4}$$

Thus, from the velocities in (4.4), it can be seen that the phase velocity will always be higher than the group velocity; resulting in the carrier phase advancing by the same amount the signal information is delayed. This phenomenon, termed 'ionospheric divergence', results in errors in carrier phase and pseudo-range measurements in GPS receivers, which are required for final (PVT) solutions provided by GPS. Important to note is that the errors are strongly correlated with the electron density of the region, with higher densities resulting in larger errors; which can be exploited to derive the electron

density through differential phase/pseudorange measurements, as demonstrated by previous studies discussed in Chapter 3. A more detailed explanation of ionospheric effects on GPS can be found in [*Kaplan and Hegarty*, 2006].

4.3 Ionospheric (TEC) Tomography

Tomography is an inverse problem, whereby an object is imaged through the reconstruction of multiple measurements of waves propagating through that object. It is a method of remote sensing an article of interest placed between a transmitter and receiver [*Leitinger*, 1996], and has applications in a range of sciences from medical/biological and physical sciences to archaeology. For example, medical computer tomography (CT) scanners use attenuations in X-rays passing through the human body from different angles to obtain a two-dimensional (2-D) cross-sectional image.

The techniques of tomography vary based on the application. Ionospheric tomography was first introduced by [*Austen et al.*, 1988], and is categorised under ray tomography where the electron density in the upper atmosphere (i.e. the object of interest) is derived through total electron content (TEC) measurements along the path of dual-frequency signal systems. TEC is an integral measurement of the total number of free electrons in a column of unit cross-sectional area along the path between two points, such as a transmitter and receiver. It is measured in electrons/m^2, with 1 TEC unit (TECu) equal to 10^{16} electrons/m^2. Ray tomography approximates the measurements as straight-line integrals, enabling ray-bending effects in the image (that occurs due to a varying refractive index) to be discarded. This allows large-scale wave propagation in radio systems to be addressed whilst assuming a stationary medium [*Pereyra*, 2000; *Bust and Mitchell*, 2008]. The concept of tomography, and ionospheric tomography in particular are illustrated in Figure 4.2 [*Dtrx*, 2009; *Sodankyla Geophysical Observatory*, 2014].

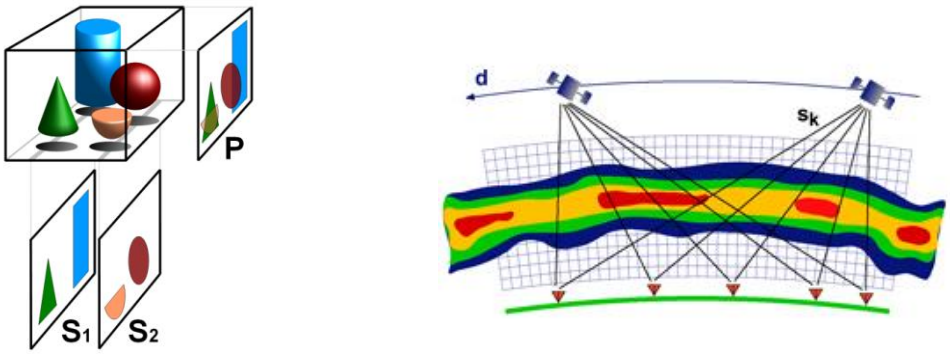

(a) (b)

Figure 4.2. The concept of ionospheric tomography. (a) Illustration of the principle of 2-D tomography, where individual cross-sections S1 and S2 can be combined to form the general projection P [*Dtrx*, 2009]. (b) Principle of ionospheric ray tomography, where the ionosphere is 'pixellated' to enable mathematical computation of the inversion process [Credit: J. Pirttilä][6].

As discussed in Section 4.2.1, the electron density influences the refractive index experienced by a signal propagating through ionised plasma. This in turn affects the phase of the signal travelling between a transmitter (Tx) and receiver (Rx) as follows [*Leitinger*, 1996]:

$$\theta = \frac{2\pi f}{c} \int_{Tx}^{Rx} n \, ds + 2\pi f t + \psi \tag{4.5}$$

where, f is the transmitted frequency, c is the velocity of light in free space, n is the refractive index, ds is the phase path element, t is the time, ψ is the phase constant, and $n \, ds$ is along the path between transmitter Tx and receiver Rx.

The relationship between phase and refractive index can be exploited to derive TEC measurements of the ionosphere by using a dual-frequency system, and comparing the phases of two different signal frequencies that travel the same path between transmitter and receiver (similar to GPS-based studies discussed in Chapter 3.4). The signals must be transmitted with a fixed frequency ratio and with a constant phase relation at the transmitter antenna (i.e. phase coherent) [*Leitinger*, 1996]. Assuming negligible ray-bending (straight line elements between transmitter (Tx) and receiver (Rx)), and using equation (4.5), the differential phase Θ can be expressed as [*Leitinger*, 1996],

$$\Theta = \frac{\theta_1}{p} - \frac{\theta_2}{q} = \frac{2\pi f_r}{c} \int_{Tx}^{Rx} (n_1 - n_2) \, ds + \frac{\psi_1}{p} - \frac{\psi_2}{q} \tag{4.6}$$

where, ds is a given straight line element and f_r is a reference frequency related to the two transmitted frequencies as $f_1 = pf_r$ and $f_2 = qf_r$, with p and q being integers.

[6] Image accessed from [*Sodankyla Geophysical Observatory*, 2014]

Expressing equation (4.3) in terms of the plasma frequency, the refractive index can be written as [*Leitinger*, 1996]:

$$n^2 = 1 - \frac{f_p^2}{f^2} = 1 - \frac{e^2}{4\pi^2 \varepsilon_0 m_e f^2} N_e = 1 - A\frac{N_e}{f^2} \tag{4.7}$$

where, f_p is the plasma frequency (Hz), e is the electron charge (C), m_e is the electron mass (kg), ε_0 is the permittivity of free space (F/m), $A = 80.6$ (m^3/s^2) and N_e is the electron density in m^{-3}. Substituting this expression in equation (4.6), the phase can now be written as:

$$\Theta = \frac{\pi}{c}\frac{A}{f_r}\left(\frac{1}{q^2} - \frac{1}{p^2}\right)\int_{Tx}^{Rx} N_e \, ds + \frac{\psi_1}{p} - \frac{\psi_2}{q} \tag{4.8}$$

where, the integral electron density is the TEC along path $TxRx$, also known as slant TEC (sTEC):

$$sTEC = \int_{Tx}^{Rx} N_e \, ds \tag{4.9}$$

Calculating differential phase measurements enable the plasma medium to be successfully isolated, as any non-dispersive effects from the neutral gas component (affecting both signals indiscriminately) will be eliminated during the comparison. The differential phase shift technique is widely used in ionospheric tomography because it is considered to be directly proportional to the change in TEC to a first order approximation [*Mitchell and Spencer*, 2003]. The method is also known as the differential Doppler technique, as the time derivative of the differential phase can be considered to be approximately proportional to the Doppler shift caused by the plasma [*Leitinger*, 1996].

Historically, systems such as NNSS, Cicada and CERTO derived TEC along LEO satellite-ground-receiver paths using differential phase measurements which were used for 2-D tomographic imaging of the ionosphere. With the launch of the GPS at Medium Earth Orbit (MEO), providing continuous availability and comprising a dual-frequency transmitter system, it is now widely used for ionospheric imaging. In contrast to LEO transmitters, the high altitude placement of GPS satellites allows both ground and space-borne (LEO) dual-frequency receivers to measure carrier phase advances/time (code) delays of the signal (Section 4.2.1), which can be used to extract the electron content of

the region. The flexibility of the location of receivers enables vertically isolated regions to be imaged and eliminate effects from undesired altitudes.

4.4 Ionospheric Tomography with MIDAS

Ionospheric imaging with GPS, while advantageous in terms of coverage and vertical range, suffer from drawbacks inherent to its geometry and orbital period. The higher altitude of GPS in comparison to LEO systems such as NNSS means the satellites move relatively slowly. With significant variability in the ionosphere over this measurement period, the assumption used with LEO satellite-based tomography of a stationary medium between transmitter and receiver is no longer applicable. A new approach was thus required to exploit the new data set enabled by the GPS satellite system. To address the problem, the University of Bath developed the Multi-Instrument Data Analysis System (MIDAS) – a suite of inversion algorithms capable of global and regional imaging of the electron density of the ionosphere.

MIDAS, programmed in MATLAB, reconstructs the upper atmospheric electron density from measured differential phase observations. It is capable of simultaneously solving for spatial and temporal dimensions, thus generating four dimensional inversions. As the name suggests MIDAS can incorporate measurements from different sources, either independently or as a combination of multiple instruments. Conventional tomography of the ionosphere can be performed from single sources such as the extensive network of satellite-to-ground data managed by the International GNSS Service (IGS) or with satellite-to-satellite GPS Radio Occultation (GPS-RO) data. These images however have limitations as the electron profile in one direction – vertical for ground receivers and horizontal for GPS-RO LEO receivers – is lost due to restricted dimensions. [*Hajj et al.*, 1994] proposed to overcome this by combining the two complementary data sets, effectively assimilating both horizontal and vertical profile information to obtain better resolution in all three spatial dimensions. [*Mitchell and Spencer*, 2002] implemented the technique in MIDAS, and successfully produced first results using IGS and GPS/MET RO data over the US mainland. More recent studies have seen the use of CHAMP and COSMIC as GPS-RO sources to map ionospheric electron concentrations in polar regions and during storm-time disturbances over USA and Europe ([*Yin and Mitchell*, 2005, 2014;

Yin et al., 2009]). Other sources that can be used with MIDAS include ionosondes (e.g.[*Chartier et al.*, 2012]), sea-reflecting radar such as TOPEX/POSEIDON and Jason-1, and LEO GPS topside measurements that enables images of the topside ionosphere and plasmasphere [*Mitchell et al.*, 2002]. Indeed, the use of topside measurements from low Earth orbiting GPS receivers is the topic of research presented here. Chapter 5 investigates the possibility of installing dual-frequency receivers dedicated to measure TEC above the ionosphere on-board CubeSats, which can potentially provide a new data set that allows isolated imaging of the region. Chapter 6 discusses the extension and validation of MIDAS to image the topside ionosphere and plasmasphere, enabling successful processing of the data collected from such receivers. Details on the different data sources of MIDAS and their individual strengths are summarised in [*Mitchell et al.*, 2002].

The first step in MIDAS is the pre-processing stage where phase observations from all instruments are collected together with GPS orbit ephemeris and conditioned to a format that can be processed by the algorithms. The sTEC, required for the inversion, is derived from differential phase observations as defined by equation (4.9), albeit modified to include calibration of the measured TEC:

$$sTEC = \int_{Tx}^{Rx} N_e \, ds + c_{cal} \tag{4.10}$$

where, c_{cal} is an unknown constant accounted for by TEC calibration [*Bust and Mitchell*, 2008]. Calibration can be done using the differential time delay obtained from the GPS signals. It considers inter-frequency biases (IFB) which are satellite and receiver-specific (but independent of the ionosphere), and multipath related random and systematic errors [*Mitchell and Spencer*, 2003].

MIDAS defines the imaging problem within a 3-D grid of voxels (volumetric pixels) of latitude, longitude and altitude over a specified time window. The typical spatial grid resolution for ionospheric imaging is 1°-4° in latitude and longitude and 100-200 km in the radial dimension. A time resolution of 15-20 minutes is usually used to observe the evolution of the ionosphere. The electron density within each voxel of the grid is determined based on the geometry of ray paths passing through the voxel and the total integrated TEC (derived from differential phase) of each path measured at the receiver.

The concept is illustrated in Figure 4.3 [*Mitchell et al.*, 2002]. For simplicity, only a 2-D pixel grid is considered.

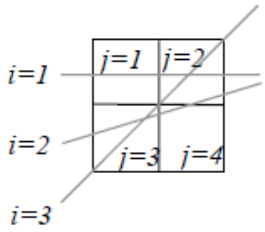

Figure 4.3. Grid-based tomography implemented in MIDAS. A 2x2 grid structure with projections indexed as i and pixels as j. Assuming each pixel has a value of 1, then $i_1 = 2$; i_2 (entering at an angle of 22.5°) = 2.4; $i_3 = \sqrt{2} + \sqrt{2} = 2.8$ [*Mitchell et al.*, 2002].

In order to compute the electron density MATLAB discretizes each pixel within the grid. The inverse problem described in equation (4.10) is thus represented through a series of simultaneous equations generalized as,

$$\boldsymbol{b}_{(i)} = \mathbf{A}_{(ixj)}\boldsymbol{x}_{(j)} + \boldsymbol{c}_{(j)} \tag{4.11}$$

$$\Longrightarrow \quad \boldsymbol{b}_i = \sum_j \mathbf{A}_{ij}\,\boldsymbol{x}_j \tag{4.12}$$

(For e.g.) $$\boldsymbol{b}_1 = \mathbf{A}_{11}\boldsymbol{x}_1 + \mathbf{A}_{12}\boldsymbol{x}_2 \tag{4.13}$$

where $\boldsymbol{b}$ is a vector of i vertical TEC (vTEC) calculated from the observed sTEC, j is the number of voxels, $\mathbf{A}$ is a (i x j) matrix of ray path geometry, $\boldsymbol{x}$ is a column vector of j components holding the unknown electron concentration in each voxel, and $\boldsymbol{c}$ is the unknown cycle offset in each voxel. Since the observations are derived from differential phase of L1/L2 signals along the same ray path geometry, the latter component ($\boldsymbol{c}$) can be removed by differencing adjacent rows of $\boldsymbol{b}$ and $\boldsymbol{Ax}$. Equation (4.11) is now reduced to:

$$\boldsymbol{b} = \mathbf{A}\boldsymbol{x} \tag{4.14}$$

While matrix equation (4.14) represents a set of simultaneous equations, the limited ray paths over the entire grid results in an under-constrained problem that does not contain a unique solution for each voxel without a priori knowledge. MIDAS addresses this by using a mapping matrix $\mathbf{X}$ containing a set of Empirical Orthonormal basis Functions (EOFs) in the radial dimension and spherical harmonics-generated basis functions for horizontal variations. As the approach is not based on models derived from long-term statistical data, only a minimum of a priori assumptions are required on the electron density distribution of the upper atmosphere [*Mitchell et al.*, 2002]. The use of EOFs is expressed in matrix form as:

$$\boldsymbol{b} = \mathbf{AX}\boldsymbol{w} \tag{4.15}$$

where, $\mathbf{AX}$ is the basis set of line integral electron concentrations and $\boldsymbol{w}$ is the unknown relative contribution of the basis functions, realized by,

$$\boldsymbol{w} = (\mathbf{AX})^{-1}\boldsymbol{b} \tag{4.16}$$

where, the solution to $\boldsymbol{w}$ is obtained using singular value decomposition or minimal residual method – the latter an iterative numerical approach. The unknown electron concentration ($\boldsymbol{x}$) for each voxel is recovered by,

$$\boldsymbol{x} = \mathbf{X}\boldsymbol{w} \tag{4.17}$$

Since the orbital period of GPS satellites is ~12 hours, a fixed ground receiver will track satellites at high elevation for several hours between rise and set times. TEC measurements taken throughout this time thus contain information on the temporal evolution of the ionosphere. In order to account for these time variations, [*Mitchell and Spencer*, 2003] further extended the algorithm to produce time-dependent inversions. A priori knowledge of the change in electron concentration during a given time period is included with the assumption that changes are linear within a voxel. The change in TEC observed at consecutive time intervals within a given voxel is related to the changes in the ray path geometry and electron concentration such that,

$$\boldsymbol{\Delta TEC} = \mathbf{D}\boldsymbol{y} \tag{4.18}$$

where, $\boldsymbol{\Delta TEC}$ is the observed change in TEC within the voxel, $\mathbf{D}$ is the difference in ray path geometry at consecutive time intervals and $\boldsymbol{y}$ is the unknown change in electron concentration with time. The evolution of the electron concentration per voxel ($\boldsymbol{y}$) is recovered by adopting the same process used for the spatial reconstruction described by equations (4.14)-(4.17). For the ionosphere, linear variations while having sufficient data are ensured by collecting TEC measurements for a typical period of 1 hour with sampling at 30s intervals. The adaptation of the MIDAS for the topside ionosphere and plasmasphere is discussed in Chapter 6.

Figure 4.4 shows a 3-D map of the ionospheric electron density over high latitudes on October 30, 2003 at 2100 UT [Mitchel et al]. This was reconstructed using TEC measured by ground receivers and a priori knowledge of the vertical profile. The evolution of the

structures can be studied by producing a time series of the region, thus giving 4-D images. Details on ionospheric imaging and relevant ionospheric science can be found in [*Bust and Mitchell*, 2008] and associated literature.

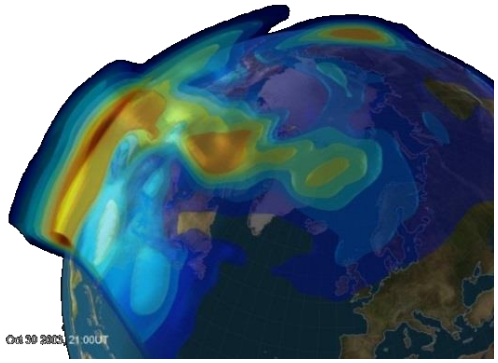

Figure 4.4. 3-D mapping of the ionosphere for October 30, 2003, 2100 UT using MIDAS [Mitchell et al.].

4.5 Summary

Tomography is a widely used technique for ionospheric imaging since it was first introduced by [*Austen et al.*, 1988]. First observational results with dual-frequency LEO satellite-to-ground systems (NNSS, Russian Cicada) used differential phase measurements to derive slant TEC along signal paths; which were inverted through tomography techniques to produce 2-D images. The launch of GPS in 1995 heralded the possibility of 4-dimensional (3-D space and time) images, as the carrier advance/group delay experienced by the signals provided a measurement of electron density in its propagation medium. Transmitting at 20,200 km, the system allowed the implementation of both ground and space-based (LEO) receivers, thus providing higher resolutions in both horizontal and vertical dimensions [*Hajj et al.*, 1994]. The use of LEO GPS receivers also provided a new data set, with vertical ray paths between satellite topside and GPS transmitters giving TEC measurements of the topside ionosphere and plasmasphere. Challenges however needed to be addressed in terms of orbit geometry before GPS data could be used in inversions. The assumption of a stationary ionosphere over the measurement period used with 2-D tomography cannot be used with GPS due to the long orbital period of the satellites. With a constellation of 31 satellites, GPS also presented a more complicated orbital geometry. The MIDAS suite of inversion algorithms developed by the University of Bath address these issues by simultaneously

solving in spatial and temporal dimensions using a 3-D grid structure over a defined time window. MIDAS accepts phase measurements of the signals (at the receiver) as its input, which is then processed to obtain sTEC along the ray paths between transmitter and receiver. The electron density for each volumetric pixel (voxel) is computed through inversion techniques using the ray path geometry within the voxel and sTEC measured with each ray path. MIDAS also has the added advantage of being able to assimilate measurements from multiple instruments (ground and LEO GPS receivers, ionosondes etc), allowing high resolution images. Of particular importance is its ability to incorporate topside data from LEO GPS receivers to image the topside ionosphere and plasmasphere – the topic of the research presented in the following chapters.

5 TOPCAT – In-Situ Imaging of the Topside Ionosphere and Plasmasphere

5.1 Introduction

Given the impact of the Earth's ionised atmosphere on today's technology, much effort has been extended to quantify the electron concentration of the region. As evidenced in Chapter 3, advancements in ionospheric imaging with GPS have resulted in the establishment of extensive networks of ground-based and LEO radio-occultation (RO) receivers that continuously measure ionospheric TEC from received signals. The placement of these receivers however poses a limitation in that the electron densities derived from GPS TEC cannot be differentiated into the different regions of the ionised atmosphere. This is because the integral measurement along signal paths from GPS transmitters (at 20,200 km) to receivers results in the ionospheric electron density masking dynamics of the less dense topside ionosphere and plasmasphere. While this is acceptable for ionospheric studies, the ground-based and RO data lack information on the coupling between space weather and the magnetosphere-ionosphere system. Electron density measurements in regions above the ionosphere thus require in-situ instruments at altitudes above ~500 km, which will allow the topside ionosphere and plasmasphere to be isolated. This implies a need for LEO GPS receivers capable of topside measurements.

Many satellite missions incorporate dual-frequency GPS receivers for precise orbit determination to aid in spacecraft attitude control. This data can be used to derive vertical Line-Of-Sight (LOS) TEC between satellite and GPS transmitters for the topside ionosphere and plasmasphere, provided the receiver is placed in a suitable orbit. Previous GPS Radio Occultation (GPS-RO) missions such as CHAMP, SAC-C, Metop-A, and currently operational FORMOSAT-3/COSMIC (referred to as COSMIC hereafter) occupy(ied) sun-synchronous near-polar circular orbits at altitudes of 600-800 km. These have been ideal candidates for upper atmospheric research and have provided valuable datasets from which TEC has been derived [*Anthes*, 2011; *Yue et al.*, 2011]. Indeed, examples of two such missions – CHAMP and COSMIC – were discussed in Chapter 3.

However, most missions (with the exception of COSMIC) have been single satellites, resulting in very poor spatial and temporal coverage for systematic studies. COSMIC, itself, comprised of a six-satellite constellation is still not optimal for continuous global coverage to study the topside ionosphere and beyond, although the ideal number of LEO satellites has not yet been determined.

This chapter discusses the development of TOPCAT – a low-cost technology demonstrator for in-situ measurement of the topside ionospheric and plasmaspheric electron density. It was installed as a payload in the UK Space Agency (UKSA) led UKube-1 Cubesat – a nano-satellite measuring ~100x100x300 mm. The use of CubeSats for topside ionosphere and plasmasphere science is a novel concept as miniature satellites are an emerging technology that promises significantly low development and launch costs and short turn-around time scales. In addition, the satellite in its entirety (platform and payloads inclusive) was developed with commercial-off-the-shelf (COTS) components, to deliver a relatively cost-effective means of conducting upper atmospheric science. The success of the mission will determine the viability of the instrument for a future constellation of CubeSats that will provide continuous global coverage for imaging the topside ionospheric and plasmaspheric electron density.

The results in this chapter were presented at the ION GNSS+ 2014 meeting, and is published in [*Pinto Jayawardena et al.*, 2014].

5.2 UKube-1

CubeSats are nano-satellites with minimum dimensions of ~100x100x100 mm (known as 1U CubeSats). Larger CubeSats can be realised by scaling the satellite in 1U increments, thus giving 2U (~100x100x200 mm), 3U (~100x100x300 mm) and so forth. The compact design results in a lighter weight and the capability to 'piggy-back' on scheduled launches. This reduces the cost per satellite launched and provides a platform to conduct economically viable feasibility studies that may otherwise require significant funding.

UKube-1 is a 3U CubeSat measuring (100x100x340 mm). It was launched on 8 July 2014 by the UKSA in a Soyuz 2-1B/Fregat-M rocket as the pilot satellite of a national CubeSat programme. The satellite has a mass of ~4 kg and travels in a sun-synchronous orbit at

an altitude of ~630 km. It is 2-axis stabilised with the aid of mangetorquers and rate gyros, and has a spin rate of ≤0.2 deg/s. Communication with the ground station for command and data transfer is via ultra-high and very high frequencies (UHF and VHF) at ~435 MHz (uplink) and 145.840 MHz (downlink) respectively. An S-Band link operating at 2401.5 MHz is also present to enable large data transfers between the satellite and ground station. UKube-1 carries two scientific, one industrial and one educational outreach instruments. In addition to the GPS receiver from the University of Bath (TOPCAT), these are: a CMOS imager (C3D) from the Open University, a true random number (TRN) generator 'Janus' by Airbus Defence & Space, and a self-contained sub-system of a material science experiment and independent communication (FUNCube) for secondary education by AMSAT-UK.

In order to appreciate the capabilities of UKube-1 as a technology demonstrator platform, an overview must be given on the other instruments within the satellite. C3D tests a new sensor technology developed in collaboration with e2v Technologies. It will also act as a test-bench for radiation damage effects in space. The TRN generator by Airbus Defence & Space aims to test new technology that uses single event upsets (SEUs) caused by high energy radiation to produce true random numbers. If feasible, this will be invaluable for secure satellite communication. Janus will also test general effects of SEUs on the electronics used by the payload. FUNCube is an independent payload capable of communicating with ground stations via its transponders. The ground receivers are provided to schools as USB dongles that display payload telemetry in real-time [*AMSAT-UK*, 2014].

A key novelty of using UKube-1 to launch TOPCAT is its orbit characteristics that allow for dayside topside ionosphere-plasmasphere imaging. At an altitude of 630 km, the satellite provides a unique viewing geometry of the near-Earth space environment. Measuring TEC between GPS satellites and the CubeSat topside gives a new dataset that can directly improve the vertical resolution of current ionospheric and plasmaspheric imaging.

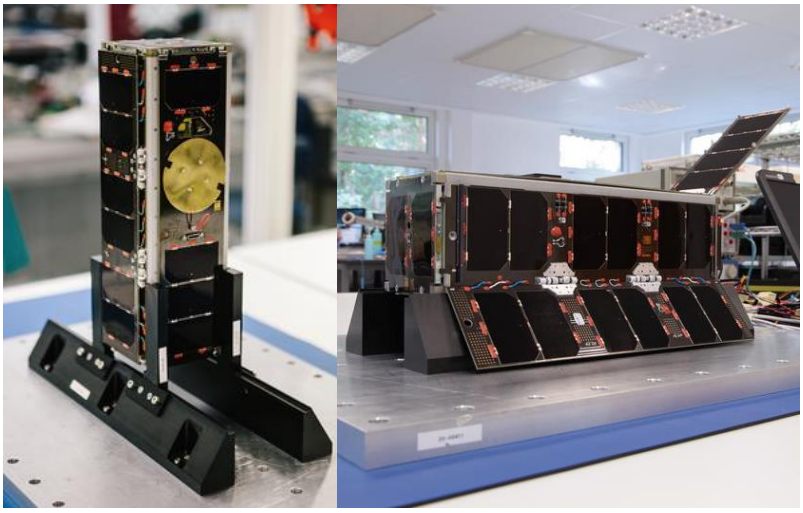

Figure 5.1. UKube-1 ready to be shipped to the launch site. [Credit: Clyde Space Ltd.]

5.3 Payload Design

The dual-frequency receiver used in TOPCAT is the commercially available Novatel OEMV-1DF module, customized for space applications. It has an increased Doppler bandwidth, enabling satellite tracking at high velocities of ~7 km/s. The elevation cut-off functionality is disabled, as a reference to elevation is not available when tracking satellites from space-based receivers. The receiver is connected to an active L1/L2 dual-frequency Antcom patch antenna manufactured for aerospace applications.

To conform to UKube-1 design specifications, the receiver is operated by a payload controller board, which is in turn controlled by the main On-Board Computer (OBC) of the platform that regulates all systems within the satellite. Since the Novatel receiver is a commercially available device, the majority of design efforts were directed towards the realisation of the payload controller board. The electronic design included the hardware, firmware, communication and data processing and storage. Mechanical aspects addressed were the accommodation of the antenna, installation of the radiation shield and the fitting of the fully integrated payload within the satellite chassis. A detailed discussion of the electronic design process is given in the following sub-sections. Challenges faced with the mechanical design are discussed in Section 5.4. The functional architecture and the final design of the payload controller board are shown in Figure 5.2. A detailed schematic of the payload controller board and its PCB layout can be found in Appendix A1.1.

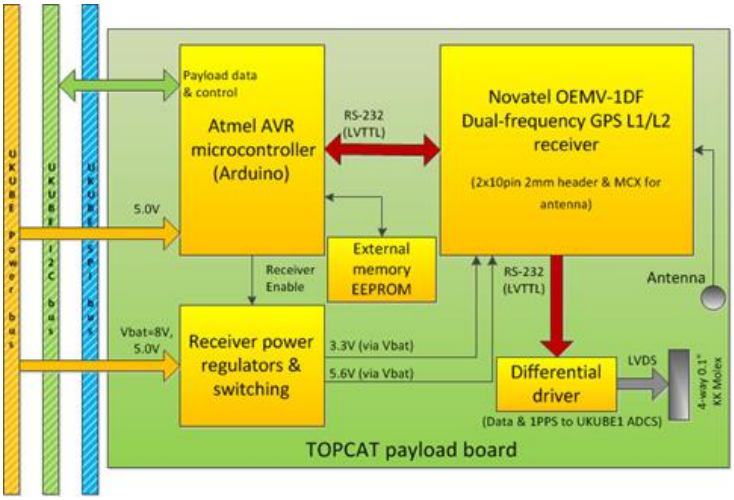

(a)

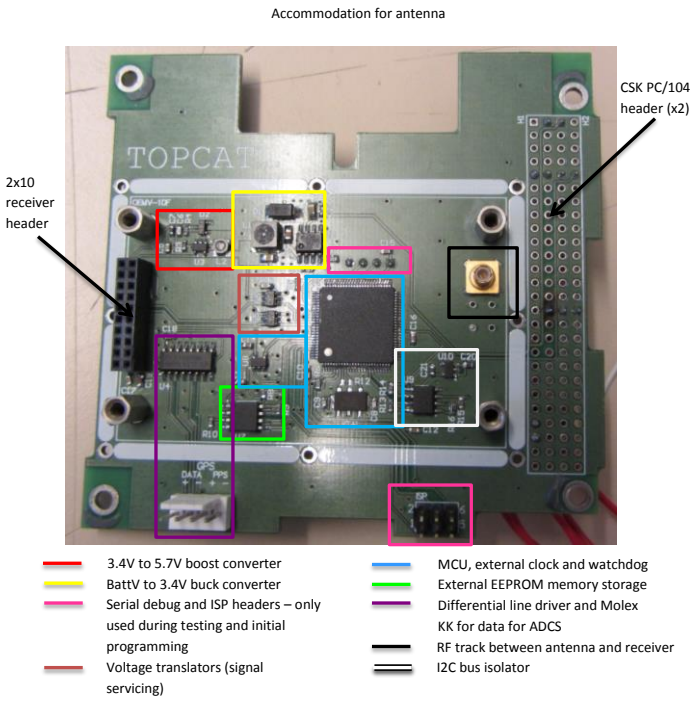

(b)

Figure 5.2. TOPCAT architecture and design. (a) Functional architecture of the TOPCAT payload. (b) The final design of the TOPCAT controller board, with the different sub-systems highlighted. The commercially bought receiver is not included here to enable the devices of the controller board to be viewed.

5.3.1 Power and Control Hardware

5.3.1.1 Power

Power resources utilised by TOPCAT are 5V for the payload controller microprocessor and an unregulated battery rail (BatV) for the receiver, patch antenna and peripheral electronics that do not operate via the 5V supply. The receiver requires an input voltage of 3.3V while the antenna needs between 5.6V and 12V for operation. The battery rail is thus regulated within the payload controller board to supply the receiver with 3.3V and 5.7V for the receiver and antenna, respectively. The enable functions of both regulators

are connected to the microcontroller to ensure all electronics within the payload are controlled solely by the local microcontroller, and (ultimately) the platform, as per the specifications.

5.3.1.2 The Microcontroller

TOPCAT uses an Atmel ATMega2560-16AU (ATMega2560, hereafter) microcontroller to regulate functionality of the payload controller board and receiver. The device was chosen as it met virtually all the requirements of the payload, whilst offering a simple architecture on which to programme the desired functions. All preliminary design tests were carried out using the Arduino Mega 2560 development kit, thus enabling a relatively short design cycle. The microcontroller required several interfaces to connect with other payload sub-systems. These were four communication buses (2 serial, I2C and SPI), a reset and watchdog timer (WDT) unit, and enable switches to control power to the components. All interfaces were successfully facilitated through dedicated hardware within the microcontroller. In addition to hardware resources, firmware capabilities were also considered when selecting the microcontroller. In particular, the operation clock rate and Flash/EEPROM/RAM memory determine the level of functional complexity allowed as well as the data rate and handling methods. ATMega2560's 16MHz clock and flash memory provided more than adequate resources for uploading and storage of the firmware. However, the data storage memory modules (i.e. EEPROM and RAM) did not have sufficient capacity to hold the data generated by the receiver. This was addressed by integrating an external EEPROM unit and limiting the use of RAM during operation.

Another unit vital to ensure robust operation of the microcontroller is the reset-WDT module. In general, all microcontrollers consist of a reset interface that can be manually activated in the event a hard-reset of the device is required. However, as TOPCAT's application inherently requires all components be remotely operated, the reset functionality needed to be automated. This was achieved by implementing a watchdog timer – a device that requires periodic activation via a digital pulse by the microcontroller, without which, the device proceeds with resetting the uC.

5.3.2 The Communication System & Signal Servicing

The complete payload (controller board, receiver and antenna) is operated by the OBC software framework which communicates via two buses. All commands and responses between the payload and platform are relayed through the I2C bus. Data may be transferred to the OBC through the same, although a higher speed SPI bus is also available as an optional feature. Since TOPCAT consists of an external memory module and does not require a high data transfer speed, the I2C bus was selected as the sole mode of communication between payload and platform. The SPI bus of the payload is instead utilised internally as the interface between the microcontroller and external EEPROM module. It also served as the programming interface during firmware uploads to the flash memory of the microcontroller, which needed to be implemented before launch. Since this only occurs when all other devices on the payload controller board are powered down, dual use of the SPI, in this context, simplified the design.

Information (both commands to and data from the receiver) is conveyed between the receiver and microcontroller through a serial communication link, which is then transferred to the external EEPROM for storage via the SPI bus. Another serial transmit/receive link was used temporarily for debug operations as it enabled easy access to the firmware during software development. In addition, the GPS receiver module is configured to augment the Attitude Determination and Control System (ADCS) and timing of the satellite. This required a differential line driver, independent of the serial communication system, to transfer the relevant data directly from the receiver to the ADCS. The use of differential signalling here was important to minimise data corruption from interference and cross talk, which can arise due to the significant distance between receiver and ADCS and the different media (PCB tracks/cabling) the signals are required to travel through. It must be noted that given the multiple devices and buses contributing to TOPCAT's communication system, the signals were not compatible at all interfaces. For example, the GPS receiver and the I2C bus communicate at 3.3V signal levels while the microcontroller operates at 5V. The issue was addressed by implementing bi-directional voltage translators that conditions the signals to ensure they are compatible at the receiving end.

5.3.3 Operational Procedure and Firmware

Since the payload needed to be integrated with the platform, an operational procedure was laid down to ensure the process was carried out smoothly. The procedure consists of requested interactions between systems and the handling of commands, parameters, errors and data. The sequence of operation was designed to complement the capabilities and limitations of the platform, as ultimately the OBC is responsible for regulating all functions within the satellite. The procedure is realised through its implementation within the firmware of the payload microcontroller. The TOPCAT operational procedure is illustrated in **Error! Not a valid bookmark self-reference.**. It was based on the platform operational sequence provided by UKube-1's satellite provider, Clyde Space Ltd.

In an attempt to deliver a robust payload that allows maximum possible scientific output under varying operational conditions, measures were taken to include flexibility in TOPCAT's functionality. Multiple operational modes were implemented with different features together with error and parameter handling that enable status monitoring of the payload and the ability to respond to them when required. These features offered a modicum of control over the instrument in an otherwise fully automated system, which can be utilised in the event of any undesired behaviour of the payload. Further, as the development of the platform and payload were carried out separately, it was vital to have a test bench where payload-platform integration could be tested. To this end, the satellite provider issued a platform emulator that reflected virtually all features available in their system; which was used to confirm successful functionality of TOPCAT. The final operational modes and a brief description of each are given in Table 5.1. Parameter and error handling are summarised in Appendix A1.2.

Table 5.1. Operational modes of TOPCAT. Default mode is Mode 0x01. Mode 0x03 will be used only in the event of an operational failure with Mode 0x01 or 0x02.

Operational Mode	Max. Memory	Content	Sampling Frequency	Data Rate
Mode 0x01: Low Data Rate (Minimum)	30kB	Rawephem; Rxstatusevent; Rangecmp; Bestpos	0.05Hz (every 20 seconds)	90samples/30min
Mode 0x02: High Data Rate	200kB	Rawephem; Rxstatusevent; Rangecmp;	0.1 Hz (every 10 seconds)	180samples/30min

(Optimal)		Bestpos		
Operational Mode	**Max. Memory**	**Content**	**Sampling Frequency**	**Data Rate**
Mode 0x03: Receiver Debug/Status Check	30kB	Rxstatusevent; Rxstatus; Satvis; TrackStat	0.0167 Hz (every 60 seconds for the operational period of the orbit)	Variable

Once the payload is powered on, initialised and switched into one of the operational modes by the platform, the microcontroller transmits the desired commands to the Novatel receiver via the serial communication link. Since the commands cannot be sent interactively, they are pre-defined in the microcontroller firmware during flash memory programming. The receiver responds by generating data that is directly transmitted to the microcontroller (also through the serial link). The data is then processed into a pre-defined packet format as per packet protocol specifications issued by the satellite provider. In general, the data are re-arranged to packets of 256 bytes, to which a 2-byte packet header and end-CRC are appended. The processed packets are transferred via the SPI bus to the EEPROM for storage, until they are required to be transferred. Details of the packet content and data sampling information can be found in Appendix A1.3.

Although the external EEPROM module is sufficient to store data for a given orbit, it still contains a finite capacity which will be filled eventually. The data storage is thus used in a cyclical manner, which allows the re-use of the device. In the event the memory is full, no further data is collected until a sufficient number of packets are transferred to the platform, thus clearing some memory for new data. Due to timing limitations, a known number of packets are buffered into the microcontroller, which are then prepared for transfer by appending the header and CRC to the data. Processed packets are transferred to platform memory under the control of the OBC. No packet handling is implemented to the positioning and timing data provided to ADCS and OBC respectively, as they are transmitted directly from the receiver to their destination and do not need to be downlinked to the ground station.

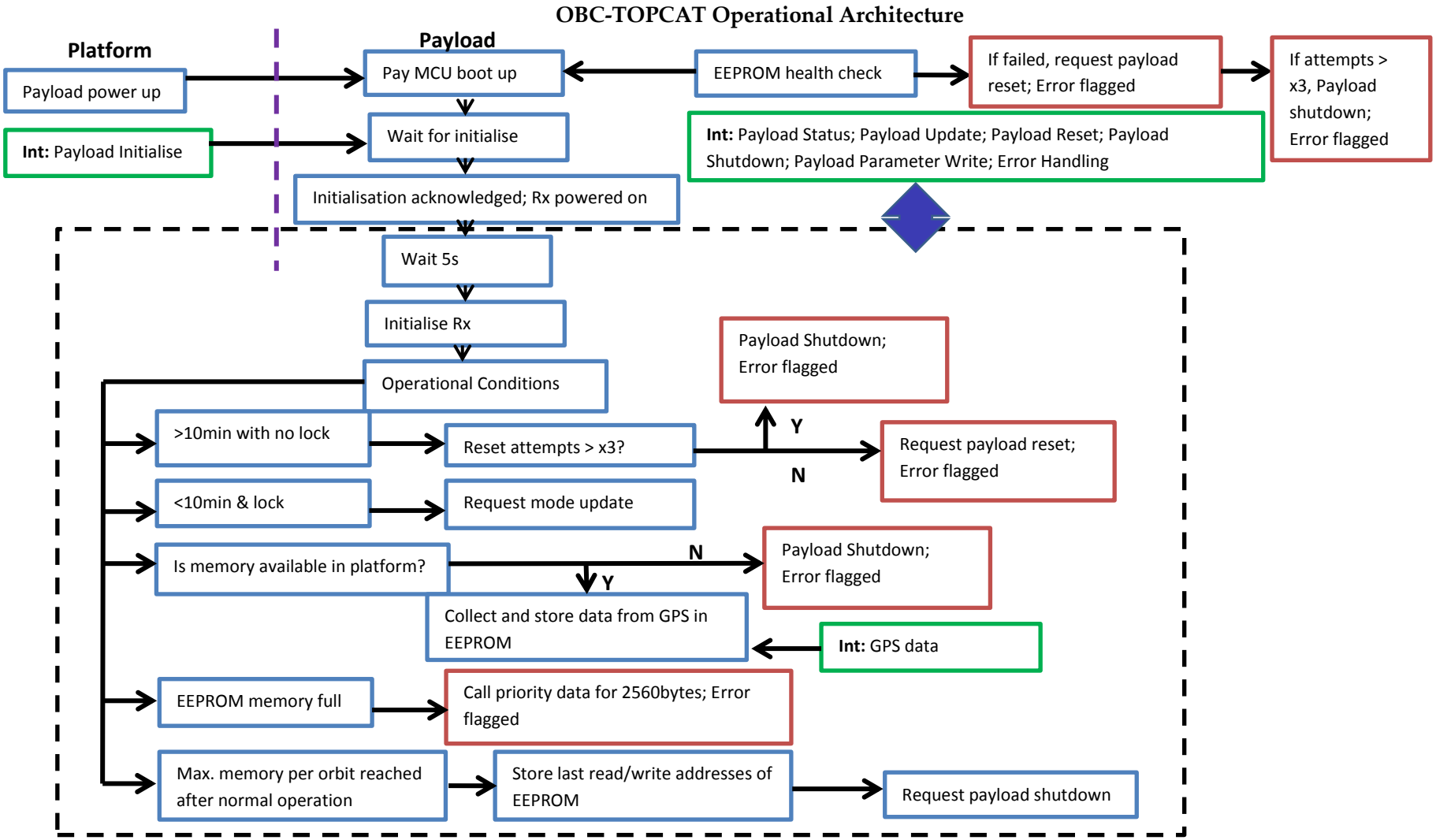

Figure 5.3. Detailed operational architecture of TOPCAT and its interaction with the OBC.

5.3.4 Mechanical Design

A number of limitations needed to be considered during the mechanical design of TOPCAT. The restricted dimensions and weight of UKube-1 limited the flexibility in the design, resulting in a highly compacted payload structure. As the vibration modes of TOPCAT are influenced by the weight distribution and mechanical mounting of the design, care also needed to be taken to ensure the payload resonant frequency conforms to the vibration specifications of UKube-1. Of particular importance was the placement of the patch antenna, which proved to be a significant challenge. This is because patch antennas are inherently susceptible to multipath and require a sufficiently large ground plane to receive a strong signal. Given the limited space available within the CubeSat, this resulted in a number of revisions to the mechanical design. The challenges encountered concerning antenna accommodation are discussed in Section 5.4, while the payload's response to structural integrity tests are presented in Section 5.5. Table 5.2 gives the dimensions and clearances of TOPCAT, which highlights limitations in size.

Table 5.2. Dimensions and clearances around TOPCAT displaying the small profile.

Parameter	Comments	Minimum	Typical	Maximum	Units
Length	Y face	89.85	-	93.94	mm
Width	X face	85.56	-	90.0	mm
Total height	Including tail of connectors	3.6	17.6	-	mm
Clearance over board	From top of board to max. height	-	-	16	mm
Clearance under board	From bottom of PCB to max. height	-	-	2.7	mm

5.4 Design Challenges

Certain challenges had to be overcome to ensure the design conformed to UKube-1 specifications. The satellite's small size imposed limitations on power, mass and space availability for the payload, and the design needed to be realised in a short turn-around timescale (<18 months). Power consumption and data generation in particular were harder challenges as both exceeded the specified capacity. These were mitigated by operating the receiver every sixth orbit and averaging resource usage over all orbits. This

approach was acceptable as the relatively high resources required per orbit are compensated for by reducing the total number of active orbits.

In addition to these 'global' challenges, several technical difficulties had to be addressed before a successfully operational payload was realised. As this was a pilot project to determine technology feasibility, these challenges helped in identifying key areas that require detailed investigations should the concept be expanded in the future. While firmware development also encountered some issues, these were of low-risk, concerning the end-product, due to its 'software' nature. Conversely, hardware setbacks were complex and of higher risk in terms of delivery of the payload. The following sub-sections discuss a selection of design challenges that had the most impact during the development life-cycle. A complete list, together with the mitigation techniques employed, is given in Appendix A1.4.

5.4.1 Antenna Performance and Installation in UKube-1

The foremost issues concerning the development of TOPCAT were GPS antenna performance degradation due to an insufficient ground plane and the mechanical placement of the antenna within the satellite. The initial design proposed the integration of all TOPCAT sub-systems into a single payload. In this version, the antenna was to be mounted on the controller PCB through a bespoke cut-out using an aluminium housing that also acted as its ground plane. The housing (or ground plane) was restricted to an (isolated) 42x42 mm area due to spatial limitations of the satellite. The antenna was to be in-line with the height of the mount wall and placed behind a window of the UKube-1 chassis, so that it may receive the GPS signal through the chassis opening. Integration of TOPCAT in this configuration with the platform however determined that the ground plane area was insufficient for good signal reception and the receiver was unable to track and lock onto GPS satellites. A redesign was thus required of the antenna housing that ensured a larger ground plane. The final version saw the antenna in contact with the ground plane of the solar panels both mechanically and electrically, effectively extending the ground plane area of the antenna and increasing the received signal strength. It must be noted however that the placement of the antenna resulted in a different follow-on problem, where the viewing angle was restricted due to the solar panels. This was mitigated by slightly extending the antenna outside the UKube-1 chassis to obtain the

best possible view. Figure 5.4 shows the evolution of the design to produce the final version.

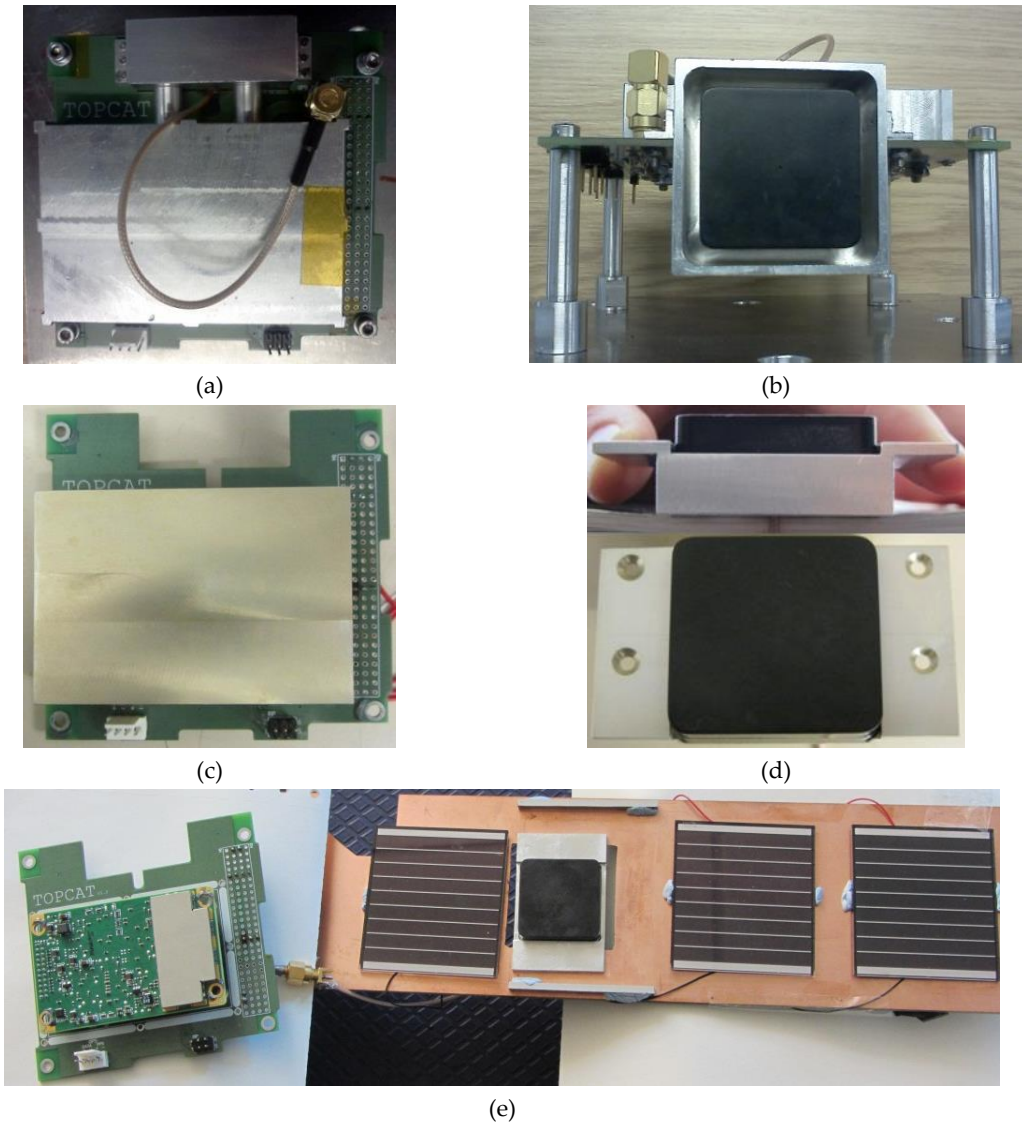

Figure 5.4. Evolution of the mechanical design of the aluminium shield, antenna and antenna housing. (a) The shield and antenna housing were attached through two pillars. The complete payload was considered as a single unit, where the vibration responses were directly related. (b) The previous design for the antenna housing that acts as a ground plane as well as to support the antenna in its placement. This design was not suitable as an adequate ground plane for the patch antenna. (c) The final design revision of the TOPCAT mechanical structure – the aluminium shield and the TOPCAT mother/daughter PCB units act as a separate individual unit, while the antenna and its housing are considered as a second unit that does not have a direct mechanical connection to TOPCAT. (d) The new antenna housing structure. This will be mounted on the solar panels to increase the effective ground plane, with the portion below the 'wings' recessing inside the chassis. (e) Test setup for the complete TOPCAT system. The antenna/solar panel structure represents the proposed mounting design.

5.4.2 Conformity of Receiver and Antenna Specifications

Since UKube-1 consists of both 3.3V and 5V power buses, the initial design proposed to use these resources to operate the receiver at 3.3V and antenna at 5V. However, the power rails specifications stated a tolerance of ±1%, which was not compatible with the

receiver. This is because the voltage tolerance of the Novatel OEMV-1DF receiver is very stringent such that, 3.27V (3.3V-1%) rendered the device inoperable. The active GPS patch antenna selected for the mission also needed a minimum voltage of 5.6V to be powered. These issues necessitated a re-design of the power unit of the payload, where the unregulated battery supply (BatV) of UKube-1 was down converted to the desired voltage values. BatV was thus regulated separately to 3.4V and 5.7V for receiver and antenna operation, respectively.

5.4.3 Timing Conflicts between Communication Buses

During continuous data transfer from payload to platform, the payload was seen to consistently get reset by the watchdog timer (WDT). After extensive investigations the problem was traced back to the priority levels between I2C and SPI interrupts within the microcontroller. The interrupt for SPI, used for communications with the external EEPROM, has a higher priority setting than I2C. Thus, if large amounts of data are available, the microcontroller continues to transfer data without responding to the regular status poll requested by the platform via the I2C bus. Since the platform is programmed to wait for a response or repeat the status poll, the I2C bus is held active throughout the process. This is perceived by the payload microcontroller as the signal lines being busy, thus not servicing the WDT. After a specific duration (determined by the timer) without a response from the microcontroller, the WDT assumes a system malfunction and resets the unit. Since the payload reset frequency increased with an increasing amount of data to be transferred from payload to platform, the issue was resolved by buffering a limited number of packets from the EEPROM into the microcontroller RAM via SPI. Thus, when platform commands a data transfer, only the buffered packets are sent; effectively reducing the time occupied by the SPI bus in between I2C data transfers.

5.5 Space Qualification of TOPCAT

Since TOPCAT was developed mostly using COTS components, vibration, thermal-vacuum (T/V) and radiation tests were performed to ensure its survival at launch and successful operation under orbit conditions. During launch, the satellite experiences strong vibration which can cause significant damage to mechanical structures, both

locally within the payload and the satellite. Operating in a sun-synchronous orbit means that the satellite experiences diurnal variations in vacuum during each orbit, much like local time. The satellite thus experiences considerable temperature variations, resulting in thermal strain of components over successive cycles. Further, the altitude of orbit at ~630 km exposes UKube-1 to radiation levels significantly higher than at ground level on Earth. Accumulation of radiation within electronics can damage their internal structure, rendering the devices inoperable. Moreover, if high energy particles are encountered, it could cause single event upsets (SEUs) that may result in undesirable behaviour of the affected system.

Verification of payload operation following or while being subjected to these harsh conditions requires the exposure of the payload to similar environments. To this end, vibration and thermal/vacuum tests were performed at the facilities in UCL's Mullard Space Science Laboratory (MSSL), while radiation tests were conducted at Synergy Health PLC. It must be noted here that the test sequence is of importance, particularly concerning vibration and thermal/vacuum tests (in that order). This is because mechanical vibration can cause micro-cracks among other effects that may not be visible to the naked eye or produce any immediate functional errors; although continuous operation may result in further degradation of the faulty area. When subjected to thermal cycling however, these cracks can expand and highlight the fault, enabling their identification. Moreover, the same sequence of conditions is experienced by the payload during launch and subsequent deployment into orbit, after which no vibration is experienced. As expected in an engineering project, the test phase was followed by several design revisions to ensure a robust end-product. Where a re-design was not suitable, the vulnerabilities were identified and the risks mitigated. The following sub-sections discuss the results obtained with the final design of TOPCAT, which confirmed a fully functional payload. All tests were conducted on the engineering model at Qualification Level (QL), which qualified the design for space-borne operation. This is in contrast to Acceptance Level (AL) tests, which are performed on flight hardware to confirm flight-readiness of the payload. Due to time constraints imposed on the development of UKube-1, AL tests were conducted by the satellite providers at system-level during full integration of the satellite. They reported TOPCAT as flight-ready and confirmed its successful integration and operation on-board UKube-1.

5.5.1 Vibration Testing

Significant stresses are experienced by satellites due to strong mechanical vibration during the launch process. The modes of vibration translated from rocket to satellite are dependent on the launch vehicle as the vibration profile is determined by the rocket's core design and operation. Specifications for vibration tests are thus defined by the launch provider for satellite and payload(s) separately to emulate the stresses experienced during launch conditions. Noteworthy is the distinction between the post-integration satellite and individual payloads tests. This is because the vibration modes experienced by the internal sub-systems, while similar, does not necessarily reflect that of the complete satellite. It is therefore necessary to subject the standalone payload to vibration conditions that are similar to those that the internal systems are expected to undergo. Of importance is that the payload was operated (for functional checks) only *following* a given set of test and *not during* vibration. This is because, during the launch phase when vibration is experienced the satellite will not be operational – thus faithfully representing the conditions of launch. The vibration test specifications for UKube-1 payloads to which TOPCAT was subjected to are given in Table 5.3.

Table 5.3. Vibration test specifications as determined by the launch providers.

Type of Test	**Specifications**		**Comments**
Resonance Search	The minimum designed natural frequency of the payload shall be >150Hz		
	The natural frequency of the payload shall exceed the resonances of the launch vehicle by a factor of two		
Sine Vibration (all axes)	Pre-test sine sweep from 5 to 2000 Hz		
	Sine sweep between 10-100 Hz @ 4g @ 2 oct/min		
	1" stroke limitation		
Sine Burst (all axes)	40 Hz at 15g		10 cycles
	Post-test sine sweep from 5 to 2000 Hz		Compare pre-test and post-test sweeps
Random Vibration	14.1g RMS for 120 seconds duration (all three axes)		
	Frequency Range (Hz)	Workmanship Level (g^2/Hz)	
	20	0.026	
	20-50	0.026-0.16	@ +6 dB/oct
	50-800	0.16	Maintain
	800-2000	0.16-0.026	@ -6 dB/oct
	2000	0.026	
Shock Load	1 kg between 1kHz and 10 kHz		
	Ramp up from 100 Hz @ 20g		

Tests were performed using a shaker apparatus at the MSSL vibration test facility. The payload unit consisted of the controller board, receiver and the radiation shield, assembled in a similar manner to the flight-version. The antenna and its housing were not included as they were to be integrated to the satellite chassis; thus being considered a part of the platform for vibration purposes. The test procedure was carried out in all three axes (x,y,z) independently, with vibration measured via accelerometers placed around the payload (Figure 5.5). Control accelerometers were also implemented to ensure the specifications in Table 5.3 were reproduced accurately by the shaker apparatus. The test sequence was initiated with a resonance search on each axis as conformation of the resonance behaviour to specification was vital to all other tests. This is because each stage was followed by a post-test resonance search (and functionality test) that would reflect any structural damage suffered from mechanical strain. The following section presents the results for each type of vibration test performed on the 3 axes independently, together with the post-resonance profile. The final outcome of vibration tests on TOPCAT are summarised in section 5.5.1.2.

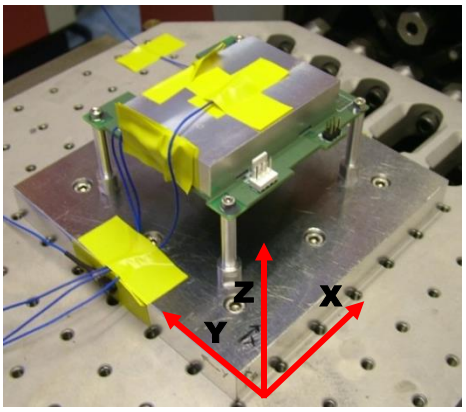

Figure 5.5. TOPCAT secured on the shaker for vibration tests. The reference axes are defined in the figure. Devices attached to TOPCAT (with extending cables) are accelerometers to measure vibration response.

5.5.1.1 Results

x-Axis – The natural frequency was observed at 506.7 Hz, while further resonance was seen at 532.4, 574.8 and 1779 Hz within the test range of 5-2000 Hz. Sine vibration and sine burst responses were compared with the resonance response, with no significant changes observed. Comparison of random vibration and natural frequency responses showed a small downward shift of the resonance frequency between 0.5% and 1%.

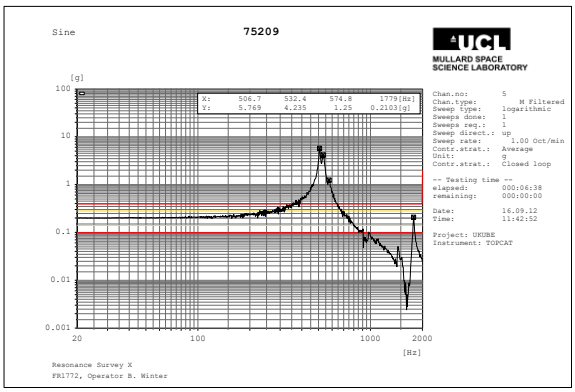

(a)

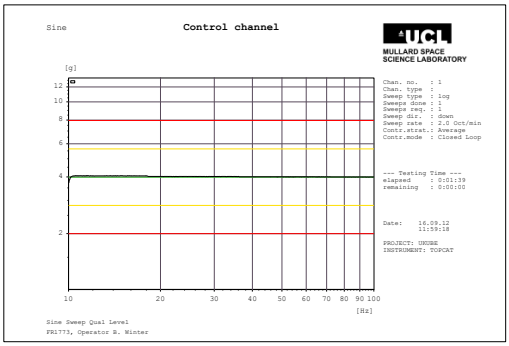

(b)

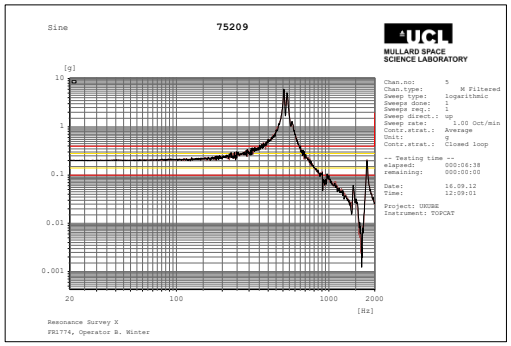

(c)

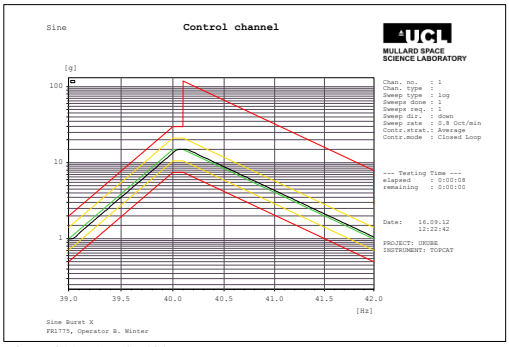

(d)

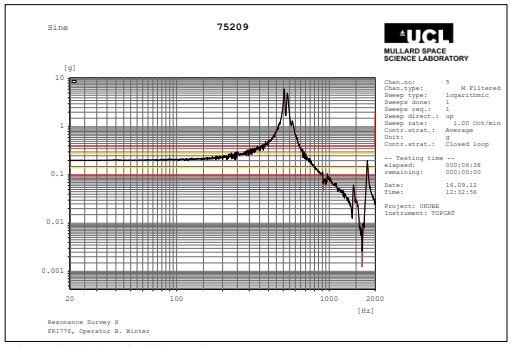

(e)

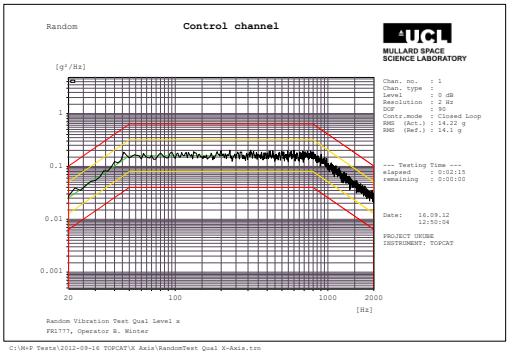

(f)

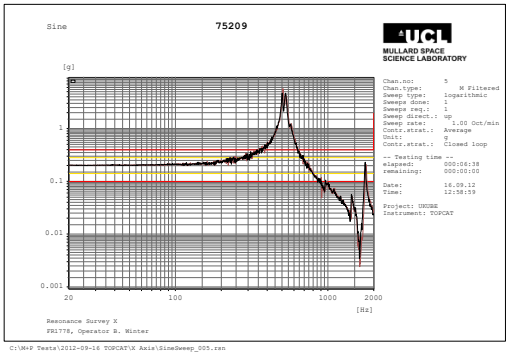

(g)

Figure 5.6. Vibration test results for x-axis. (a) The resonance search shows a natural frequency at 506.7 Hz. (b) Sine vibration result with the control channels, and post-vibration resonance search (c) showing no change from (a). (d) Sine burst result with the control channels, and post-vibration resonance search (e) showing no change from (a). (f) Random vibration results with the control channels, and the post vibration resonance search (g) showing a small downward shift of the natural frequency by 0.5-1%.

y-Axis - The natural frequency was observed at 504.4 Hz, while further resonance was seen at 522.9, 564.5 and 901.5 Hz within the test range of 5-2000 Hz. Sine vibration, sine burst and random vibration responses were compared with the resonance response, with no significant changes observed.

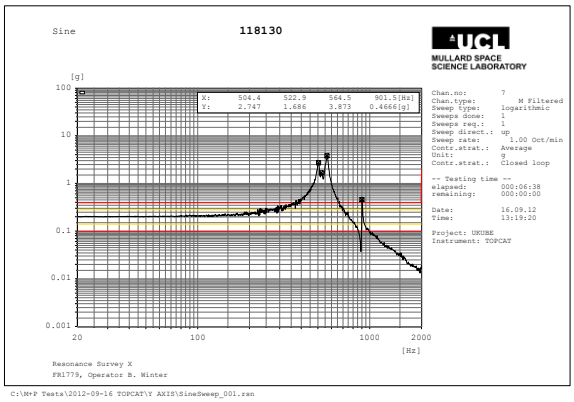

(a)

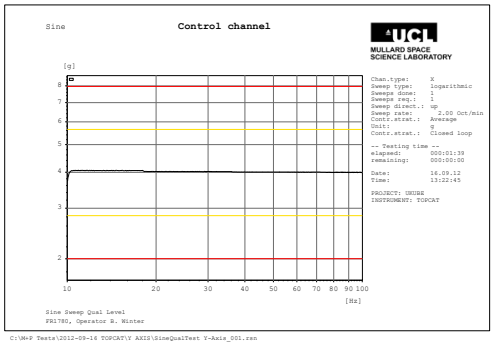

(b)

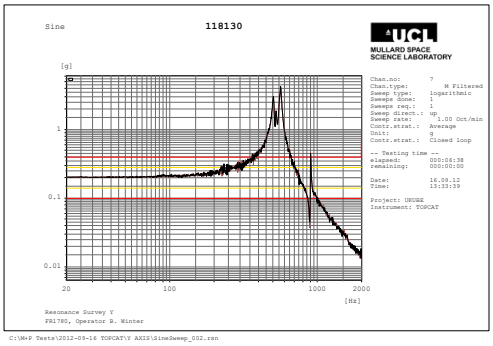

(c)

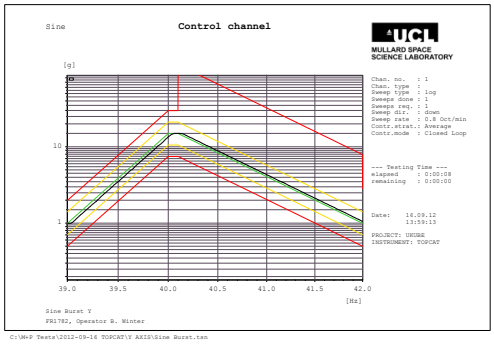

(d)

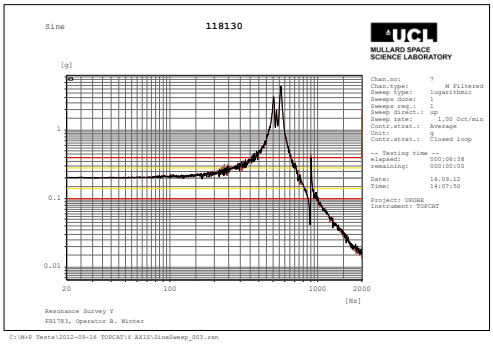

(e)

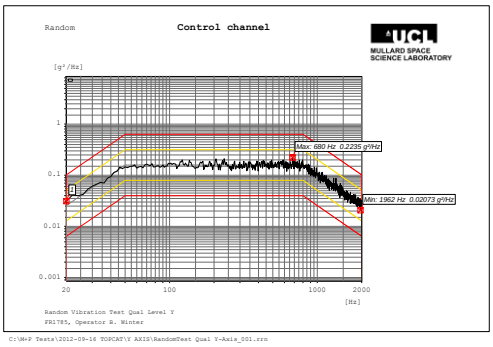

(f)

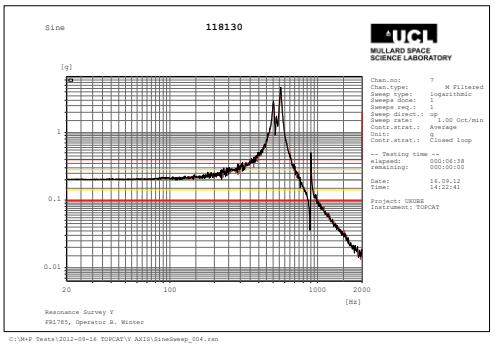

(g)

Figure 5.7. Vibration test results for y-axis. (a) The resonance search showing a natural frequency at 504.4 Hz. (b) Sine vibration result with the control channels, and post-vibration resonance search (c) showing no change from (a). (d) Sine burst result with the control channels, and post-vibration resonance search (e) showing no change from (a). (f) Random vibration result with the control channels, and post-vibration resonance search (g) showing no change from (a).

z-Axis – The natural frequency was observed at 392.0 Hz, while further resonance was seen at 504.4, 537.2, 567, 1075 and 1414 Hz within the test range of 5-2000 Hz. Sine vibration, sine burst and random vibration responses were compared with the resonance response, with no significant changes observed.

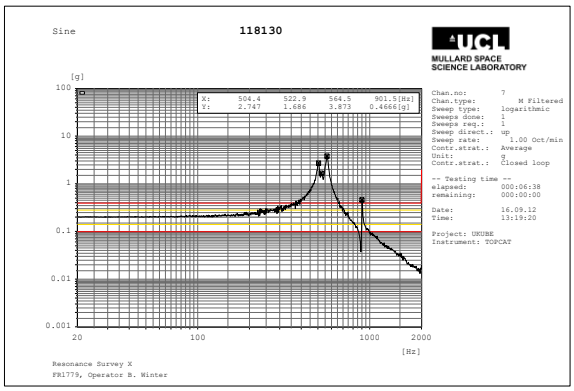

(a)

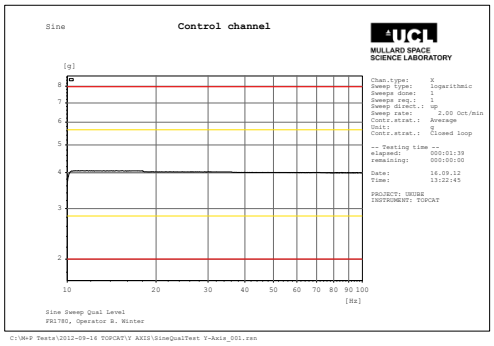

(b)

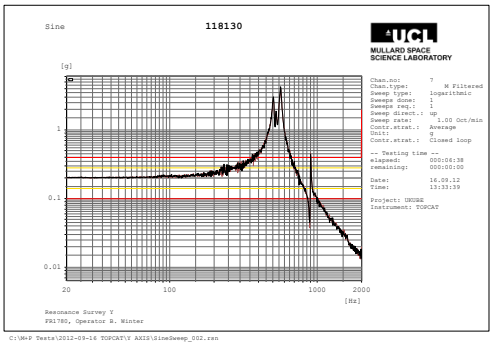

(c)

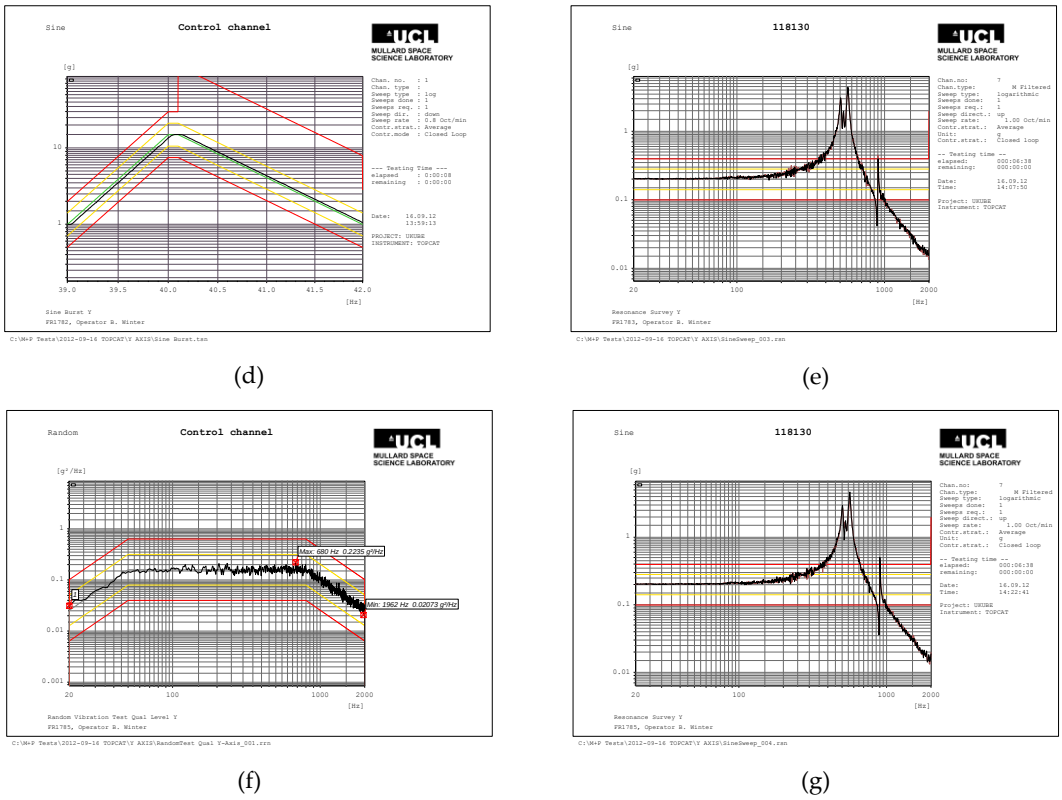

Figure 5.8. Vibration test results for z-axis. (a) The resonance search showing a natural frequency at 392.0 Hz. (b) Sine vibration result with the control channels, and post-vibration resonance search (c) showing no change from (a). (d) Sine burst result with the control channels, and post-vibration resonance search (e) showing no change from (a). (f) Random vibration result with the control channels, and post-vibration resonance search (g) showing no change from (a).

5.5.1.2 Discussion

TOPCAT successfully completed all tests with no significant or permanent mechanical stresses/strains on the payload. The lowest natural frequency was observed to be 392.0 Hz in the z-axis, well above the limits specified as required. Although the natural frequency response in the x-axis following the random vibration test showed a downward shift, this was attributed to the settling of the TOPCAT module during the test rather than any structural degradation [*Winter*, 2012]. This was confirmed by the y-axis random vibration test response, where no shifts were observed. The TOPCAT payload was thus qualified for flight, barring the antenna and its housing; which was not tested due to their placement on the solar panel. Further details on the vibration test procedure and results are provided in a test report in Appendix A2.1.

5.5.2 Thermal/Vacuum (T/V) Testing

T/V tests emulate the environment TOPCAT would be exposed to and operate in during its mission. As the payload would experience harsh temperatures and vacuum conditions, it was vital to ensure all components functioned as intended without

material outgassing. T/V tests were thus conducted together with functional tests, where the payload operation was monitored *throughout* the procedure. This was in contrast to vibration tests, where functionality checks were performed *after* each test, as the satellite would only be operated after launch (when vibration is experienced). Also of importance is that the T/V test was conducted *following* the payload's exposure to vibration. This was because, in addition to correctly simulating the launch-orbit sequence, any micro-scale mechanical damage would have been magnified under repeated thermal cycles, effectively highlighting any structural faults. Table 5.4 gives the thermal/vacuum test specifications to emulate the orbit environment of TOPCAT – i.e. a sun-synchronous orbit at ~630 km. The thermal cycle profile is given in Figure 5.9 [*Greenland and Warren*, 2011]. .

Table 5.4. Thermal specifications for T/V testing.

Test	**Temperature (Tolerance) °C**
Ambient Temperature	15-25
Non-operating maximum	+70 (+3)
Operating maximum	+55 (+3)
Non-operating minimum	-35 (-3)
Operating minimum	-20 (-3)
Soak time: 2 hours	
Rate of change of temperature: ±5°C/minute	
Temperature tolerance: ±3°C	
Number of T/V cycles: 8	

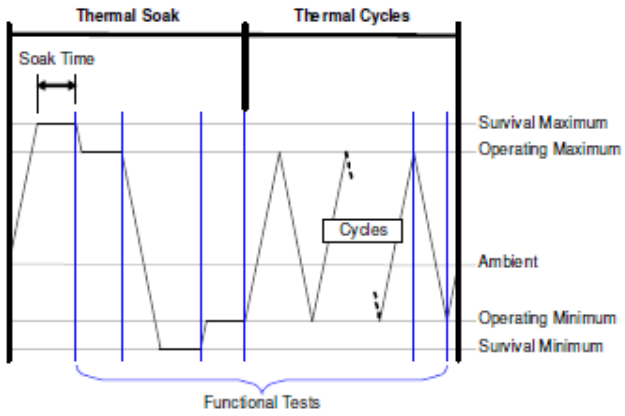

Figure 5.9. Profile of the thermal cycling specifications for T/V testing [*Greenland and Warren*, 2011].

The tests were carried out in a T/V chamber, where the temperature was controlled through liquid nitrogen and a heating element. The temperature was monitored and controlled via a closed-loop feedback system with Platinum Resistor Thermometers (PRTs) acting as sensors. Since a vacuum environment is a poor heat conductor and

thermal distributor, the temperature controls were carefully monitored to prevent undesirable deviations from the specified limits. 10-layers of multi-layer insulation (MLI) was also placed around the payload for thermal isolation and to ensure an even temperature distribution across TOPCAT. Once successfully installed, a functional test was performed as a control to ensure any failures were solely due to the T/V environment in which it would be operating. Figure 5.10 shows TOPCAT prepared for T/V testing, before and after being enclosed in MLI.

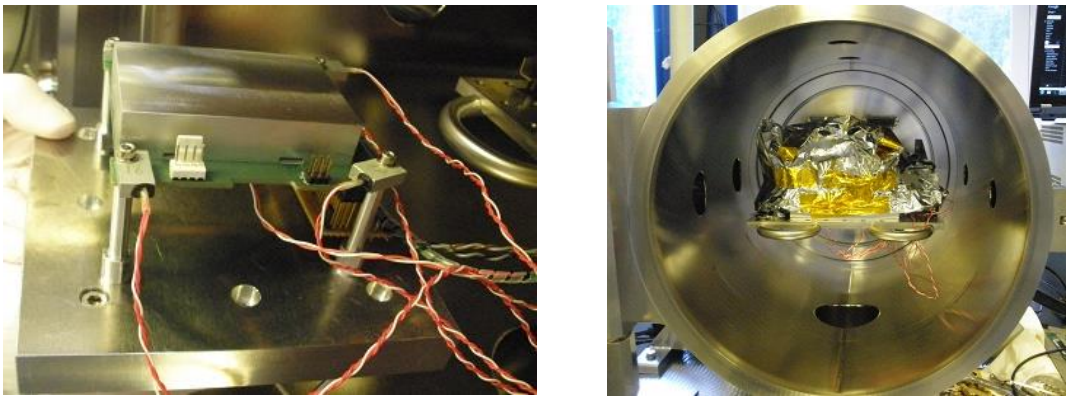

(a) (b)

Figure 5.10. TOPCAT under preparation for T/V testing. (a) Inserting TOPCAT into the chamber (before wrapping in MLI) with PRTs attached at the four corners to monitor board temperature. (b) Final T/V test setup within the chamber with MLI for thermal isolation.

5.5.2.1 Results

Figure 5.11 gives the thermal cycle profile for TOPCAT, as measured from within the chamber. The payload was exposed to six cycles of temperature variations, with the first acting as the soak period to test for survival. TOPCAT was thus tested through five thermal cycles, when functionality was monitored. Although considered a vacuum, the chamber had a nominal pressure of ~10^{-6} mBar, regarded as negligible for test purposes. Variations in the pressure reflected that of the thermal cycles and ranged between 10^{-7} and 10^{-5} mBar. This was due to thermal expansion/contraction of the environment and was as expected. Functional tests were performed at both operational limits as well as during selected transitions in the operational range. The latter was done to emulate conditions that would be experienced by TOPCAT when the satellite transits from day to night and vice versa. All tests were successful and no expanded micro-cracks were observed either visually or functionally. TOPCAT was thus qualified to operate in its intended orbit environment, following vibration conditions experienced during its launch.

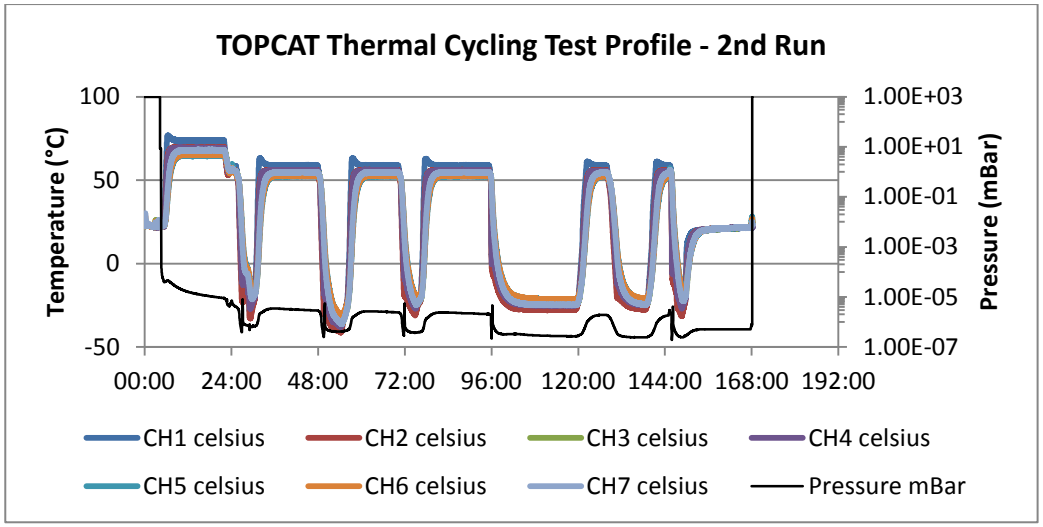

Figure 5.11. TOPCAT thermal profile during T/V testing. All coloured plots represent the different PRT sensors attached to the setup. The plot in black shows the pressure within the chamber (ideally, vacuum) – which also sees a small variation correlated with the thermal cycles. This is due to thermal expansion.

5.5.2.2 Discussion

Although the general thermal profile was set up as per specifications, a number of deviations were necessary to conduct the test pragmatically. In order to ensure soak temperatures were achieved with minimal departure from the specified limits, the thermal control system required more than two hours to stabilise the temperature of TOPCAT at non-operating limits. Execution of the test was also affected by time restrictions, as unsupervised operation of the setup was not permitted. In these circumstances, the temperature was maintained at ambient values until appropriate supervision could be provided to monitor operation. These deviations, while representing the sun-synchronous orbit to a lesser extent, were of minimal impact to the integrity of the test. This is because the resultant effect of adopting the practical approaches was over-qualification of the board during prolonged soaking at the non-operating maximum and resting at ambient temperatures – neither of which can render the test invalid. Of more concern was the reduction of the thermal cycles from a specified eight to five, which was also due to timing and scheduling limitations. This was however deemed acceptable, as a previous thermal test run was performed for 12 cycles on a precursor to the final design. Although not identical, the designs were sufficiently similar to qualify the final version of TOPCAT as a space-ready payload from successful operation over only 5 cycles. A detailed log of the test process is given in Appendix A2.2. It is important to note that, while the test qualified TOPCAT on a payload-level, a further

vibration-thermal-vacuum test cycle was required following satellite integration to qualify the complete system (including the antenna) as flight-ready.

5.5.3 Radiation Testing

At an orbit altitude of ~630 km, UKube-1 – and by extension TOPCAT – would be exposed to two types of radiation: Total Ionising Dose (TID) and energetic particle. TID is caused by low energy radiation, and has a cumulative effect over the mission lifetime. Effects include temporary leakage (or dark) currents in satellite electronics and degradation of gate-oxide/insulating layers in semiconductor components, which results in more permanent damage. In contrast, High Energy (HE) particles originating from cosmic rays are energetic enough to pass through the entire satellite, possibly causing temporary Single Event Effects (SEEs) along its path.

Testing for radiation hardness of TOPCAT was important as the controller board was developed from simple COTS components, whose behaviour under radiation exposure had not been characterised. The payload was thus tested for TID radiation to understand long term effects and expected failure timescales during its mission lifetime. HE particle radiation was not tested against since CubeSat designs are inherently not protected against HE radiation. Noteworthy is that, since TID testing allows characterization of the payload's radiation hardness and identification of failure modes, it was a destructive test by nature. As such, only the payload controller board was tested covered by a 2mm thick aluminium shield (as shown in Figure 5.5, Figure 5.10(a)), placed to protect the internal electronics against radiation damage. The receiver and antenna were represented by equivalent resistors that emulated their load conditions. The exclusion of the payload instruments were justified, as both devices were designed for space-based applications.

Specifications for TID testing are typically determined based on the orbit, altitude and duration of mission. For UKube-1 in a sun-synchronous orbit at ~630 km altitude, the expected TID was not more than 15 krad during its mission lifetime of one year. As it was not viable to conduct real-time tests over a year due to a short turn-around timescale (<18 months), irradiation was accelerated by exposing TOPCAT to 1.5 krad per hour for 10 hours from a Cobal-60 gamma source; effectively emulating the radiation the payload is exposed to throughout its mission. The outcome of the test was determined by monitoring the current consumption and through continuous functional tests. The final

TID required for radiation damage were calculated for different components from the rate of TID accumulation (1.5krad/hour) and the time taken for the damage to be detected.

5.5.3.1 Results

Figure 5.12 shows the current consumption of TOPCAT from both 5V and BatV power rails monitored during the test procedure. The red vertical marker at 16:32:01 hours, representing approximately 6.5 months into the mission (or ~8.25 krad TID), indicates the initial point of failure of TOPCAT. This was identified through corrupted data received from the payload controller board, and the position was strongly co-located with the sharp rise in current consumption from the BatV supply. The software failure was associated with the EEPROM/microcontroller as the errors were seen within the data packets received by the platform. The 'dummy' data were generated by the microcontroller and transferred onto the EEPROM for storage, which were then read back into a RAM buffer when data was requested by the platform. Since all other components appeared to function successfully, the fault was deemed to be associated with the EEPROM and/or microcontroller, where the data were stored and generated, respectively. Despite the fault, TOPCAT continued to function at this time, although with sporadic bouts of data corruption.

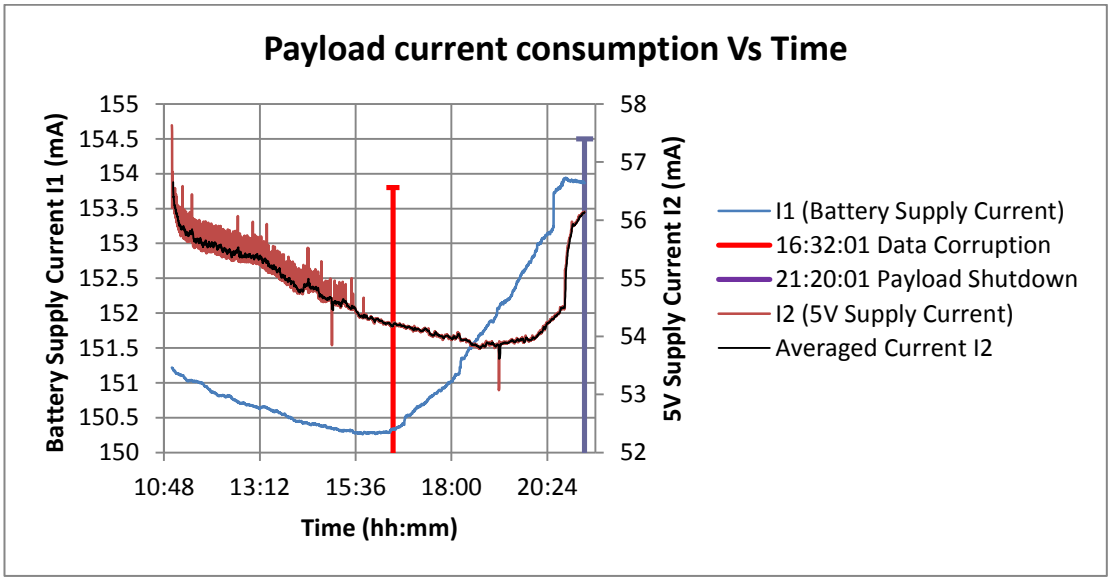

Figure 5.12. TID radiation test results for TOPCAT. The blue graph represents current consumption by TOPCAT from the BatV supply, while the red/black graphs are current consumption from the 5V supply. The red vertical marker @ 16:32:01 (~8.25kRad) indicates a point of failure of TOPCAT, as identified from corrupted data. The position is strongly correlated with the sharp rise in current in BatV. TOPCAT was still functional, albeit with sporadic corrupted operation. An even steeper change in current usage is seen in both supplies closer to the end of the test run (i.e. closer to 15kRad TID).

In addition to the payload degradation indicated at 16:32:01 hours, an abrupt rise in current consumption was observed from both power supplies closer to the 10th hour (past 20:24 hours) of irradiation. Although no functional failures were discerned during operation, post-irradiation functional tests revealed that the microcontroller was unable to access the EEPROM and a memory-write could not be performed on the flash memory of the microcontroller. Based on the evidence in Figure 5.12, the damage was inferred to have occurred toward the end of the test run at approximately 11.4 months into the mission (~14.25 krad). As mentioned before, TID effects on electronics may be temporary or permanent, depending on the type of damage to the device. This was reflected during operational tests in the days following irradiation, which showed normal current consumption from both power supplies. Re-soldering the EEPROM to ensure good contact between surface mount points also restored normal EEPROM operation. In contrast, the microcontroller flash memory suffered permanent damage whereby it could not be programmed, although memory-reads were still possible.

5.5.3.2 Discussion

Concerning the first observed functional error, it is important to consider that the sudden change in current gradient coinciding with the data corruption was of the battery supply (BatV) rather than the 5V rail. BatV supplied power only to the receiver and antenna – represented by resistor loads in the test setup – and the voltage regulators, while the 5V supply powered the microcontroller, EEPROM and all other peripheral electronics. Thus, the correlation between the EEPROM-microcontroller related error and rise in BatV current consumption may be attributed to the degradation of one (or both) of the voltage regulators powered by the BatV supply. This may have had an indirect effect on microcontroller operation through its outputs to the regulators that control their switching – such as leakage current being injected into the microcontroller via the enable inputs of the regulators.

Results of the radiation test presented in section 5.5.3.1 revealed the components of TOPCAT most susceptible to radiation damage and their potential lifespan. The voltage regulators on the controller board seemed to accumulate approximately 8.25 krad before any faults were detected, which was equivalent to a component lifetime of ~6.5 months in the expected radiation environment. The apparent hard failure of the EEPROM and microcontroller occurred at an approximate TID of 14.25 krad, which translated to 11.4

months in the mission lifecycle. This was acceptable as the payload would be in operation for 95% of its lifetime, albeit with some data corruption in the latter half of the year. It must be appreciated that only circumstantial conclusions could be drawn in determining component failure (and their cause) since extensive investigations were not conducted on radiation damage processes. However, this was deemed sufficient as only component qualification was required to ensure successful operation of the payload in orbit. In light of the results, the final design was updated to install a shield with an increased wall thickness of 3mm that would enhance TOPCAT's survival probability during its mission.

5.6 Summary and Conclusion

TOPCAT is a dual-frequency GPS receiver-based instrument installed as a payload in the 3U CubeSat 'UKube-1' to image the topside ionosphere and plasmasphere. The satellite was launched on 8 July 2014 to a sun-synchronous LEO orbit at an altitude of ~630 km. TOPCAT was realised through the integration of a commercial receiver (configured for orbit conditions) and antenna with controller electronics designed from COTS components. Development of TOPCAT saw a number of challenges, particularly related to the GPS receiver antenna performance. Design constraints imposed by CubeSat specifications resulted in an insufficient ground plane and a compromised viewing angle for the antenna, causing a degradation of the received signal. Other issues included non-conformity of the receiver and antenna to the satellite's supply voltage specifications, and timing conflicts between payload communication buses. Several design cycles were required for the challenges to be resolved or mitigated.

Since the COTS components in TOPCAT are not space-graded, tests needed to be performed under launch and orbit conditions to qualify the design as space-worthy. Vibration tests were carried out on the payload that emulated the launch environment, while thermal-vacuum and radiation tests simulated the operating environment of the orbit. Results of these ground tests demonstrated that TOPCAT would successfully operate following exposure to launch stresses and T/V conditions. Radiation tests revealed that the components would survive 95% of its mission lifetime. This was

addressed by taking measures to increase the shield thickness in the final design, effectively improving the survival probability during its mission lifetime of one year.

Provided data analysis confirms the feasibility of TOPCAT for successful imaging of the topside ionosphere and plasmasphere, the development of a constellation of CubeSats is intended for global and time-continuous coverage of the upper reaches of the ionised atmosphere. The motivation for this endeavour is the potential to perform high quality ionospheric/plasmaspheric science with cost-effective technology and COTS components. Indeed, the establishment of a tomography algorithm to support such a system is discussed in Chapter 6. At the time of writing, UKube-1 has been successfully launched and is currently in its commissioning phase.

6 Topside Ionosphere-Plasmasphere Imaging with MIDAS

6.1 Introduction

With the successful placement of TOPCAT in LEO (Chapter 5), the next phase of the research is to validate the inversion algorithm MIDAS to image the topside ionosphere and plasmasphere. The Multi-Instrument Data Analysis System (MIDAS), as introduced in Section 4.4, employs tomographic inversions to image the electron distribution in the ionosphere. The suite of algorithms use phase measurements from dual-frequency systems – primarily GPS – to derive slant TEC along the signal paths, which is then inverted to produce maps of electron concentration of the region of interest. Developed for upper atmospheric research, the use of the software for spatial and temporal imaging of the ionosphere has been well established. Its implementation for regions above the ionosphere however, is yet to be seen due to the different dynamics present, relative to the ionosphere. In contrast to the complex production, loss and transport mechanisms in the lower regions, the plasma distribution in the topside ionosphere and plasmasphere is largely governed by the geomagnetic field (Chapter 2 and 3). This chapter discusses the extension of MIDAS to image these higher altitudes using the TEC derived from GPS phase measurements, and follows the work carried out by *Spencer and Mitchell*, [2011].

The chapter first describes the adaptation of MIDAS to image the topside ionosphere and plasmasphere, which is realised through the use of a priori knowledge that is more conducive to describing regions beyond the ionosphere. The method undertaken to validate the modified set of algorithms is then discussed, where both simulated and true COSMIC GPS data are used to image the upper regions. The results are presented in the following section, which includes a qualitative comparison of the images from COSMIC data against independent observations made using both COSMIC and Jason-1 measurements (discussed in Chapter 3) to ensure the veracity of the reconstructions. The chapter is closed with a discussion of the results and a conclusion that highlights possible future work that could further improve topside ionospheric-plasmaspheric imaging with MIDAS.

The results in this chapter together with the methodology in Subsection 4.4 will be submitted to the Journal of Geophysical Research in the near future.

6.2 MIDAS for the Topside Ionosphere-Plasmasphere

First results from the extension of MIDAS to include the topside ionosphere and plasmasphere were produced by [*Spencer and Mitchell*, 2011]. TEC was measured by POD antennas of the COSMIC GPS receivers, thus enabling reconstruction of the global electron concentration from an altitude of ~800 km to 20,200 km, effectively isolating the region.

As described in Section 4.4, the original version of MIDAS developed for the ionosphere contains basis functions that describe the electron concentration morphology specific to the local region, which is based on plasma properties. In contrast, particle motion in the topside ionosphere and plasmasphere is influenced largely by the geomagnetic field. Thus, to image these higher altitudes correctly, MIDAS requires basis functions that incorporate the physics governing the regions. [*Spencer and Mitchell*, 2011] achieved this by substituting the original basis functions with a description of a dipole magnetic field in terms of Euler potentials α and β:

$$\alpha = \frac{\sin \lambda^2}{r_{Vox}} \tag{6.1}$$

$$\beta = \phi \tag{6.2}$$

where, λ and ϕ are magnetic latitude and longitude and r_{Vox} is the radius of the voxel of interest. The magnetic field $\boldsymbol{B}$ is described through Euler potentials as [*Stern*, 1970]:

$$\boldsymbol{B} = \nabla\alpha \Lambda \nabla\beta \tag{6.3}$$

The mapping matrix **X** defined in equation (4.15) thus linearly transforms the spatial grid of λ, ϕ and r_{Vox} to a 2-dimensional quantized Euler space through interpolation with a reconstruction resolution of $\delta\alpha$ and $\delta\beta$ at each time step.

In addition to the process described by equations (4.14)-(4.18), the algorithm also introduces quadratic smoothing in space and time to minimize any artefacts produced during the inversion. This is expressed in matrix form as,

$$[(\mathbf{AX})^{-1}(\mathbf{AX}) + \eta(\mathbf{RX})^{-1}(\mathbf{RX})]\mathbf{W} = (\mathbf{AX})^{-1}\boldsymbol{b} \quad (6.4)$$

where $\boldsymbol{R}$ is the regularization matrix and η specifies the relative weighting between observations and regularization.

Since only a maximum of six receivers are available at any given time, a longer time duration than that used for the ionosphere is needed to collect sufficient data for the inversion; which needs to be considered against the temporal evolution of the topside ionosphere-plasmasphere. In contrast to time-dependent ionospheric reconstructions in [*Mitchell and Spencer*, 2003], [*Spencer and Mitchell*, 2011] used data averaged over 3-hours with the time window extending for 33 hours to provide evolutionary a priori information.

6.3 Validation of MIDAS for the Topside Ionosphere-Plasmasphere

The results presented in this section are an extension of the work carried out by [*Spencer and Mitchell*, 2011], where MIDAS is validated for the use of topside ionospheric/plasmaspheric imaging. Year-long data from 2009 is used in this validation as the year lies in a solar minimum, when solar- and geomagnetic-activity are lowest. Consequently, the plasmasphere exists in a 'quiet' state with minimal or no storm-induced structures, which is optimal to investigate and understand the performance of the new algorithm.

In the first phase, ray path geometry between GPS satellites and COSMIC receivers throughout the year are used to undertake a computer simulation using an empirical topside ionosphere-plasmasphere model by [*Gallagher et al.*, 1988] ('Gallagher model', hereafter). This allows the new technique to be tested and benchmarked against a case where the plasmasphere is modelled, ensuring the correct answer is known. The algorithm is then used with true differential phase from COSMIC GPS POD antennas of the receivers for the same year (2009). Validation is achieved by qualitatively comparing the reconstructions against features previously observed by [*Pedatella et al.*, 2011; *Lee et al.*, 2013].

The COSMIC GPS data used in the validation are obtained in RINEX format from the UCAR COSMIC database, available from [http://cdaac-www.cosmic.ucar.edu/cdaac/products.html]. Noteworthy is that, although six satellites are available in the constellation, their operation during the year 2009 was observed to be intermittent. Particularly, some orbit data providing receiver positions appear to be compromised, although dual-frequency phase measurements are available when the orbit data are missing. The orbits are recovered by substituting the position data from a future complete orbit. Drift and perturbations are accounted for by minimizing differences between the ground tracks of the two orbits.

Following the acquisition of phase and orbit data, a three dimensional grid is defined in geomagnetic coordinates for the topside ionosphere-plasmasphere. The radial aspect extends from 600 km to 20,200 km altitude with a step-size of 1000 km, while the geomagnetic latitude and longitude dimensions have a step-size of 10° and 20°, respectively. Pole-to-pole latitudes are used in the inversion, although the plasmasphere only extends to regions of the closed magnetic field lines of ~±50° geomagnetic latitude. This is to ensure that ray path geometries towards the edge of the plasmasphere are not discarded during reconstructions. Following the reconstruction, the analysis considers a limited latitude range of ±40° for the simulation (due to model limitations) and ±50° for real data. In order to ensure only direct LOS ray paths are considered, an elevation cut-off of 40° is also imposed that effectively eliminates any occultation data from the inversion.

6.3.1 Reconstruction of the Gallagher Model

The empirical model by [*Gallagher et al.*, 1988] is used to simulate the procedure of imaging the electron concentration in the topside ionosphere and plasmasphere. The model was based on the data from the Retarding Ion Mass Spectrometer (RIMS) onboard Dynamics Explorer-1 (DE-1). It describes the steady state low energy proton distribution in the plasmasphere, while the topside ionosphere is modelled using a modified chapman layer. The model was developed by Gallagher et al. using RIMS data collected for a magnetic latitude range of ±40° between 0000 hrs and 1200 hrs MLT, obtained during moderate geomagnetic activity immediately following a solar maximum.

6.3.1.1 Method

The proton concentration described by the Gallagher model is translated to an electron concentration in MIDAS by assuming quasi-neutrality of the medium. The electron concentration is simulated within each voxel of the spatial and temporal grids defined earlier. Ray path geometries through the simulation (***A***) required by the algorithm are generated between GPS and COSMIC satellites; the latter providing receiver positions at the time of signal reception, sampled every 60 seconds. The simulated TEC 'observations' (***b***) at the receiver are then inverted to reconstruct the topside ionosphere-plasmasphere model.

Although applying the same 3-hour temporal resolution used by [*Spencer and Mitchell*, 2011] ensures sufficient data coverage for the inversion, the longer window means that any fast evolving (<3-hours) structures will not be faithfully reconstructed. To determine the effects of this, the inversion process of the model simulation is conducted with both 1-hour and 3-hour time resolutions. Considering both coverage and quality of reconstruction, a suitable time resolution is then selected to proceed with the validation using true COSMIC GPS data.

Figure 6.1 shows the Gallagher model for the topside ionosphere-plasmasphere simulated by MIDAS for the 3-hour resolution (averaged data) at two time steps: 0300-0600 hours UT and 0600-0900 hours UT. Although the model is applied to simulate the topside ionosphere-plasmasphere globally, only the latitude range ±40° is considered when evaluating the quality of reconstruction. This is because the model is only valid for the limited latitude range. The model also only incorporates diurnal variations.

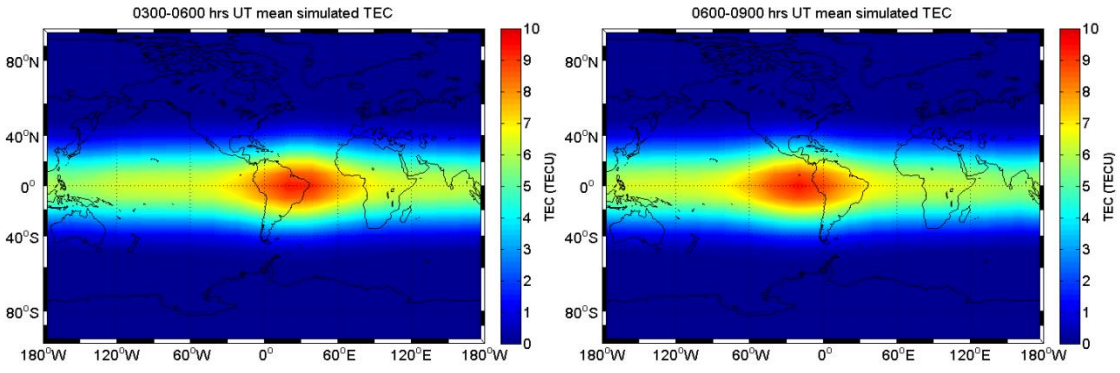

(a) (b)

Figure 6.1. Simulated average electron concentration by MIDAS of the topside ionosphere and plasmasphere over 3 hours for ±90° geomagnetic latitude at two time steps described by the Gallagher model. (a) 22 May 2009 0300-0600 hours UT. (b) 22 May 2009 0600-0900 hours UT.

6.3.1.2 Results

As mentioned in Section 6.3.1.1, reconstruction of the Gallagher simulation is carried out using both 3-hour and 1-hour time resolutions. This is to identify the optimum resolution for imaging plasmaspheric structures that would also provide good ray path coverage across the spatial grid. The 3-hour (averaged data) time resolution uses a 33-hour window containing 11 3-hour time frames, centred on the time of interest. Observations from all time frames contribute to the central time through a regularization process, which linearly constrains the evolution of dynamics and prevents any large or abrupt changes in electron density through successive frames. The contribution of multiple frames (i.e. windows) also provides better ray path coverage, which may otherwise not be available if only the 3 hours of interest (i.e. frame of interest) were considered. In contrast to the 3-hour time frames, the 1-hour time resolution uses 11 1-hour frames, effectively increasing the time resolution but reducing the coverage contributing to the time of interest.

Reconstructions of the simulation using the two time resolutions and respective ray path coverages are shown in Figure 6.2 and Figure 6.3. Two time windows for 22 May 2009 – 0300-0600 and 0600-0900 hrs UT for 3-hour resolution, and 0300-0400 and 0600-0700 hrs UT for 1-hour resolution – are considered to demonstrate the evolution of the simulated plasmasphere and its effect on the reconstructions. Although the simulation only represents diurnal variations, it is important to consider the day of the year for reconstructions as the ray path coverage is not consistent and has a significant bearing on the quality of the reconstruction.

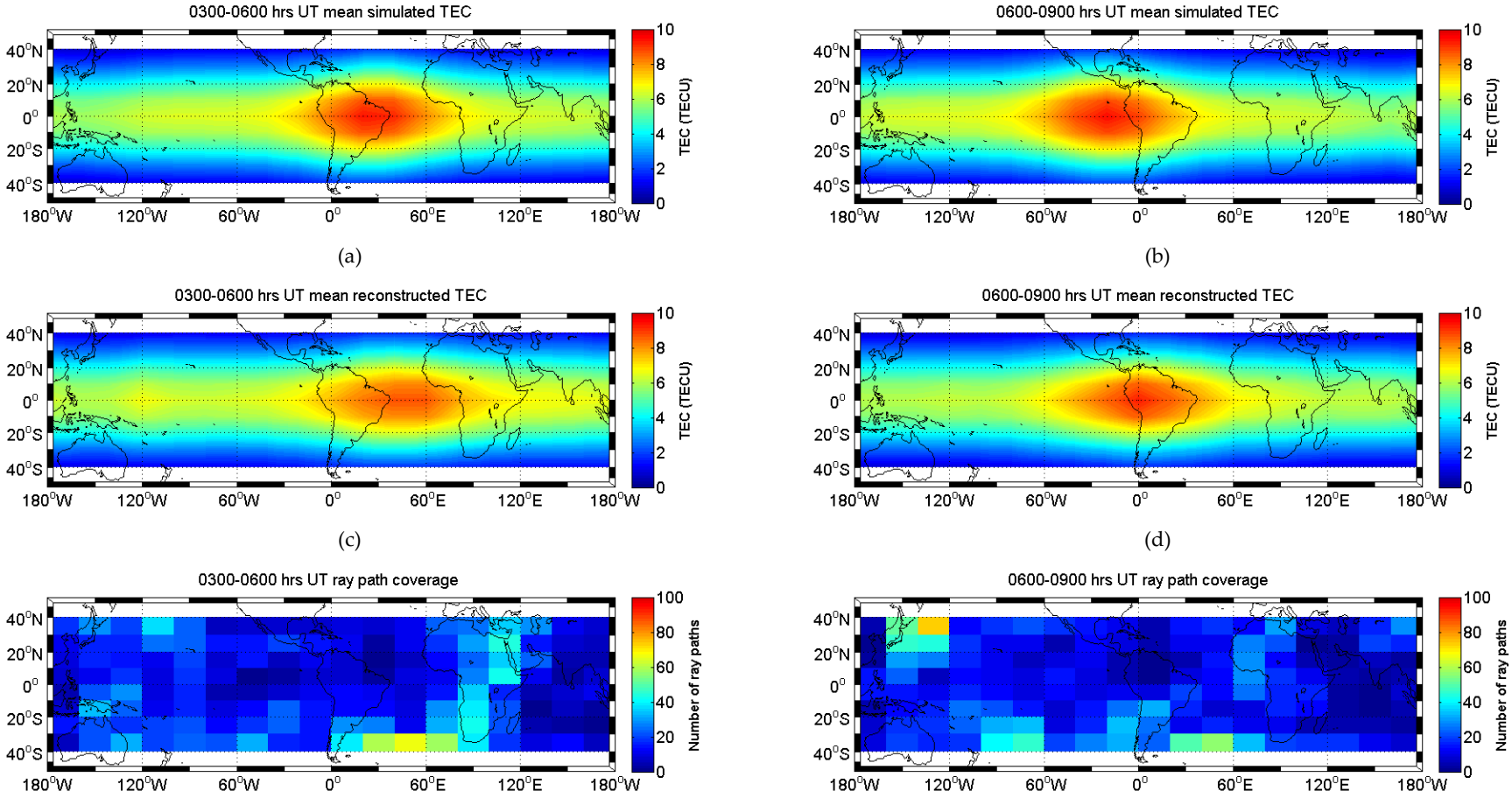

Figure 6.2. 3-hour reconstructions of the Gallagher simulation (of plasmaspheric TEC) for 22 May 2009 from 0300-0900 hours UT with raypath coverage. (a), (b) Plasmaspheric TEC from the Gallagher simulation for 0300-0600 hours UT and 0600-0900 hours UT, respectively. (c), (d) Reconstruction of the simulation through MIDAS for the same time durations. (e), (f) Ray path coverage at each time duration.

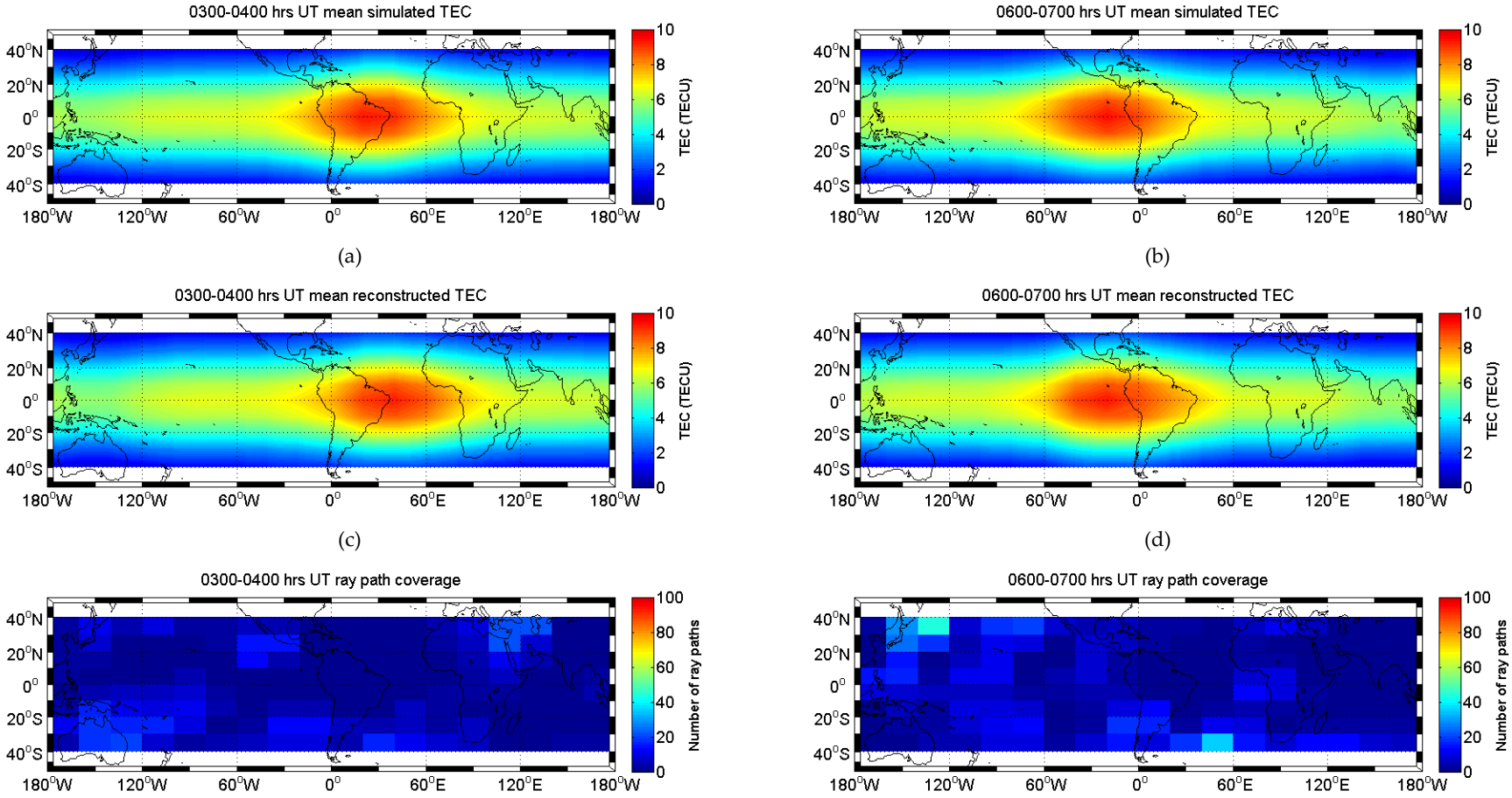

Figure 6.3. 1-hour reconstructions of the Gallagher simulation (of plasmaspheric TEC) for 22 May 2009 from 0300-0400 hours and 0600-0700 hours UT, with raypath coverage. (a), (b) Plasmaspheric TEC from the Gallagher simulation for 0300-0400 hours UT and 0600-0700 hours UT, respectively. (c), (d) Reconstruction of the simulation through MIDAS for the same time durations. (e), (f) Ray path coverage at each time duration.

Figure 6.4 gives the percentage error between the simulations and reconstructions at each time step to quantify the quality of reconstruction for both time resolutions. Results show that the inversion using a 1-hour time frame with an 11-hour time window (Figure 6.3) represents the simulation better than that performed with a 3-hour time frame using a 33-hour time window (Figure 6.2). This is because, the structures of the Gallagher model evolve significantly over 3 hours, resulting in considerable discontinuation between two consecutive time windows. Therefore, given the limited observations from only six receivers, the window of 33-hours has a stronger influence on the solution than the observed data itself. Considering inversions with an 11-hour time window, although the solutions appear to represent the simulation more faithfully, two factors need to be considered: 1) the evolution of structures in the model through two consecutive time steps is more continuous and thus less realistic, making the solution easier to compute, and 2) the number of observations compared to the number of unknowns (i.e. electron density along field lines) per inversion for one hour is very small, resulting in the problem being further under-constrained. The latter is particularly important when reconstructing the true plasmasphere, which has more structures than a model simulation. Both these factors mean that, when imaging the plasmasphere using observed differential phase measurements, the 3-hour time resolution will be more reliable due to the higher number of observations per voxel. Indeed, this means the algorithm is only suitable for the quiet-time plasmasphere which has slower evolving structures (<3 hours). Reconstruction of a more active (storm-time) plasmasphere will be possible in the future, provided there is a better availability of observations due to a higher number of either satellites or receivers; thus allowing for an increase in the algorithm's time resolution (e.g. 1-hour time frames) to image more dynamic structures.

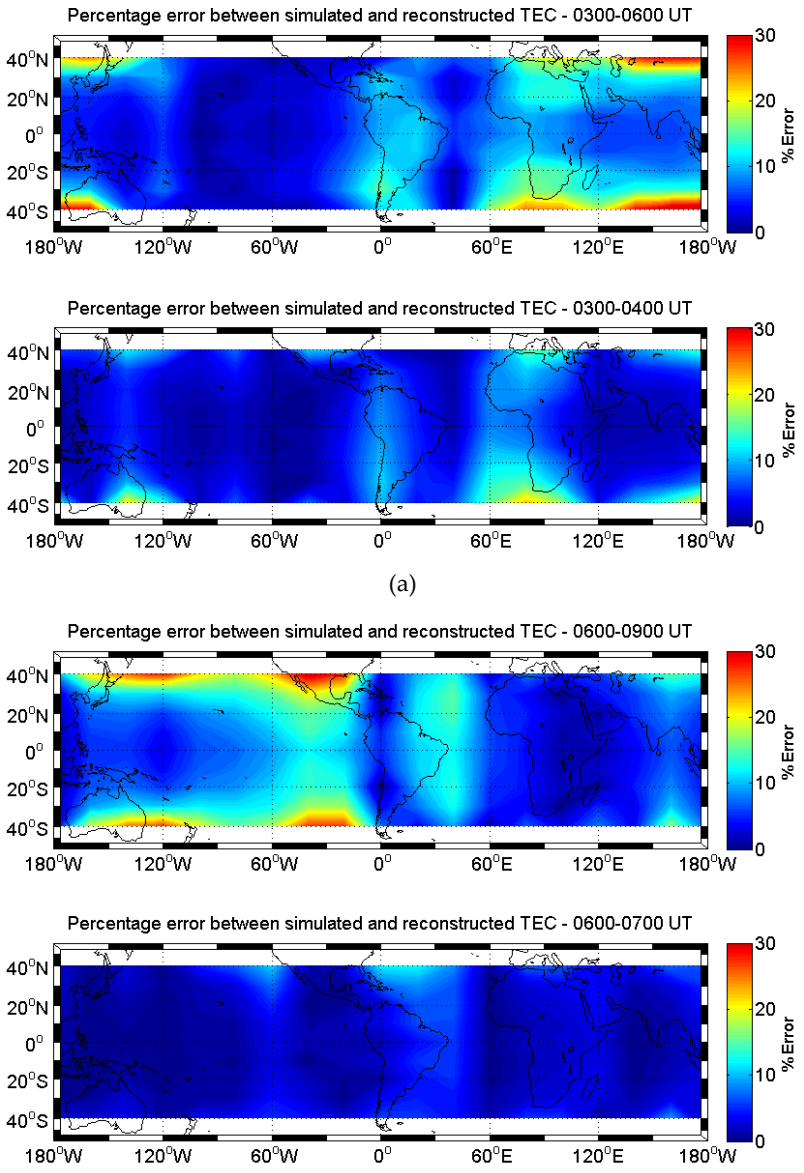

(a)

(b)

Figure 6.4. Comparison of the percentage error between the simulation and reconstruction for 3-hour and 1-hour mean TEC at two instances on 22 May 2009. (a) Percentage error for 0300-0600 hours UT (3-hour) and 0300-0400 hours UT (1-hour). (b) Percentage error for 0600-0900 hours UT (3-hour) and 0600-0700 hours UT (1-hour).

6.3.2 Reconstruction of the Topside Ionosphere-Plasmasphere

6.3.2.1 Method

Once the quality of the reconstruction technique was verified by simulation, the study progressed to real observations from COSMIC GPS receivers to qualitatively validate the algorithm against previous observations by [*Pedatella et al.*, 2011; *Lee et al.*, 2013] (discussed in Section 3.4.2 and 3.4.3). In contrast to the verification process (by simulation), here, the latitudinal dimension extends between ±50° to ensure the majority of the plasmasphere is considered. Measured differential phase data, sampled every 60

seconds, are processed by MIDAS together with the ray path geometries produced at each point of sampling (***b*** and ***A***, respectively). Given the results from the simulation, 3-hour time frames are used to provide a 33-hour window for the inversions. The reconstructed electron density is evaluated in terms of diurnal, seasonal and longitudinal variations, and specific features observed by the previous studies. GPS-derived TEC from Jason-1 [*Lee et al.*, 2013] (Section 3.4.3) is used as the primary source since it shows global characteristics of the plasmasphere above 1336 km. Results from COSMIC GPS TEC by [*Pedatella et al.*, 2011] (Section 3.4.2) are used as they provide observations of the underlying topside ionosphere, thus enabling the validation of MIDAS for both regions.

6.3.2.2 Results

Seasonal and Local Time Variations

Seasonal variations are observed by evaluating TEC during the solstices and equinoxes of the year. The distribution over ±2 weeks around the solstice (or equinox) is studied to identify seasonal evolution of the topside ionospheric-plasmaspheric TEC. General trends over the year are observed by imaging the annual TEC distribution. Variations in local time (LT) are analysed by sorting the data into 1-hour bins. Daytime is defined from dawn to dusk (0600-1800 LT), while dusk to dawn (1800-0600 LT) is considered as the night-time.

Figure 6.5 shows the mean TEC distribution during the solstice and equinox seasons, and their variation with local time. The annual trend for 2009 is shown in Figure 6.6. TEC in the topside ionosphere-plasmasphere rises during daytime to a peak in the afternoon (1200-1800 hours LT), and falls during the night with an average day-night TEC difference of 1-2 TECU. June is noted to have the lowest TEC across the globe, and December the highest. The semi-annual anomaly, prevalent in the ionosphere, is nearly non-existent in the upper regions, having only an approximately 7% difference between equinox and solstice TEC. These features from MIDAS-based COSMIC TEC reconstructions agree well with characteristics observed by [*Lee et al.*, 2013] using Jason-1 TEC, although higher TEC is seen with the COSMIC data. *Lee et al.* [2013] reported an approximate 1 TECU diurnal difference and an absence of the semi-annual anomaly. The small differences observed between results presented here from COSMIC and those from Jason-1 may be attributed to the contribution from the topside ionosphere, which is not present in Jason-1 measurements due to its higher orbit altitude of ~1336 km.

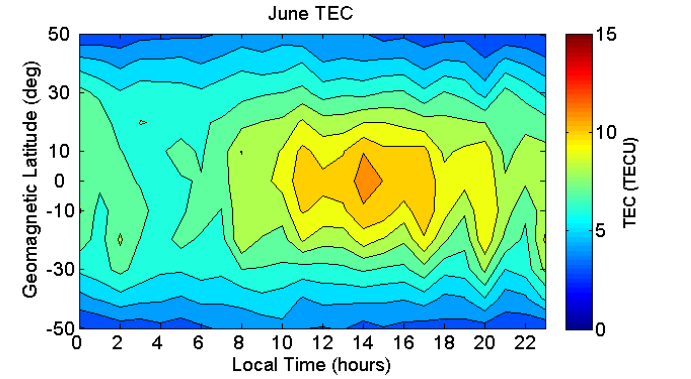

(a)

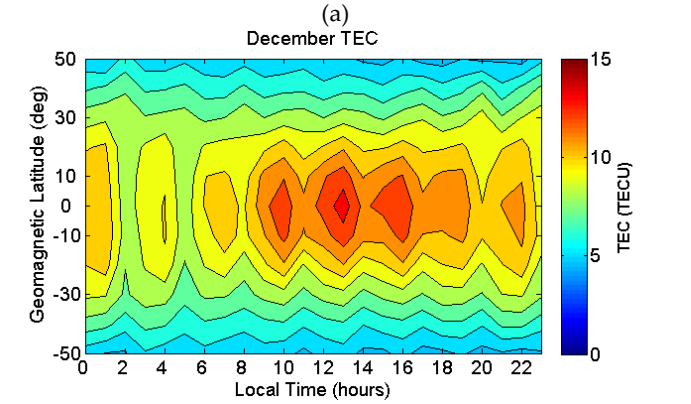

(b)

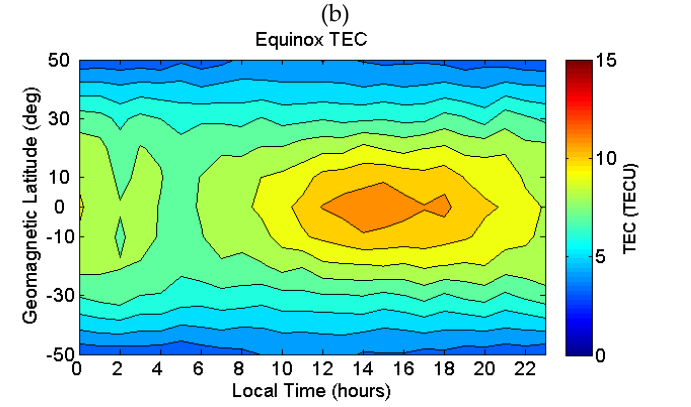

(c)

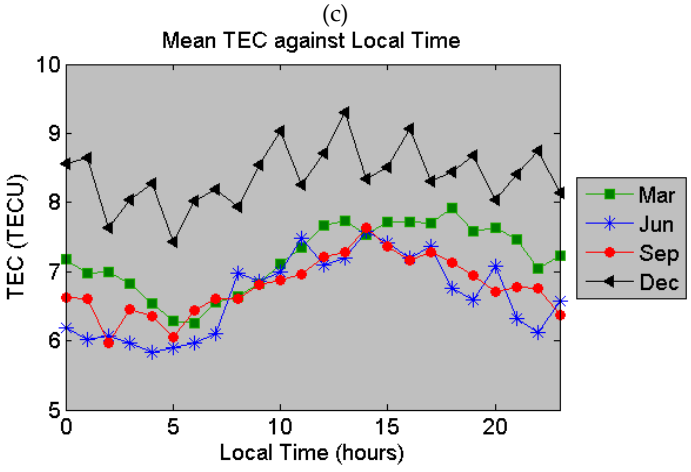

(d)

Figure 6.5. Seasonal TEC maps showing variation with local time. (a) TEC distribution for June. (b) TEC distribution for December. (c) Mean TEC distribution for March and September equinoxes. (d) Average TEC for each solstice and equinox season against local time. The TEC maps of (a)-(c) are plotted against the geomagnetic latitude.

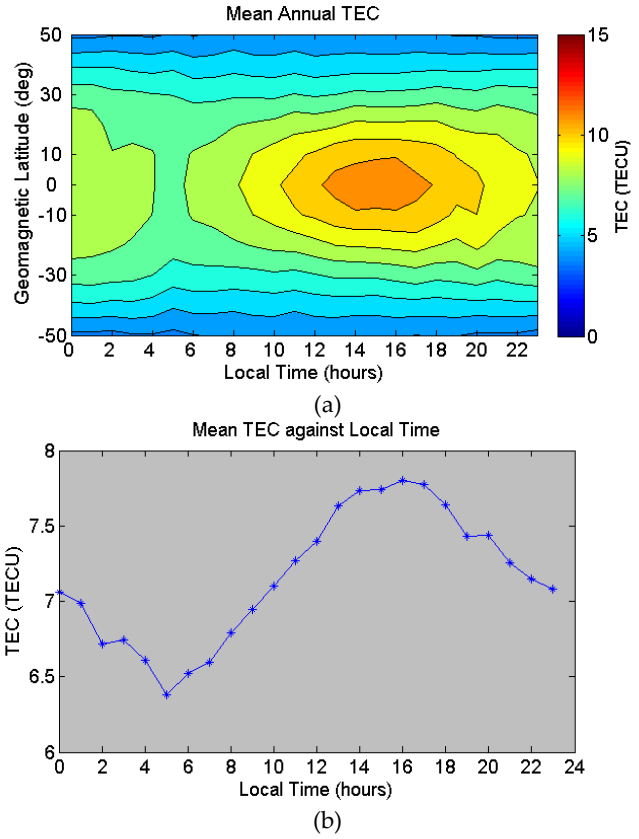

Figure 6.6. Average TEC distribution over the year 2009. (a) Variation of TEC with geomagnetic latitude and local time. (b) Average TEC against local time.

Longitudinal and L-Shell Variations

Longitudinal and L-shell variations are studied in terms of seasonal and diurnal TEC distributions in the equatorial plasmasphere (±20° geomagnetic latitude). Day and night are defined as 1000-1600 LT and 2200-0400 LT, respectively, while variations with altitude are characterised in terms of small (L<2.5) and large (L>2.5) L-shells.

MIDAS reconstructions of the plasmasphere show the presence of the annual anomaly in the American sector (30°W to 60°E geomagnetic longitudes) – a feature identified in a number of past studies (e.g. [*Clilverd et al.*, 1991; *Guiter et al.*, 1995; *Richards et al.*, 2000]) and observed by both COSMIC [*Pedatella et al.*, 2011] and Jason-1 [*Lee et al.*, 2013] GPS TEC (Sections 3.4.2 and 3.4.3). The average annual TEC distribution for 2009, given in Figure 6.7, shows a maximum in December and a minimum in June over American longitudes. The results, imaged for ±20° geomagnetic latitude between 1200 and 1800 LT, agree well with the analysis carried out by [*Pedatella et al.*, 2011] for the previous year (2008) also using COSMIC data; although the absolute TEC from MIDAS is 2-4 TECU higher for 2009, particularly during the December maximum. The ratio of December TEC to June TEC is found to be between 1 and 3, which also conforms to previous findings.

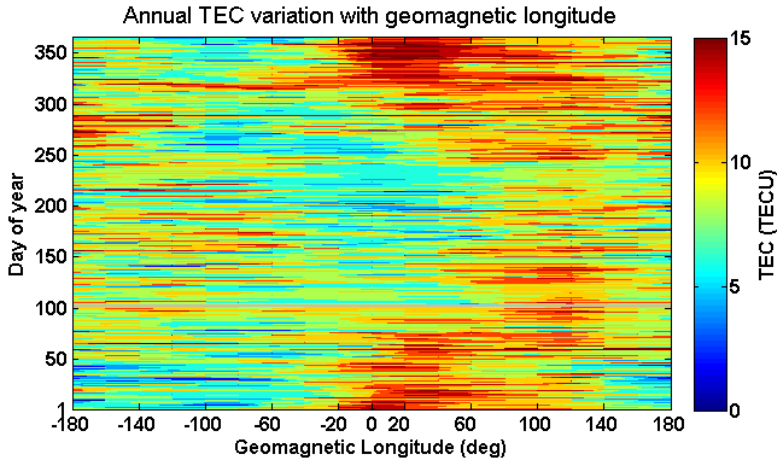

Figure 6.7. Variation in annual TEC with longitude for the year 2009. The results are comparable to the seasonal longitudinal variations for 2008 produced by [*Pedatella et al.*, 2011], shown in Figure 3.7

Figure 6.8 shows the distribution of TEC with the L-shell parameter. The annual anomaly is consistently present regardless of the altitude, as is the ratio between December TEC and June TEC. Additionally, for small L-shells, a peak is seen in June at 120°W geomagnetic longitude, while December holds the lowest TEC (i.e. reversed from the annual anomaly). This is notably absent at L>2.5. The result was also observed by [*Lee et al.*, 2013] using Jason-1 data.

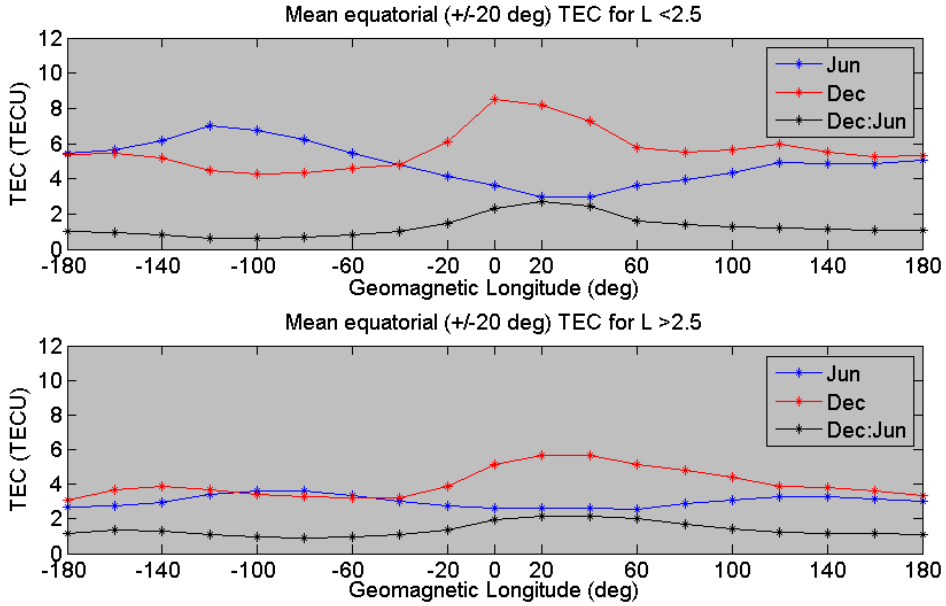

(a)

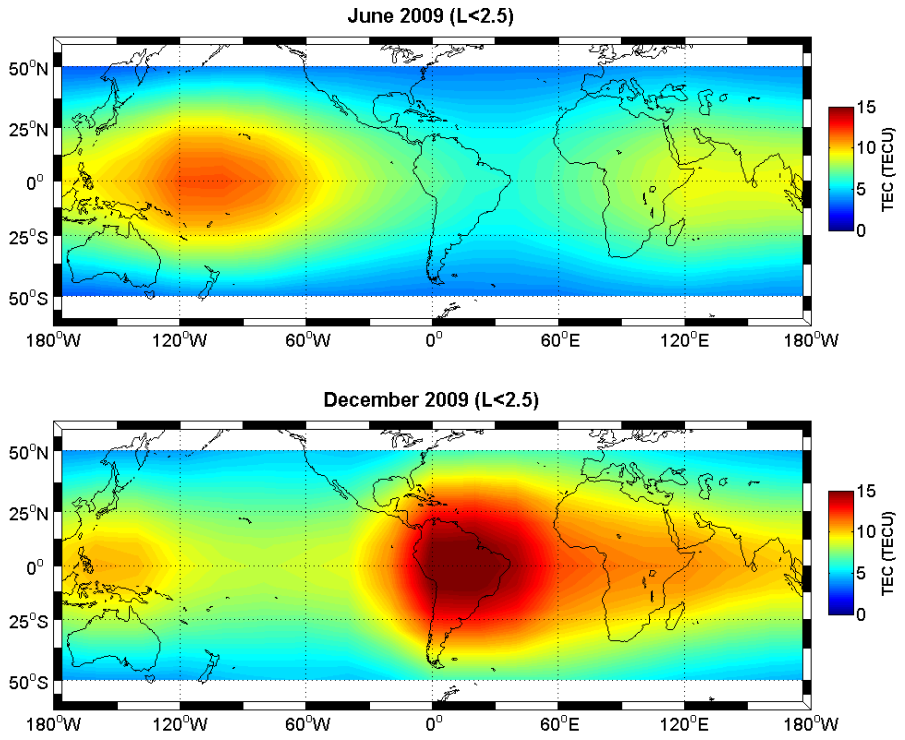

(b)

Figure 6.8. Longitudinal and L-shell variations in TEC for June and December. (a) Average TEC over equatorial magnetic latitudes (±20°) against geomagnetic longitudes for L<2.5 and L>2.5. (b) Global TEC maps of June and December for L<2.5 to highlight the peak in TEC at ~120°W in June, which is absent in December.

Diurnal variations with longitude for different seasons are given in Figure 6.9. Both the annual anomaly in the American sector and reversal of this feature (i.e. June > December) at ~120°W geomagnetic longitude seen by [*Pedatella et al.*, 2011; *Lee et al.*, 2013] can be clearly observed regardless of the time of day. Corroborating with results by [*Lee et al.*, 2013], the December to June TEC ratio over American longitudes is greater during the night relative to daytime. However, the night-time difference between December and June TEC is higher for COSMIC data, with a maximum of 6-7 TECU, compared to 3-4 TECU observed by Jason-1. This is due to the contribution from the topside ionosphere, which is strongly coupled to the higher density lower altitude ionosphere.

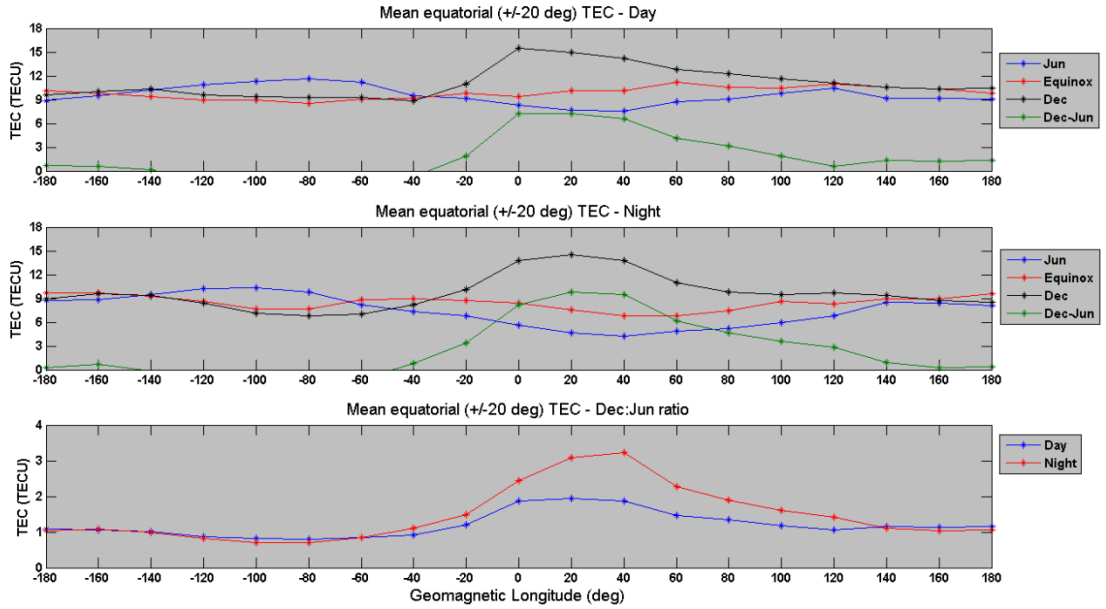

Figure 6.9. Diurnal and seasonal variations in TEC with longitude. First two panels show the average TEC distribution during day and night for the solstices and equinox. The December to June ratio is also given which shows the annual anomaly over American longitudes. Last panel compares the December to June ratio between day and night.

6.4 Discussion

Reconstructions of the quiet-time topside ionosphere-plasmasphere by MIDAS show strong agreement with characteristics and features seen in previous studies presented in Chapter 3, excluding hemispheric variations. Notwithstanding the enforced hemispherical symmetry of the TEC distribution (due to Euler potentials representing a dipole geomagnetic field), comparison of results with Jason-1 ([*Lee et al.*, 2013]) and COSMIC [*Pedatella et al.*, 2011] GPS TEC has enabled the algorithm to be validated for the region. However, notable differences can be seen in the absolute TEC, particularly against Jason-1 data, which may be attributed to several factors. The orbital altitude of Jason-1 is ~1336 km, which effectively isolates the plasmasphere. COSMIC satellites are at an altitude of 750-850 km and thus include the higher density topside ionosphere. Since the physics of the topside ionosphere is influenced by both the lower ionosphere and the plasmasphere, the added variation in TEC may also account for the deviations observed between [*Lee et al.*, 2013]'s results and MIDAS reconstructions. Differences in data processing also have an effect on the final analysis. *Lee et al.*, [2013] used averaged data over a period of 8 years (2002-2009), thus observing the plasmasphere over

decreasing solar activity during solar cycle 23. The majority of data was collected from 2003-2006, enabling the study to be performed during moderate solar activity. Furthermore, as discussed in Chapter 3, the analysis with Jason-1 TEC by *Lee et al.*, [2013] was done by classifying the data into low and high solar (F10.7 < 100 and F10.7 > 100, respectively) and geomagnetic (Kp < 2.5 and Kp > 2.5, respectively) activity. In contrast, the validation of MIDAS was carried out using COSMIC data for the year 2009 only – i.e. during the solar minimum of cycle 24 – for which no solar/geomagnetic classification of data was applied.

The rationale for the differences between *Lee et al.*, [2013] and MIDAS results are further supported by *Pedatella et al.*, [2011]. The absolute TEC derived from the 2008 COSMIC data in the study is comparable to the MIDAS reconstructions of the topside ionosphere-plasmasphere using the same data source. The differences observed here can be attributed to two factors. Validation of MIDAS was performed using 2009 COSMIC data, and thus contained inherent variations in data coverage and the region's dynamics relative to the previous year. Secondly, the spatial, temporal and data resolutions are different in the two studies. The MIDAS algorithm discussed here uses considerably large spatial voxels where the electron density is assumed constant, to compromise on computational resources. The data is also averaged over 3-hours per inversion, providing a smaller data resolution and binning, which has a significant effect on the images as highlighted by the 3-hour and 1-hour reconstructions of the Gallagher model simulation.

6.5 Summary and Conclusion

The work presented in this chapter validated MIDAS – a toolkit of algorithms for ionospheric tomography and data assimilation – for quiet-time topside ionospheric-plasmaspheric imaging using LEO GPS TEC. The COSMIC constellation during the year 2009 (solar minimum), orbiting at an altitude of 750-850 km, was used as the data source. Extension of MIDAS was achieved by incorporating the geomagnetic field's influence on electron density distribution (in the topside ionosphere-plasmasphere) by means of Euler potentials. The validation process was performed in two stages. A simulation of the empirical model by [*Gallagher et al.*, 1988] was first sampled from COSMIC GPS receiver

positions and inverted by MIDAS to verify the quality of reconstruction. The verification process was also used to identify the optimal time resolution, found to be averaged 3-hour data, given the limited coverage of COSMIC for continuous global imaging. The algorithm was then successfully validated by reconstructing the (quiet) topside ionosphere-plasmasphere for the year 2009, using COSMIC satellites' GPS POD observations and comparing the results with previous independent studies on global plasmaspheric TEC ([*Pedatella et al.*, 2011; *Lee et al.*, 2013]).

While the validation of MIDAS was successful for the quiet topside ionosphere-plasmasphere, some limitations still need to be addressed. The algorithm's application of Euler potentials of a dipole to represent the geomagnetic field leads to an enforced hemispherical symmetry, resulting in the masking of any hemispherical variations. This may be resolved by incorporating a more realistic geomagnetic field as a priori knowledge into the algorithm. Furthermore, the current time resolution of 3-hour averaged data (frames) is not sufficient to image the storm- or active-time topside ionosphere-plasmasphere due to the presence of more dynamic structures. Increasing this resolution, however, requires better ray path coverage of the region to maintain the quality of reconstructions, which may be achieved in the future through an improved network of LEO GPS receivers such as TOPCAT, discussed in the previous chapter.

7 Conclusions & Future Work

This thesis explored the implementation of GPS-based ionospheric tomography to image the electron content of the topside ionosphere and plasmasphere. The use of ground and Low Earth Orbit (LEO) radio occultation receivers has already been well-established for imaging the ionosphere. Extending similar techniques for regions beyond, however, is a new concept that has only been addressed in recent years. The research presented here was conducted in two parts: first, the use of new, low-cost technology for placing GPS receivers in a suitable LEO configuration was demonstrated. This was followed by the establishment of inversion algorithms that could process the new dataset when it is generated. Thus, the thesis effectively addressed the realisation of the complete imaging system – from instrumentation (for data collection), to tomography algorithms that can reconstruct images of the topside ionosphere-plasmasphere. This chapter summarises the work carried out to achieve the objectives of the research, results produced and future work that may be undertaken which can further advance imaging capabilities for the topside ionosphere and plasmasphere.

With the bulk of the ionised plasma contained in the ionosphere, the topside ionosphere and plasmasphere have always garnered relatively less interest in the ionospheric community, particularly concerning effects on radio signals, such as GPS. The majority of studies to investigate the electron content of the Earth's ionised atmosphere have been focused on the ionosphere, with contributions from higher altitudes typically being either included in the ionospheric measurements or considered negligible depending on the circumstances. Recent observations, as discussed in Chapter 3, however, have shown that the strong coupling between the ionosphere, topside and plasmasphere results in significant co-dependence in the electron distributions of the regions. Understanding the dynamics of the ionised atmosphere thus requires the availability of reliable measurements of the tenuous topside ionosphere and plasmasphere, as well as of the main ionosphere.

One method of measuring the electron content in the Earth's ionised atmosphere is through ionospheric tomography, which is discussed in Chapter 4. In general, this

requires a dual-frequency radio system whose signals propagate through the region(s) of interest. The received signals are used to extract the total electron content (TEC) along the signal path, which can then be inverted by applying tomographic techniques to image the electron distribution of the region. Since GPS is inherently a multi-frequency broadcasting system that is readily available with continuous global coverage, it provides a convenient means with which ionospheric tomography can be implemented. Certainly to date, large networks of ground receivers as well as space-based radio occultation receivers have provided much needed data sets that have contributed a wealth of knowledge to ionospheric science.

In addition to the study of the ionosphere, GPS provides a further advantage that has only been exploited in recent years. Placed at an altitude of 20,200 km, GPS satellites orbit at the boundary of the (dayside) plasmasphere. Since the broadcast signals propagate earthward from this altitude, GPS is also capable of imaging the topside ionosphere and plasmasphere; thereby enabling observations of electron distribution of the entire terrestrial ionised atmosphere. Given that many satellites now carry a dual-frequency GPS receiver for precise orbit determination (POD), those launched into Low Earth Orbit (LEO) – e.g. CHAMP, COSMIC, Jason-1 – provide an ideal data source from which to derive TEC of the topside ionosphere-plasmasphere. However, these missions (with the exception of COSMIC) have all consisted of only single satellites, which cannot provide global coverage. Furthermore, the TEC derived from their POD observations are secondary data. Thus, whilst they provide useful information, the satellites are not configured to observe the topside ionosphere-plasmasphere, and any imaging must be performed within the limitations imposed by the satellites' primary missions.

To address these problems, the first phase of the research in this thesis proposed the installation of dual-frequency GPS receivers at LEO altitudes for dedicated imaging of the topside ionosphere and plasmasphere. The novelty of this idea was that it was to be developed using simple, commercial-off-the-shelf (COTS) components, thus greatly reducing development costs of the instrument. Further, the receiver was to be placed on-board a CubeSat – a nano-satellite measuring approximately 100 x 100 x 300 mm. The miniature satellites have the advantage of being able to 'piggy-back' on launches of large satellites, thus drastically reducing their launch costs. This was of particular importance, as high resolution global coverage of the topside ionosphere-plasmasphere would

require a constellation of such CubeSats – a possible next phase that may be implemented in the future. Since the low-cost technology has not been applied before, a technology demonstrator was required to provide proof of concept. Chapter 5 discussed the development life-cycle of this instrument, 'TOPCAT', which was launched as a payload on UK Space Agency's pilot CubeSat, UKube-1. TOPCAT consisted of a commercial Novatel receiver, along with controller electronics designed from COTS components. Chapter 5 included the design challenges that were encountered due to constraints and specifications imposed by CubeSat technology, as well as the series of qualification tests (vibration, thermal-vacuum and radiation) required to qualify the payload as space-worthy. UKube-1 was successfully launched on 8 July 2014 into a sun-synchronous, near-circular polar orbit at an altitude of 630 km. It is currently in its commissioning phase.

The second phase of this thesis, as mentioned before, is the validation of an inversion algorithm capable of processing GPS TEC to produce images of the topside ionosphere-plasmasphere. In Chapter 4, a suite of algorithms, 'MIDAS', was introduced, that was developed by the University of Bath for ionospheric tomography. Whilst capable of assimilating data from multiple instruments, it is primarily used with differential GPS phase data to reconstruct the electron concentration of the ionosphere. Chapter 6 discussed the adaptation of this set of algorithms for the topside ionosphere and plasmasphere, and validated the modified version of MIDAS for the region. The validation process was carried out in two stages: first, a simulation described by Gallagher et al. [1988] was reconstructed to verify the quality of the images. This was followed by reconstructing the plasmasphere using COSMIC GPS POD phase data for the year 2009. With six satellites in the COSMIC constellation, the data set provided near-global coverage to image the topside ionosphere-plasmasphere in its entirety. The validation was completed by qualitatively comparing the reconstructed images with previous observations obtained through COSMIC and Jason-1 missions. Results showed that MIDAS can successfully reconstruct the undisturbed (quiet-time) topside ionosphere-plasmasphere using COSMIC data. However, imaging the storm-time topside ionosphere-plasmasphere requires better data coverage (i.e. more receivers) as the resolution offered by the COSMIC constellation is not sufficient to reconstruct fast-evolving structures.

In addition to the promising results, of importance to note is that the research undertaken also emphasised the need for future work if a system is to be established for continuous global imaging of the topside ionosphere and plasmasphere. As mentioned previously, high resolution imaging of regions beyond the ionosphere in both quiet and disturbed conditions require more receivers in LEO altitudes. With the feasibility of CubeSat technology for imaging proven through the successful launch of TOPCAT, a potential next phase is the launch of a constellation of CubeSats, each carrying a dual-frequency GPS receiver dedicated for topside ionosphere-plasmasphere imaging. This would require careful design of a constellation, which provides an ideal number of satellites that compromises between the best possible coverage and costs incurred in developing multiple satellites. Indeed, given that many present and future missions now carry GPS receivers for orbit determination, these may also be exploited to further augment the new dataset enabled by the constellation. Further, other GNSS constellations such as GLONASS, Galileo and Compass may also be used by installing multi-frequency LEO receivers that can process other GNSS signals – effectively providing a LEO-based GNSS receiver network for imaging the topside ionosphere-plasmasphere, much akin to the IGS ground network available for ionospheric science.

With the availability of better data coverage, the next step is to improve the reconstruction algorithm currently used to image the electron content of the topside and plasmasphere. At present, the limited dataset available from the six COSMIC satellites poses a severely underconstrained problem that needs to be inverted (through tomography) to reconstruct the regions. MIDAS addresses this by including a priori knowledge of the topside ionosphere-plasmasphere to constrain the solution. In particular, the electron distribution is confined to geomagnetic field lines, described through Euler potentials of a dipole field structure. The limitation of this method is that the electron distribution is restricted to a model that does not completely represent the true geomagnetic field; giving rise to artefacts such as hemispherical symmetry about the geomagnetic equator. With the availability of new data, however, such constraints can be relaxed as better data coverage enables a more realistic reconstruction of the region, thus enabling a complete system that can continuously measure the upper reaches of the Earth's ionised atmosphere.

In conclusion, the research presented in this thesis demonstrates that ionospheric tomography can be successfully applied for imaging the global topside ionosphere and plasmasphere, provided an adequate number of LEO receivers are present to generate sufficient data for the inversions. Current datasets for *global* imaging can only be obtained from the COSMIC constellation, which is composed of six satellites. While the data resolution from these receivers can faithfully reconstruct the quiet-time topside ionosphere and plasmasphere, more receivers are needed to extend the algorithm to accurately image when the region is more structured (e.g. during storms). This may be addressed by installing commercial dual- or multi-frequency GNSS receivers in LEO altitudes by means of CubeSats, effectively supporting current LEO receivers already in orbit. As demonstrated in this thesis, this is a viable means of providing a much needed data source for the region that can also be realised in a short timescale and at a significantly low cost; which may otherwise not be possible with conventional technology used for space-borne instruments.

References

AMSAT-UK (2014), UKube-1 Launch Information | AMSAT-UK on WordPress.com, Available from: http://amsat-uk.org/2014/07/03/ukube-1-launch-information/ (Accessed 1 August 2014)

Anthes, R. A. (2011), Exploring Earth's atmosphere with radio occultation: contributions to weather, climate and space weather, *Atmos. Meas. Tech.*, *4*(6), 1077–1103.

Austen, J. R., S. J. Franke, and C. H. Liu (1988), Ionospheric imaging using computerized tomography, *Radio Sci.*, *23*(3), 299–307, doi:10.1029/RS023i003p00299.

Bauer, S. (1969), Diffusive equilibrium in the topside ionosphere, *Proc. IEEE*, *57*(6), 1114–1118.

Bauer, S. J. (1962a), On the Structure of the Topside Ionosphere, *J. Atmos. Sci.*, *16*, 276–278.

Bauer, S. J. (1962b), The Electron Density Distribution above the F2 Peak and Associated Atmospheric Parameters, *J. Atmos. Sci.*, *19*(1), 17–19, doi:10.1175/1520-0469(1962)019<0017:TEDDAT>2.0.CO;2.

Baumjohann, W., and R. A. Treumann (1997), *Basic space plasma physics*, Imperial College Press.

Bhavnani, K. H., and R. P. Vancour (1991), *Coordinate Systems for Space and Geophysical Applications*, Phillips Laboratory, US Air Force Systems Command.

Brice, N. M. (1967), Bulk motion of the magnetosphere, *J. Geophys. Res.*, *72*(21), 5193–5211.

Bust, G. S., and C. N. Mitchell (2008), History, current state, and future directions of ionospheric imaging, *Rev. Geophys.*, *46*(1).

Carpenter, D. L. (1966), Whistler studies of the plasmapause in the magnetosphere: 1. Temporal variations in the position of the knee and some evidence on plasma motions near the knee, *J. Geophys. Res.*, *71*(3), 693–709, doi:10.1029/JZ071i003p00693.

Carpenter, D. L., and R. R. Anderson (1992), An ISEE/whistler model of equatorial electron density in the magnetosphere, *J. Geophys. Res.*, *97*(A2), 1097, doi:10.1029/91JA01548.

Carpenter, D. L., and C. G. Park (1973), What ionospheric workers should know about the plasmapause--plasmasphere., *Rev. Geophys. Sp. Phys. 11 No. 1, 133-154(Feb 1973).*

Carpenter, D. L., C. G. Park, H. A. Taylor, and H. C. Brinton (1969), Multi-experiment detection of the plasmapause from EOGO satellites and Antarctic ground stations, *J. Geophys. Res.*, *74*(7), 1837–1847, doi:10.1029/JA074i007p01837.

Chartier, A. T., N. D. Smith, C. N. Mitchell, D. R. Jackson, and P. J. C. Patilongo (2012), The use of ionosondes in GPS ionospheric tomography at low latitudes, *J. Geophys. Res. Sp. Phys.*, *117*(A10).

Clilverd, M. A., A. J. Smith, and N. R. Thomson (1991), The annual variation in quiet time plasmaspheric electron density, determined from whistler mode group delays, *Planet. Space Sci.*, *39*(7), 1059–1067, doi:10.1016/0032-0633(91)90113-O.

COMET, UCAR, and N. H. A. Observatory (2004a), Magnetic Convection, Available from: http://www.meted.ucar.edu/hao/aurora/txt/x_m_2_2.php (Accessed 19 December 2014)

COMET, UCAR, and N. H. A. Observatory (2004b), Magnetosphere-Ionosphere Current System, Available from: http://www.meted.ucar.edu/hao/aurora/txt/x_m_3_1.php (Accessed 30 January 2013)

Darrouzet, F., J. De Keyser, and V. Pierrard (2009), *The Earth's Plasmasphere: A CLUSTER and IMAGE Perspective*, Springer.

Dtrx (2009), TomographyPrinciple_Illustration, *de.wikipedia*. Available from: http://upload.wikimedia.org/wikipedia/commons/2/25/TomographyPrinciple_Illustration.png (Accessed 16 February 2015)

ESA (n.d.), CHAMP - eoPortal Directory - Satellite Missions - Earthnet Online, Available from: https://directory.eoportal.org/web/eoportal/satellite-missions/c-missions/champ (Accessed 28 February 2013)

Foster, J. C., P. . Erickson, J. Goldstein, and F. J. Rich (2002), Ionospheric signatures of plasmaspheric tails, *Geophys. Res. Lett.*, *29*(13), 1623, doi:10.1029/2002GL015067.

Foster, J. C., A. J. Coster, P. J. Erickson, F. J. Rich, and B. R. Sandel (2004), Stormtime observations of the flux of plasmaspheric ions to the dayside cusp/magnetopause, *Geophys. Res. Lett.*, *31*(8).

Gallagher, D. L. (2005a), The Earth's Plasmasphere, *NASA*. Available from: http://plasmasphere.nasa.gov/ (Accessed 26 January 2012)

Gallagher, D. L. (2005b), The Earth's Plasmasphere (Regions), *NASA*. Available from: http://plasmasphere.nasa.gov/regions.html (Accessed 17 February 2012)

Gallagher, D. L., P. D. Craven, and R. H. Comfort (1988), An empirical model of the earth's plasmasphere, *Adv. Sp. Res.*, *8*(8), 15–24, doi:10.1016/0273-1177(88)90258-X.

Ganguli, G., M. . Reynolds, and M. . Liemohn (2000), The plasmasphere and advances in plasmaspheric research, *J. Atmos. Solar-Terrestrial Phys.*, *62*(17-18), 1647–1657, doi:10.1016/S1364-6826(00)00117-6.

Ganushkina, N. Y., I. Dandouras, Y. Y. Shprits, and J. Cao (2011), Locations of boundaries of outer and inner radiation belts as observed by Cluster and Double Star, *J. Geophys. Res.*, *116*(A9), A09234, doi:10.1029/2010JA016376.

Goldstein, J., B. R. Sandel, W. T. Forrester, M. F. Thomsen, and M. R. Hairston (2005), Global plasmasphere evolution 22–23 April 2001, *J. Geophys. Res. Sp. Phys.*, *110*(A12).

Grebowsky, J. M., N. K. Rahman, and H. A. Taylor (1970), Comparison of coincident OGO 3 and OGO 4 hydrogen ion composition measurements, *Planet. Space Sci.*, *18*(7), 965–976, doi:10.1016/0032-0633(70)90100-5.

Greenland, S., and C. Warren (2011), *UKube Payload Interface Protocol*.

Gringauz, K. I. (1985), Structure and Properties of the Earth's Plasmasphere, *Adv. Sp. Res.*, *5*(4), 391–400.

Gringauz, K. I., and V. V. Bezrukikh (1976), Asymmetry of the Earth's plasmasphere in the direction noon-midnight from Prognoz and Prognoz-2 data, *J. Atmos. Terr. Phys.*, *38*(11), 1071–1076, doi:10.1016/0021-9169(76)90036-2.

Guiter, S. M., C. E. Rasmussen, T. I. Gombosi, J. J. Sojka, and R. W. Schunk (1995), What is the source of observed annual variations in plasmaspheric density?, *J. Geophys. Res.*, *100*(A5), 8013, doi:10.1029/94JA02866.

Hajj, G. A., R. Ibañez-Meier, E. R. Kursinski, and L. J. Romans (1994), Imaging the ionosphere with the global positioning system, *Int. J. Imaging Syst. Technol.*, *5*(2), 174–187, doi:10.1002/ima.1850050214.

Hargreaves, J. K. (1979), *The upper atmosphere and solar-terrestrial relations-An introduction to the aerospace environment*, Van Nostrand Reinhold Co., New York, USA

Hargreaves, J. K. (1992), *The Solar-Terrestrial Environment*, Cambridge Atmospheric and Space Science Series, Cambridge, UK.

Hartman, W. A., and R. A. Heelis (2007), Longitudinal variations in the equatorial vertical drift in the topside ionosphere, *J. Geophys. Res. Sp. Phys.*, *112*(A3).

Heelis, R. A., W. R. Coley, A. G. Burrell, M. R. Hairston, G. D. Earle, M. D. Perdue, R. A. Power, L. L. Harmon, B. J. Holt, and C. R. Lippincott (2009), Behavior of the O+/H+ transition height during the extreme solar minimum of 2008, *Geophys. Res. Lett.*, *36*(18).

Heise, S., N. Jakowski, A. Wehrenpfennig, C. Reigber, and H. Luhr (2002), Sounding of the topside ionosphere/plasmasphere based on GPS measurements from CHAMP: Initial results, *Geophys. Res. Lett.*, *29*(14), 1699, doi:10.1029/2002GL014738.

Hofmann-Wellenhof, B., H. Lichtenegger, and J. Collins (1993), *Global Positioning System. Theory and practice.*

Huang, C., F. J. Rich, O. de La Beaujardiere, and R. A. Heelis (2010), Longitudinal and seasonal variations of the equatorial ionospheric ion density and eastward drift velocity in the dusk sector, *J. Geophys. Res. Sp. Phys.*, *115*(A2).

Hunsucker, R. H., and J. K. Hargreaves (2003), *The High-Latitude Ionosphere and its Effects on Radio Propagation*, Cambridge University Press.

Iijima, T., and T. A. Potemra (1976), Field-Aligned Currents in the Dayside Cusp Observed by Triad, *J. Geophys. Res.*, *81*(34), 5971–5979.

Ilie, R. (2007), Inner Magnetosphere : Plasma Sheet and Ring Current, Available from: www-ssc.igpp.ucla.edu/gem/tutorial/2007/2007-RI-inmag2.pdf (Accessed 25 January 2013)

Kaplan, E. D., and C. J. Hegarty (2006), *Understanding GPS: Principles and Applications*, Second Edi., Artech House.

Kotova, G. A. (2007), The Earth's plasmasphere: State of studies (a Review), *Geomagn. Aeron.*, *47*(4), 409–422, doi:10.1134/S0016793207040019.

Kotova, G. A., V. V. Bezrukikh, M. I. Verigin, L. A. Lezhen, and N. A. Barabanov (2002), Interball 1/alpha 3 cold plasma measurements in the evening plasmasphere: Quite and disturbed magnetic conditions, *Adv. Sp. Res.*, *30*(10), 2313–2318, doi:10.1016/S0273-1177(02)80256-3.

Leblanc, F., K. Aplin, Y. Yair, G. Harrison, J. P. Lebreton, and M. Blanc (Eds.) (2008), *Planetary atmospheric electricity*, Springer Science & Business Media.

Lee, H.-B., G. Jee, Y. H. Kim, and J. S. Shim (2013), Characteristics of global plasmaspheric TEC in comparison with the ionosphere simultaneously observed by Jason-1 satellite, *J. Geophys. Res. Sp. Phys.*, *118*(2), 935–946, doi:10.1002/jgra.50130.

Leitinger, R. (1996), Tomography, in *Modern Ionospheric Science*, edited by H. Kohl, R. Ruster, and K. Schlegel, pp. 346–350, European Geophysical Society.

Lemaire, J. F., and K. I. Gringauz (1998), *The Earth's Plasmasphere*, Cambridge University Press, Cambridge, UK.

Marubashi, K. (1970), Structure of topside ionosphere in high latitudes(Topside ionosphere structure in high latitudes, discussing electron density profile, corpuscular radiation ionizing effects, polar peak and trough), *RADIO Res. Lab. J.*, *17*, 335–416.

Masson, A., O. Santolík, D. L. Carpenter, F. Darrouzet, P. M. E. Décréau, F. E.-L. Mazouz, J. L. Green, S. Grimald, M. B. Moldwin, and F. Němec (2009), Advances in plasmaspheric wave research with CLUSTER and IMAGE observations, in *The Earth's Plasmasphere*, edited by F. Darrouzet, J. De Keyser, and V. Pierrard, pp. 137–191, Springer.

McIlwain, C. E. (1961), Coordinates for mapping the distribution of magnetically trapped particles, *J. Geophys. Res.*, *66*(11), 3681, doi:10.1029/JZ066i011p03681.

Mitchell, C. N., and P. Spencer (2002), Development of tomographic techniques for large scale ionospheric imaging, in *Proc of Ionospheric Effects Symposium. Alexandria, VA, pp. 6A1-1–6A1-8*.

Mitchell, C. N., and P. S. J. Spencer (2003), A three-dimensional time-dependent algorithm for ionospheric imaging using GPS, *Ann. Geophys.*, *46*(4), 687–696, doi:10.4401/ag-4373.

Mitchell, C. N., P. S. Cannon, and P. S. J. Spencer (2002), *Multi-Instrument Data Analysis System (MIDAS) Imaging of the Ionosphere*, DTIC Document.

NASA (2013), SOHO LASCO C3 Latest Image, Available from: http://soho.nascom.nasa.gov/data/realtime/c3/512/ (Accessed 21 January 2013)

National Academy of Sciences (2003), *The Sun to the Earth -- and Beyond: A decadal Research Strategy in Solar and Space Physics*, National Academies Press, Washington, D. C.

Park, C. G. (1974), Some features of plasma distribution in the plasmasphere deduced from Antarctic whistlers, *J. Geophys. Res.*, *79*(1), 169–173.

Park, C. G., D. L. Carpenter, and D. B. Wiggin (1978), Electron density in the plasmasphere: Whistler data on solar cycle, annual, and diurnal variations, *J. Geophys. Res.*, *83*(A7), 3137, doi:10.1029/JA083iA07p03137.

Pedatella, N. M., and K. M. Larson (2010), Routine determination of the plasmapause based on COSMIC GPS total electron content observations of the midlatitude trough, *J. Geophys. Res.*, *115*(A9), A09301, doi:10.1029/2010JA015265.

Pedatella, N. M., J. M. Forbes, A. Maute, A. D. Richmond, T.-W. Fang, K. M. Larson, and G. Millward (2011), Longitudinal variations in the F region ionosphere and the topside ionosphere-plasmasphere: Observations and model simulations, *J. Geophys. Res.*, *116*(A12), A12309, doi:10.1029/2011JA016600.

Pereyra, V. (2000), Ray tracing methods for inverse problems, *Inverse Probl.*, *16*(6), R1–R35, doi:10.1088/0266-5611/16/6/201.

Pinto Jayawardena, T., C. Mitchell, R. J. Watson, J. R. Rose, C. J. Coleman, and M. Jessop (2014), TOPCAT: A Space-Borne Dual-Frequency GPS Receiver for Topside Ionosphere and Plasmasphere Computer Assisted Tomography, in *Proceedings of the 27th International Technical Meeting of The Satellite Division of the Institute of Navigation (ION GNSS+ 2014)*, pp. 1492–1498.

Reiff, P. H. (1999), The Sun-Earth Connection, , Figure 5. [online] Available from: http://space.rice.edu/IMAGE/livefrom/sunearth.html (Accessed 21 January 2013)

Richards, P. G., and D. G. Torr (1985), Seasonal, diurnal, and solar cyclical variations of the limiting H+ flux in the Earth's topside ionosphere, *J. Geophys. Res. Sp. Phys.*, *90*(A6), 5261–5268.

Richards, P. G., T. Chang, and R. H. Comfort (2000), On the causes of the annual variation in the plasmaspheric electron density, *J. Atmos. Solar-Terrestrial Phys.*, *62*(10), 935–946, doi:10.1016/S1364-6826(00)00039-0.

Sandel, B. R., J. Goldstein, D. L. Gallagher, and M. Spasojevic (2003), Extreme Ultraviolet Imager Observations of the Structure and Dynamics of the Plasmasphere, *Space Sci. Rev.*, *109*(1-4), 25–46, doi:10.1023/B:SPAC.0000007511.47727.5b.

Sibanda, P. (2010), Challenges in topside ionospheric modelling over South Africa, Rhodes University.

Singh, N., and J. L. Horwitz (1992), Plasmasphere refilling: Recent observations and modeling, *J. Geophys. Res.*, *97*(A2), 1049, doi:10.1029/91JA02602.

Sodankyla Geophysical Observatory (2014), SGO Ionospheric Tomography Description, *Univ. Oulu*. Available from: http://www.sgo.fi/Data/Tomography/tomoDescr.php (Accessed 12 April 2015)

Southwest Research Institute (n.d.), Ring Current, Available from: http://pluto.space.swri.edu/image/glossary/ring_current.html (Accessed 12 April 2015a)

Southwest Research Institute (n.d.), The Plasmasphere, Part 2, Available from: http://pluto.space.swri.edu/IMAGE/glossary/plasmasphere2.html (Accessed 15 February 2013b)

Spencer, P. S. J., and C. N. Mitchell (2011), Imaging of 3-D plasmaspheric electron density using GPS to LEO satellite differential phase observations, *Radio Sci.*, *46*(3), doi:10.1029/2010RS004565.

SPENVIS (2013), Background: Trapped particle radiation models, Available from: http://www.spenvis.oma.be/help/background/traprad/traprad.html (Accessed 16 January 2013)

Stern, D. P. (1970), Euler potentials, *Am. J. Phys.*, *38*(4), 494–501.

Tascione T.F. (1994), *Introduction to the Space Environment*, Second Edi., Kreiger Publishing Company.

Taylor, H. A., and W. J. Walsh (1972), The light-ion trough, the main trough, and the plasmapause, *J. Geophys. Res.*, *77*(34), 6716, doi:10.1029/JA077i034p06716.

Taylor, H. A., H. C. Brinton, D. L. Carpenter, F. M. Bonner, and R. L. Heyborne (1969), Ion depletion in the high-latitude exosphere; simultaneous OGO 2 observations of

the light ion trough and the VLF cutoff, *J. Geophys. Res.*, *74*(14), 3517–3528, doi:10.1029/JA074i014p03517.

Tsui, J. B.-Y. (2000), *Fundamentals of global positioning system receivers*, Wiley-Interscience.

U.S. Naval Observatory (n.d.), Current GPS Constellation - Naval Oceanography Portal, [online] Available from: http://www.usno.navy.mil/USNO/time/gps/current-gps-constellation (Accessed 12 April 2015)

Winter, B. (2012), *TOPCAT Vibration Test Report*.

Yin, P., and C. N. Mitchell (2005), Use of radio-occultation data for ionospheric imaging during the April 2002 disturbances, *GPS Solut.*, *9*(2), 156–163.

Yin, P., and C. N. Mitchell (2014), Improving the vertical electron density profile in ionospheric imaging at storm time: A case study on 25–27 September 2011, *J. Geophys. Res. Sp. Phys.*, *119*(9), 7963–7971.

Yin, P., C. N. Mitchell, L. Alfonsi, M. Pinnock, P. Spencer, G. De Franceschi, V. Romano, P. Newell, P. Sarti, and M. Negusini (2009), Imaging of the Antarctic ionosphere: Experimental results, *J. Atmos. Solar-Terrestrial Phys.*, *71*(17), 1757–1765.

Yue, X., W. S. Schreiner, D. C. Hunt, C. Rocken, and Y.-H. Kuo (2011), Quantitative evaluation of the low Earth orbit satellite based slant total electron content determination, *Sp. Weather*, *9*(9), S09001.

Appendix 1 – TOPCAT Design Documents

A1.1 Schematic and PCB Layout

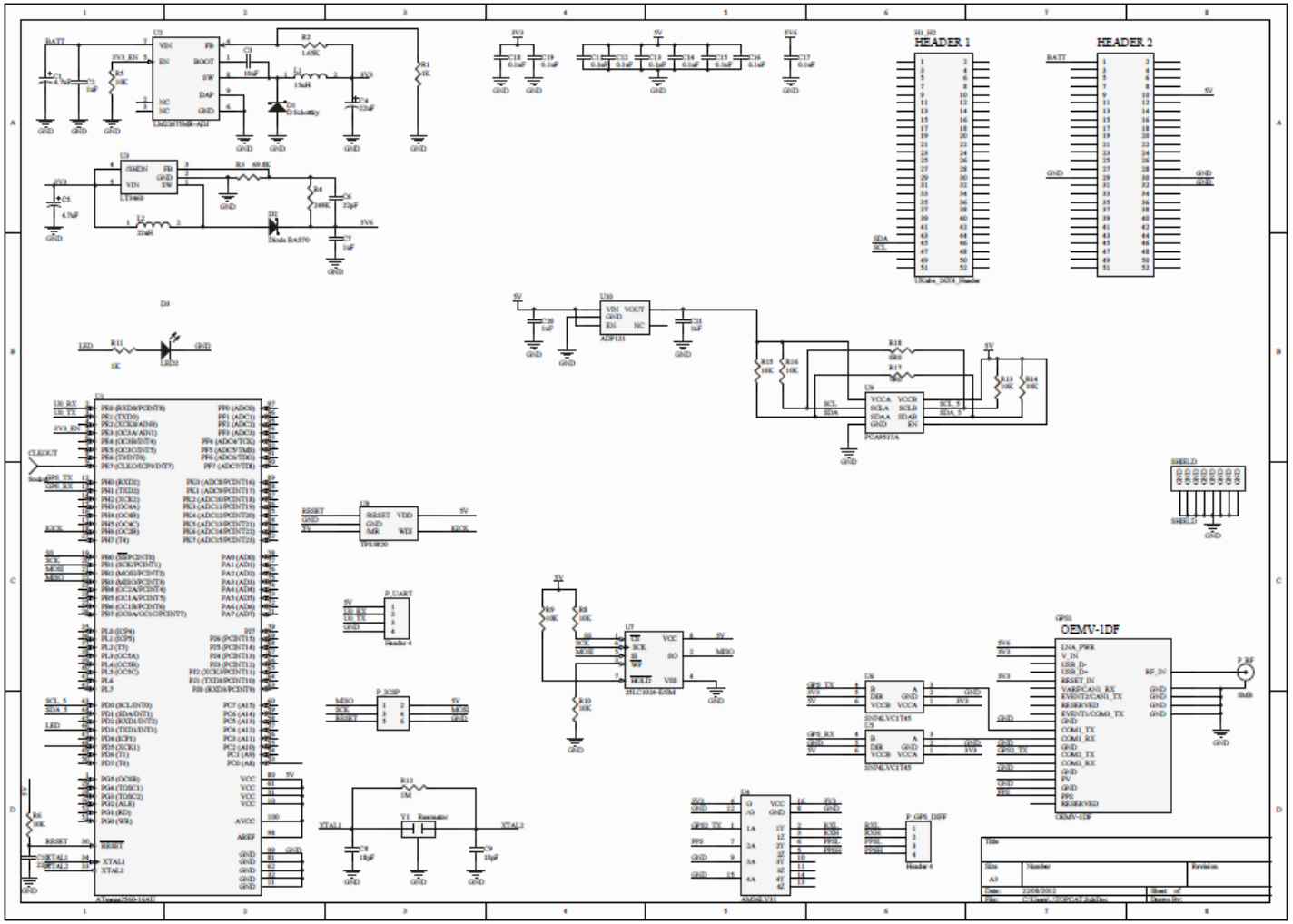

Figure A1.1 TOPCAT controller board schematic

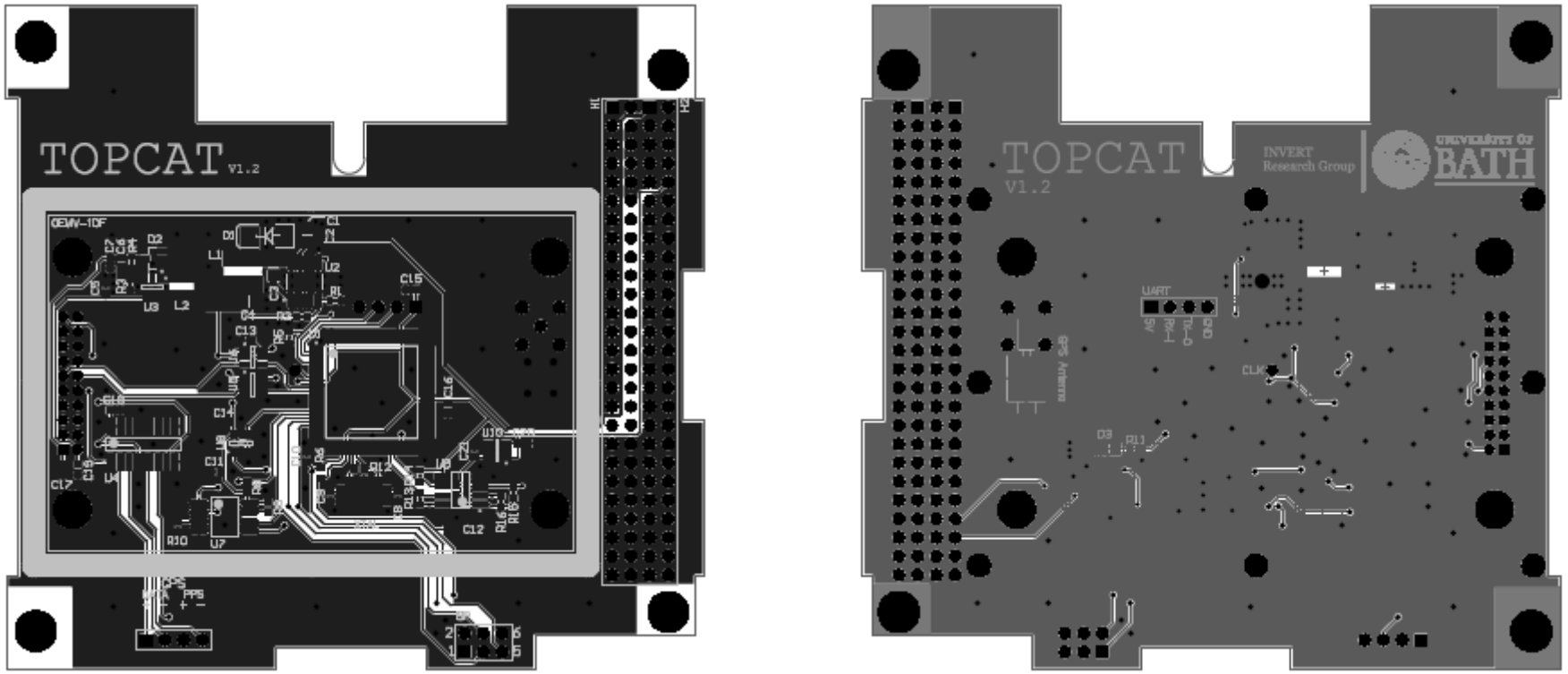

PCB Layout – Front Face

PCB Layout – Back Face

Figure A1.2 TOPCAT controller board PCB layout

A1.2 Parameter and Error Handling

Table A1.1 Parameter Handling

Parameter	Description	R/W	Update /Read before Initialise?	Reset parameter value within platform to a defined value after issue?		Automated operation within TOPCAT s/w driver (implemented by PLATFORM)	Operation
				Y/N	Notes		
0x01	Number of GPS satellites as seen by the receiver	R	N	N/A	N/A	Param 0x01 is to be **read** after a status request poll and param 0x02 write, and before a mode update (if requested) **after initialisation**	
0x02	Priority data request by user (in packets)	RW	N	Y	Reset to value 0x0000	Param 0x02 should be written following a status request poll **and** data transfer command is issued. If priority data request is active, then normal data waiting should be ignored, and the requested amount of data should be transferred via priority data transfer.	On user request only. Default value: 0x0000
0x03	Maximum data memory allowed per orbit (in packets)	RW	Y	N	N/A	Param 0x03 should be written **only before** initialisation and after the first status request/error handling.	To be updated via user before payload initialisation. Default value: 0x0000, which would represent its inactive state. If value is non-zero, this would activate this parameter which would then represent the new desired maximum memory allowance.
0x04	User defined receiver initialisation delay	RW	Y	N	N/A	Param 0x04 should be written **only before** initialisation and after the first status request/error handling.	On user request only. Default value: 0x0005. This value represents the receiver

							initialisation wait time in **seconds.**
0x05	Disable/Enable EEPROM health check/status	RW	Y	Y	Reset to value 0x8000	Param 0x05 should be written after the following sequence: status request and error handling **before initialisation**; and status request, error handling, data transfer **after initialisation**. This parameter should be written both before and after initialisation command is given.	Default **(initial)** value: 0x81FF (if error 0x41 is not invoked); If error 0x41 count = 3: 0x812E; Subsequent writes of the parameter value should only be via user request (therefore, reset the value within the platform data pool to 0x8000).
0x06	Receiver reset commands (FRESET, RESET, UNLOGALL)	RW	N	Y	Reset to value 0x0000	Param 0x06 should be written after initalisation, and following the sequence status request poll, error handling, data transfer.	On user request only. Default value 0x0000
0x07	User controlled EEPROM memory erase	RW	N	Y	Reset to value 0x0000	Param 0x07 should be written after initalisation, and following the sequence status request poll, error handling, data transfer.	On user request only. Default value 0x0000
0x08	EEPROM page number to which a write was unsuccessful	R	N	N/A	N/A	On platform request following payload issue of error flag 0x46	
0x09	Microcontroller health	R	N	N/A	N/A	If Param 0x09 value = 0 for >10minutes, restart payload.	
0x0A	User defined no-lock timout values	RW	Y	N	N/A	Param 0x0A should be written **only before** initialisation and after the first status request/error handling.	On user request only. Default value: 0x001E. This value represents the no-lock timeout value in **minutes**.
0x0B	Disable error 0x46	RW	N	N	N/A	Param 0x0B should be written after initalisation, and following the sequence status request poll, error handling, data transfer.	On user request only. Default value 0x0000

0X0C	EEPROM page number to which a write was unsuccessful	R	N	N/A	N/A	On platform request following payload issue of error flag 0x48	
0x0D	Disable error 0x48	RW	N	N	N/A	Param 0x0D should be written after initalisation, and following the sequence status request poll, error handling, data transfer.	

Table A1.2 Error Handling

Error Code	Description	Action	Repeatable automatically after 1st issue?	Notes
0x37	To be used under no-lock condition.	Restart (x3 attempts) and shut down	N	Need an error counter within platform
0x39	Indicates failure of restoration of EEPROM head/tail (read/write) position. EEPROM chip erased.	Log error	N	
0x40	All memory allocated for the orbit used. Not treated as an error	Shutdown payload	N	
0x41	Indicates EEPROM health check failure.	Attempt 0: Restart; Attempt 1: Restart; Attempt 2: Platform uploads parameter 0x05 (0x912E)	N	Need an error counter within platform
0x42	EEPROM health check failure - Change to manual parameter update	Allows user to update parameter 0x05		
0x44	Restore state from external EEPROM failed	Log error	N	
0x45	Restore state from internal EEPROM failed	Log error	N	
0x46	EEPROM page write was unsuccessful	Read parameter 0x08	Y	
0x48	EEPROM byte write was unsuccessful	Read parameter 0x0C	Y	

A1.3 Data Packet Breakdown

Table A1.3 Data Packet Summary

Data	Sampling description	Data Size (Bytes)		Assumptions/Comments
		30min @ 10sec sampling (Optimal) i.e. **180 samples**	10min @ 20sec sampling (Reduced data rate) i.e. **30 samples**	
Rawephem	Message generated only when the values change	134 x 10 = **2K**		Data value quoted is from empirical data obtained on ground. This is likely to increase during space observations. The number of satellites tracked here is assumed to be 10.
Rxstatusevent	Message generated only when the status changes	**76**		Data value quoted is from empirical data obtained on ground. This is likely to increase during space observations.
Rangecmp	Each sampling will carry 276Bytes of data, regardless of sampling frequency	520 x 180 = **92K**	520 x 30 =**16K**	The number of satellites considered is 10. This may increase when in orbit due to greater visibility
Bestpos	Each sampling will carry 104Bytes of data, regardless of sampling frequency	104 x 180 = **19K**	104 x 30 = **4K**	
Total		**114K**	**23K**	
		~6kB/min	~3.5kB/min	

Table A1.4 Data Packet Breakdown

Field Name	Description	Binary Bytes	Binary Offset	Comments
Packet Header	Mandatory slave response header	2	0	Mandatory in each packet
Packet counter	Data packet number for packet tracking	2	2	
Data Header (H)				**Data header will precede each message. The binary offset listed for the header is for the initial packet, after which it will be included before each message in a rolling buffer format**
Sync	Message start identifier	3	4	
Header Length	Length of the header	1	7	
Message ID	Message ID number of the position/navigation log	2	8	
Message Type	Binary/Ascii	1	10	
Port Address	COM port value	1	11	
Message Length	Length in bytes of the body of the message. Does not include the header *or* the CRC	2	12	
Sequence	To be used if multiple related logs are requested	2	14	
Idle Time	Processor idle time between successive logs	1	16	
Time Status	Quality of the GPS time	1	17	
Week	GPS week number	2	18	
ms	Milliseconds from the beginning of the GPS week	4	20	
Rx Status	Status of hardware and software of the receiver between successive logs with the same message ID	4	24	
Reserved	Reserved for internal use	2	28	
Rx S/W Version	Receiver software build number	2	30	
Total DataHeader Size		**28**		**Messages to be added to the packet in segments of 228 bytes in a rolling**
Messages				

Rawephem		***Raw ephemeris – raw binary information for subframes one, two and three from the satellite***			**buffer format following a data header. Any packet with less than 256 bytes of data will be padded as pre PIR-288**
prn		Satellite PRN number	4	H	
ref week		Ephemeris reference week number	4	H+4	
ref secs		Ephemeris reference time (s)	4	H+8	
subframe1		Subframe 1 data	30	H+12	
subframe2		Subframe 2 data	30	H+42	
subframe3		Subframe 3 data	30	H+72	
CRC		32-bit CRC	4	H+102	
Rxstatusevent		***Status event indicator – Event messages for the receiver status***			
word		The status word that generated the event message	4	H	
bit position		Location of the bit in the status word	4	H+4	
event		Event type	4	H+8	
description		Text description of the event or error	32	H+12	
CRC		32-bit CRC	4	H+44	
Rangecmp		***Compressed version of range comprising the channel measurements for the currently tracked satellites***			
#obs		Number of satellite observations with information to follow	4	H	
1st range record	Channel Tracking Status Doppler Frequency Pseudorange (PSR) ADR StdDev-PSR StdDev-ADR		44	H+4	

	PRN/slot Lock Time C/No Reserved			
Next rangecmp		Range records for each observation	H+4+ (#obs x 44)	
CRC		32-bit CRC	4	H+4+ (#obs x 44)
Bestpos		***Gives the best available combined GPS and inertial navigation system position computed by the receiver***		
sol sat		Solution status	4	H
pos type		Position type	4	H+4
lat		Latitude	8	H+8
lon		Longitude	8	H+16
hgt		Height above mean sea level	8	H+24
undulation		Relationship between the geoid and the ellipsoid (m) of the chosen datum	4	H+32
datum id#		Datum ID number	4	H+36
lat s		Latitude standard deviation	4	H+40
lon s		Longitude standard deviation	4	H+44
hgt s		Height standard deviation	4	H+48
stn id		Base station ID	4	H+52
diff_age		Differential age in seconds	4	H+56
sol_age		Solution age in seconds	4	H+60
#SVs		Number of satellite vehicles tracked	1	H+64
#solnSVs		Number of satellite vehicles used in solution	1	H+65
#ggL1		Number of GPS plus GLONASS L1 used in solution	1	H+66

#ggL1L2	Number of GPS plus GLONASS L1 and L2 used in solution	1	H+67	
Reserved	Reserved for internal use	1	H+68	
ext sol stat	Extended solution status	1	H+69	
Reserved	Reserved for internal use	1	H+70	
sig mask	Signals used mask – if 0, signals used in solution are unknown	1	H+71	
CRC	32-bit CRC	4	H+72	
Packet CRC	Mandatory slave response CRC	2		Mandatory in each packet

A1.4 Hardware Design Challenges

Table A1.5 Hardware Design Challenges

Issue		Description	Measures Taken	Comments
RF	Antenna and receiver could not be successfully integrated to obtain GPS lock	An initial investigation was carried out to ensure the pair's operation was successful. However the mounting design for the antenna was significantly changed, reducing the ground plane to a 42x42 mm housing. This was to be assembled on the PCB placed within the chassis, thus viewing through a skeletonized wall opening.	After extensive investigation it was concluded that the ground plane area was inadequate for the antenna. The mechanical placement was re-designed to place the antenna in contact with the solar panel, with the antenna extending out from the cubesat wall.	Antenna performance needs to be tested extensively together with the flight receiver at each design revision, before the hardware is frozen.
Mechanical	Mechanical incompatibility between antenna mount and window of the solar panel/chassis	The change of design to place the antenna on the solar panel was decided when both the satellite and payload designs were mature. The window was initially intended only for the antenna to 'look through', rather than to insert both the antenna and its housing through. Thus, the module could not be fitted in the cut-out. Since the solar panels were developed in line with the cubesat chassis no further changes could be implemented to the satellite structure.	Given the limitations in changing the solar panel window, the remaining alternative was to further modify the antenna mounting/ground plane to ensure compatibility – that resulted in a very stringent fit! Tests were carried out to ensure the performance with the new ground plane was satisfactory. Final clearance between the solar panel and the mount were a few fractions of mm!	
	PCB manufacture tolerances were incompatible	It was discovered following board manufacture that the board dimensions - particularly the mount points of the board to the satellite chassis - had deviated by a small but significant amount.	A new set of PCBs were manufactured by the same company that was developing platform boards to ensure the tolerances remained similar.	

Electrical	Power voltage specifications insufficient for receiver/antenna operation	Given Ukube-1 is capable of providing both 3.3V and 5V power rails to the payload, it was initially decided to use these supplies to operate the receiver at 3.3V and antenna at 5V. The specified tolerance in each rail was ±1%. However, the receiver voltage tolerances were very stringent such that a voltage of 3.27V rendered the device inoperable. Further, it was determined that the antenna needed a minimum voltage of 5.6V to be powered.	Given the issues, it was decided to use the unregulated BatV supply from Ukube-1 power rails and down convert it to the desired voltage values. Thus, BatV was regulated to 3.4V for the receiver and 5.7V for the antenna separately via two power regulators.	
	Underrated Inductor	An inductor expected to be sufficient for the power regulator circuit failed from the stress experienced during thermal/vacuum testing. No prior symptoms were seen to indicate its unsuitability.	The inductor was replaced by another that had a higher current rating. However, since this was significantly heavier than the previous inductor, concerns were raised regarding its performance during vibration. This was addressed by glue-locking the inductor after soldering.	
	Highly sensitive buck converter (power regulator for converting 8V to 3.4V)	The voltage regulator TPS62050 device was observed to frequently 'burn out' following soldering. This was traced back to the continuity check usually done when hand- soldering surface mount components. The device was highly sensitive to the bias voltage of the multimeter, causing it to get damaged.	The voltage regulator was replaced by a more robust device capable of handling a small voltage bias, as well as T/V cycles and vibration.	
	Brown-out condition of the uC due to the I2C bus	As the I2C bus is common to all systems within UKube-1 it is constantly powered. Since interface specifications do not allow pull-up resistors to be implemented on the signal lines, the bus was not isolated from the payload. This resulted in a current injection from the powered I2C bus into the uC via the signal pins, causing a brown out	After many attempts to isolate the bus without pull up resistors (switches, diode, powered voltage translators etc.) to no avail, a level translating I2C bus repeater (PCA9517A) was used to successfully isolate the payload from the I2C bus.	

		condition.		
Communication	Timing inconsistency between I2C and SPI data transfers	During continuous data transfer the payload was seen to consistently get reset by the watch dog timer (WDT). After extensive investigations the problem was traced back to the priority levels between I2C and SPI interrupts. SPI, used for communication with the EEPROM has a higher priority setting than I2C. Thus, if large amounts of data are available, the uC continues to transfer data without responding to the regular status poll from the platform via I2C. Since the platform is programmed to wait for a response or repeat the status poll, the I2C lines are held low throughout this process. This is perceived by the payload uC as the signal lines being busy, thus not servicing the WDT. After a time period without a response from the uC, the WDT assumes a uC malfunction and resets the unit.	Since payload reset frequency increased with increasing number of data to be transferred from payload to platform, a limited number of packets were buffered into uC RAM from the EEPROM, using SPI. When platform commands a data transfer, only these limited number of packets are sent, thus not requiring the use of the SPI bus in between I2C data transfers.	Need to ensure priority levels of interrupts before freezing the hardware/communication designs.
Testing	RF signal availability during T/V testing and false positive results	Since GPS signal reception was not possible within the T/V chamber, a simulator was used to radiate the signal into the chamber, whose signal strength was very high. This resulted in a false positive when the voltage regulator for the antenna was damaged, and failed to power the antenna. This was because the signal was strong enough to effectively 'leak' through the RF link, thus appearing as the signal from the antenna entering the receiver.	Subsequent T/V tests were conducted with RF/antenna testing. These tests were done with true GPS signals once the payload was removed from the chamber. Regarding the failed voltage regulator, it was concluded that the device was not damaged due to T/V testing, but was faulty. This was confirmed during the second batch of T/V test, when the component worked successfully.	

	Insufficient monitoring during radiation tests	While continuous monitoring was conducted of the current consumption and data transfer, detailed investigation into points and modes of failure was not possible to be discerned from the results obtained; although sufficient information was available to identify the main points of failure. For example, random data transfer and power cycling during irradiation was not performed.	The data available was used to indirectly identify possible failure of components.	Need to implement power cycling and output more information on the functionality of each sub-system during irradiation. Of particular importance is power cycling, as this accesses memory regions of the uC which are not normally used following boot-up.
Board Manufacture (Assembly)	Misinterpretation of manufacturing instructions	As the board needed to be manually populated by a different company unfamiliar with the design, there was a risk of misinterpretation of the instructions.	A manufacturing pack was provided to the company concerned, with detailed documents, photos and step-by-step instructions (Appendix 2).	
Logistics	Use of an unsuitable GPS receiver with lower specifications as the payload instrument	Due to an error in logistics, the commercial dual-frequency GPS receiver used as the payload's instrument is not suited for science-based space applications. This is because the bandwidth has been restricted resulting in the elimination of satellites whose Doppler shifts are beyond the limited bandwidth. The impact of the issue was magnified as the logistical error was identified immediately prior to delivery of the payload for satellite integration.	Although a firmware upgrade was intended to increase the bandwidth, the process was deemed too risky at the stage of the project. Further, it was discovered that the restriction in the number of satellites viewed may act as an advantage due to limitations in the uC RAM to receive large packets of data from the receiver.	

Appendix 2 – Test Results

A2.1 Mechanical Vibration Test Results

UCL	**Project: TopCat** **MULLARD SPACE SCIENCE LABORATORY** **UNIVERSITY COLLEGE LONDON** **Author:** Berend Winter

TITLE: TOPCAT VIBRATION TEST REPORT

Document Number: TOPC-MSSL-TR-001. Issue 1 Date 17/Sep/12

Distribution:

University of Bath	T. P. Jayawardena	X
Clyde Space		
Mullard Space Science Laboratory	B. Winter	X
	A Rousseau	
	A. Spencer	
	G. Davison	

CHANGE RECORD

ISSUE	DATE	PAGES CHANGED	COMMENTS
A	17/Sept/2012	ALL	First issue

CONTENTS

1 Scope 135
2 Nominative Documents 135
3 Informative Documents 135
4 Glossary 135
5 Requirements found in various documents 136
6 Participants required 136
7 Test Log 137
7.1 X – Axis 139
7.2 Y – Axis 144
7.3 Z – Axis 149
8 Conclusions 154

Scope

This document reports the TOPCAT vibration test results in a short format. The requirements that needed to be met are listed in section 5. The participants during the test and their responsibilities are listed in section 6. Section 7 lists the log book as it was kept prior to, during, and after the test. The TOPCAT instrument was tested without the antenna. There were no formal identifications or build status listed or logged. The model is an EM type model.

Nominative Documents

Label	Title	Number

Informative Documents

Label	Title	Number
IR (1)	ISOPOD Interface Specification	ISIS.IPOD.ICD.001V 1.4
IR (2)	Thermal Vacuum Test Procedure	UKB1.TN.015 (draft)
IR (3)	UKube Payload Interface Document	UKUB.RS.001.ISS04

Glossary

AQM	Assembly Qualification Model
TOPCAT	Topside ionospheric computer assisted tomography
FM	Flight Model
NRB	Nonconformance Review Board
MSSL	Mullard Space Science Laboratory
NA	Not Applicable
TBC	To Be Confirmed
TBD	To Be Defined

TRB	Test Review Board
TRR	Test Readiness Review

Requirements found in various documents

From IR(1) (they are not numbered) at qualification level.

Lowest natural frequency above 90 Hz

Sine vibration at 4 g (10-100 Hz with 1" stroke limitation)

Random vibration test

20 to 50 Hz 0.026 to 0.16 g2/Hz

50 to 800 Hz maintain 0.16 g2/Hz

800 to 2000 Hz decrease to 0.026 g2/Hz

Sine burst at 40 Hz 15 g (10 cycles)

Shock load 1 kg between 1 kHz and 10 kHz ramp up from 100 Hz (20 g)

IR(2) Deals with the thermal cycling test only

From IR(3)

PIR-188 Random Vibration, 14.1 g-rms for qualification and 10.0 g-rms for acceptance

PIR-190 The designed for natural frequency of the Payload shall exceed the resonances of the launch vehicle by a factor of two.

PIR-191 The minimum designed natural frequency of the payload shall exceed 150 Hz

PIR-192 Any vibration resonances or shock to which a subsystem may be particularly susceptible shall be identified by the payload developer.

Participants present

Representative from Bath university, Talini Pinto Jayawardena

Test Manager, Berend Winter

Test operator, Berend Winter

Test Log

14 September 2012

13:00 Talini delivered the TOPCAT pcb with the GPS motherboard. Vibration base plate was ultrasonically cleaned and the TOPCAT PCB assembly was cleaned with IPA on the outside only. Some flux appeared through holes at the bottom of the PCB. Clearly this PCB has to be cleaned more thoroughly after the vibration test and prior to the thermal vacuum test.

16:00 Mounted on the shaker wearing wrist bands as a precaution. Doug Davies stacked the bolts and we left the assembly on the shaker for the epoxy (de-gassed Stycast 2216) to set during Saturday. Talini performed a functional test and all was found to be in order.

2012-09-16 Sunday, 10:00. Started preparation for the vibration test. Mounted two accelerometers on the base plate to assist in control and three on the GPS enclosure for sine sweep peak resonance verification. We took photos, prior and after mounting the accelerometers.

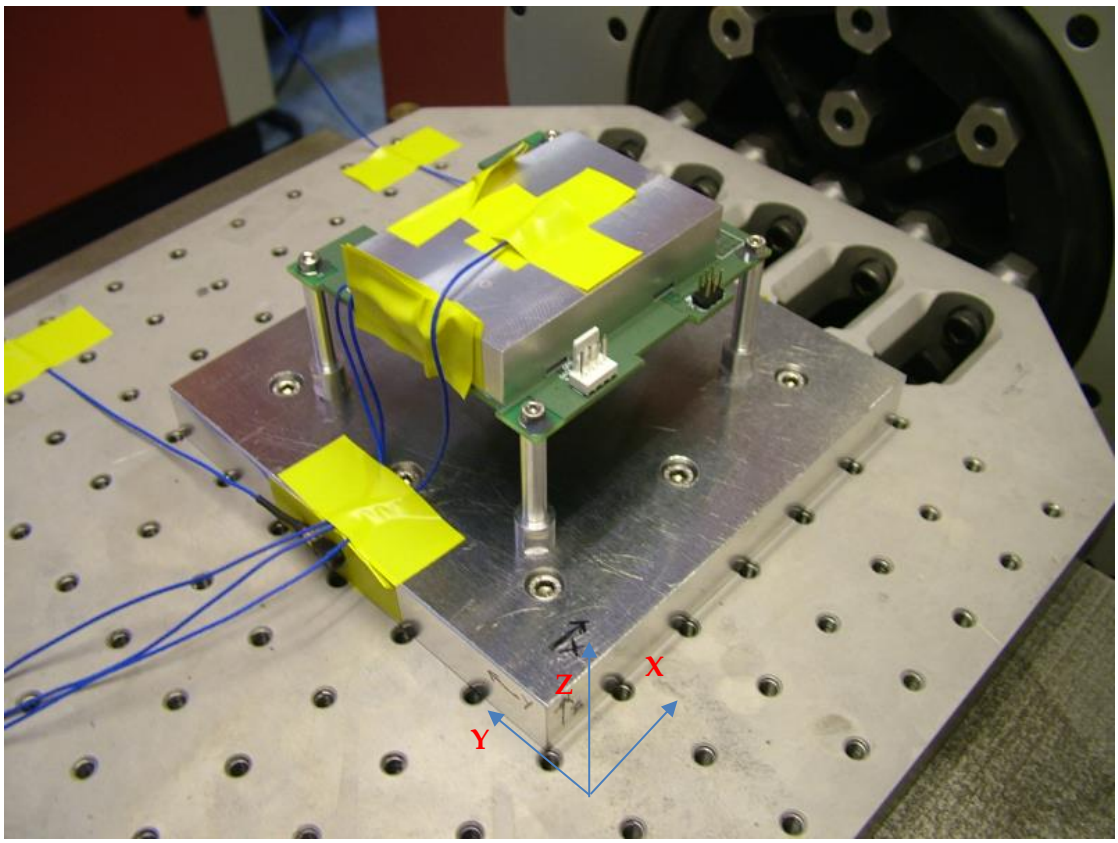

Test Set Up

The following specifications were taken from TOPC-MSSL-PR-002. Issue A

Random Vibration Qualification Levels (All axes)

In Z direction		
Frequency	Level	Slope
20		+6 dB/Oct
50	0.16 g2/Hz	
800	0.16 g2/Hz	
2000		-6 dB
Total	14.1 g-rms	

Test duration for random qualification is 120 sec

Sine Qualification Vibration test levels (All axes)

In X direction	
Frequency	Level
10	4 g
100	4 g

Sweep rate 2.0 Oct/min

The test procedure also calls for sine bursts, these will be applied using a short sine sweep with the required levels reached for a minimum of 10 cycles.

Sine Burst

Direction	Frequency	Level	Cycles
X,Y and Z	40 Hz	15 g	10

Sine burst was performed as a sweep at 0.8 oct/min between 40 and 40.1 Hz. Resulting in 10 cycles at 15 g.

X – Axis

	Project	UKCUBE					University of Bath	
	Model or Serial Number	NA						Add model or serial number
	Part/Drawing Number	NA						Add drawing number
	Date of manufacture	?						
	Mass	? kg						
	X-AXIS						Notes	
	Pre-Test	Date	Time	Input		Units	Check	
1	Mass Measurement			?		kg		
2	Mount on Shaker	14/09/2012	15:38				BW	
3	Visual Inspection	16/09/2012					BW	Basic check to verify hardw are looks ok, sensor w iring is secured and tools are removed from shaker and take photos
4	Torques checked	NA				Nm		Angular control, glue locked
5	Electrical Inspection	NA						At least a basic electrical health check
	Sine Sweep		11:00	FR1772			BW	Add FR number (facility run number) and add to facility log book
6	Control							Check for control (10.1 average)
7	Charge Amplifier						BW	Check it is w orking and that the filter and integration settings are correct
8	Input Levels				0.2	g	BW	Check max input levels (prevent clipping)
9	Sweep Rate				1	oct/min	BW	
10	Levels						BW	Check Levels are according to spec (sec 19)
11	Test run File		11:42	SineSweep_002			BW	
12	Short Visual						BW	
	Sine Qual	16/09/2012	11:47	FR1773				Add FR number (facility run number) and add to facility log book
13	Control						BW	Check for control (10.1 average)
14	Charge Amplifier						BW	Check it is w orking and that the filter and integration settings are correct
15	Input Levels						BW	Check max input levels (prevent clipping)
16	Sweep Rate				2	oct/min	BW	
17	Levels				4	g	BW	Check Levels are according to spec (sec 19)
18	Frequency				50	Hz		
19	Test run File		12:00	SineQualTest X-Axis_002				
20	Short Visual							
	Sine Sweep		12:01	FR1774			BW	Add FR number (facility run number) and add to facility log book
21	Control							Check for control (10.1 average)
22	Charge Amplifier						BW	Check it is w orking and that the filter and integration settings are correct
23	Input Levels				0.2	g	BW	Check max input levels (prevent clipping)
24	Sweep Rate				1	oct/min	BW	
25	Levels						BW	Check Levels are according to spec (sec 19)
26	Test run File		12:09	SineSweep_003			BW	
27	Short Visual						BW	
	Sine Burst		12:00	FR1775				Add FR number (facility run number) and add to facility log book
28	Control							Check for average control
29	Charge Amplifier							Check it is w orking and that the filter and integration settings are correct
30	Input Levels							Check max input levels (prevent clipping)
31	Sweep Rate				0.8	oct/min		Check sw eep rate according to spec
32	Levels				15	g		Check Levels are according to spec
33	Test run File		12:25	Sine Burst_003				
34	Short Visual							
	Sine Sweep		12:26	FR1776			BW	Add FR number (facility run number) and add to facility log book
35	Control							Check for control (10.1 average)
36	Charge Amplifier						BW	Check it is w orking and that the filter and integration settings are correct
37	Input Levels				0.2	g	BW	Check max input levels (prevent clipping)
38	Sweep Rate				1	oct/min	BW	
39	Levels						BW	Check Levels are according to spec (sec 19)
40	Test run File		12:33	SineSweep_004			BW	
41	Short Visual						BW	
	Random Qual		12:38	FR1777				Add FR number (facility run number) and add to facility log book
42	Control						BW	Check for average control
43	Charge Amplifier						BW	
43	Channel Input Levels						BW	
44	Duration				120	sec	BW	
45	Levels				14.1	g-rms	BW	
46	Test run File		12:51	RandomTest Qual X-Axis_003			BW	
47	Short Visual						BW	
	Sine Sweep		12:52	FR1778			BW	Add FR number (facility run number) and add to facility log book
48	Control							Check for control (10.1 average)
49	Charge Amplifier						BW	Check it is w orking and that the filter and integration settings are correct
50	Input Levels				0.2	g	BW	Check max input levels (prevent clipping)
51	Sweep Rate				1	oct/min	BW	
52	Levels						BW	Check Levels are according to spec (sec 19)
53	Test run File		12:59	SineSweep_005			BW	
54	Short Visual						BW	

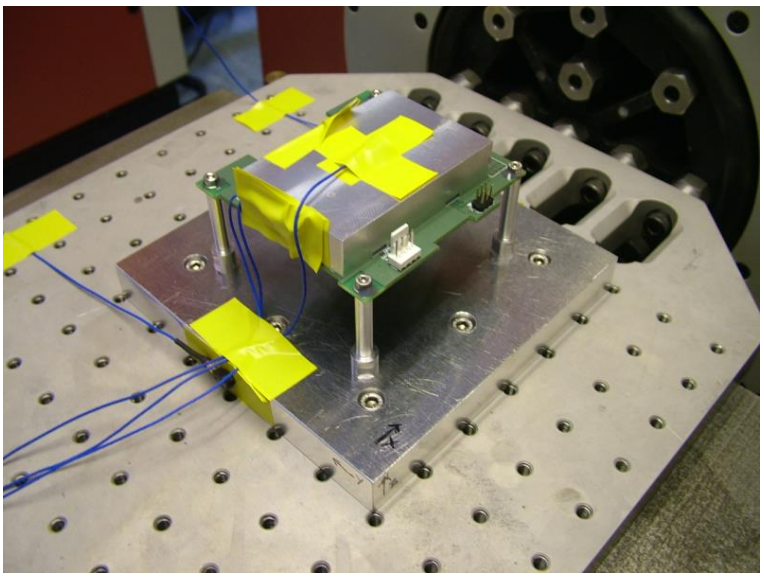

X-axis test configuration

Initial sine survey

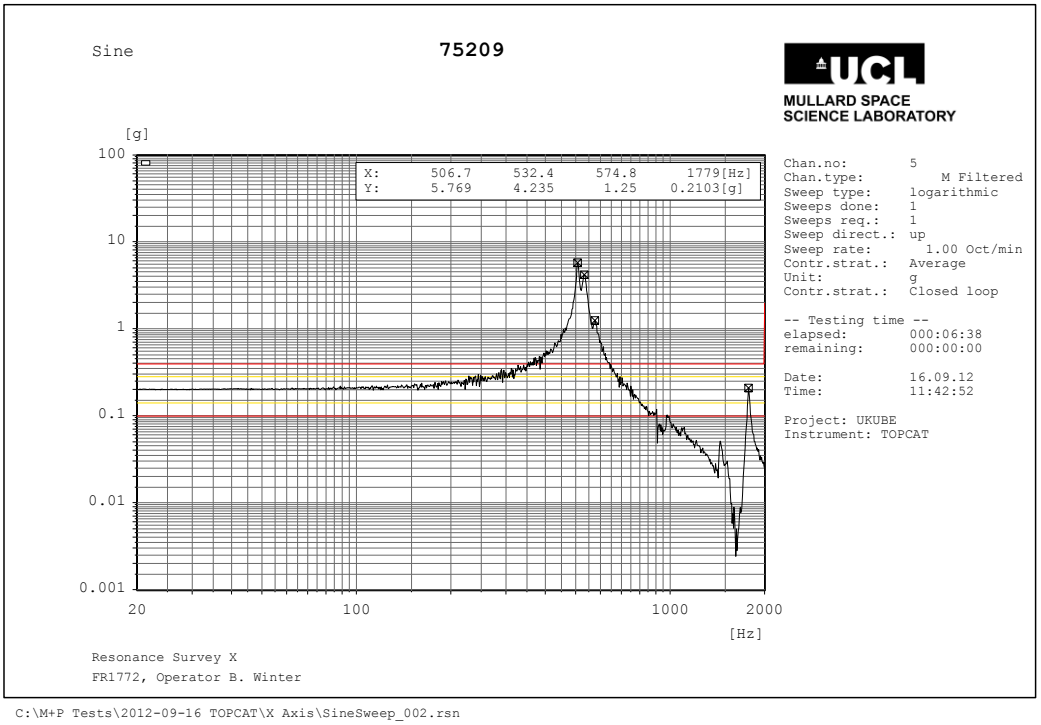

C:\M+P Tests\2012-09-16 TOPCAT\X Axis\SineSweep_002.rsn

Sine Qualification

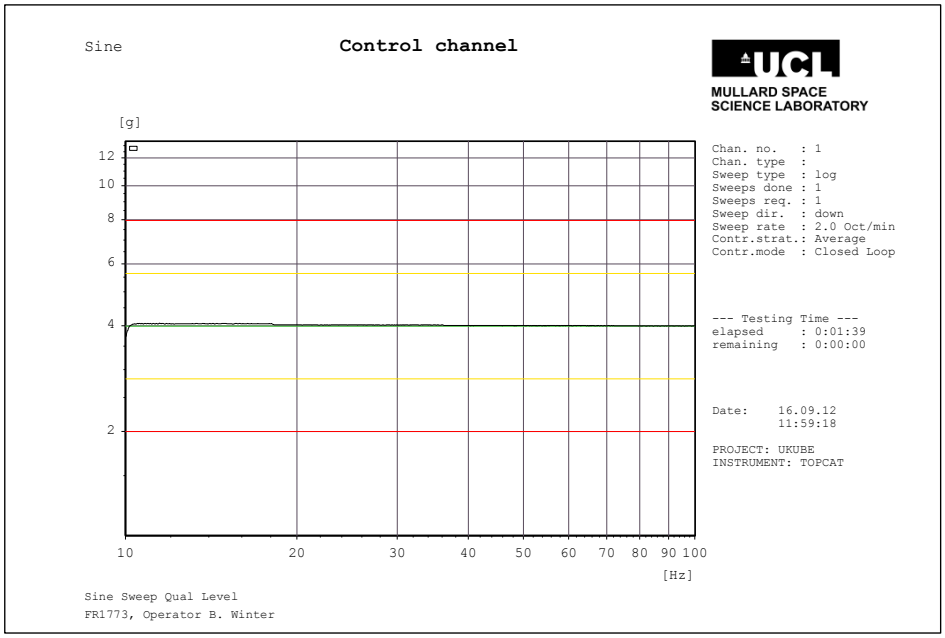

C:\M+P Tests\2012-09-16 TOPCAT\X Axis\SineQualTest X-Axis.tsn

Sine survey comparison (pre-post Sine Vibration)

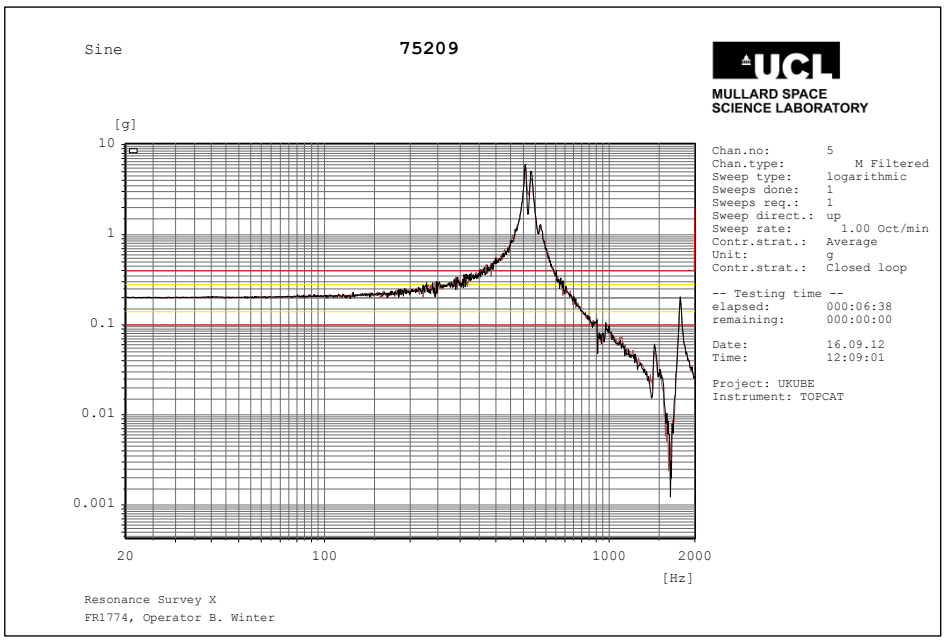

C:\M+P Tests\2012-09-16 TOPCAT\X Axis\SineSweep_003.rsn

Sine Burst

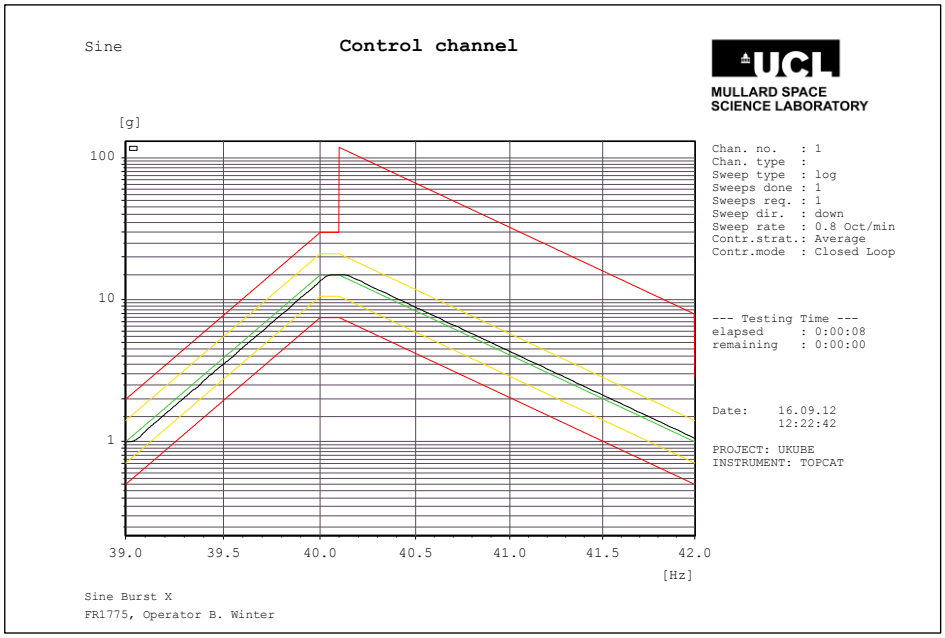

C:\M+P Tests\2012-09-16 TOPCAT\X Axis\Sine Burst.tsn

Sine survey comparison (pre-post sine burst)

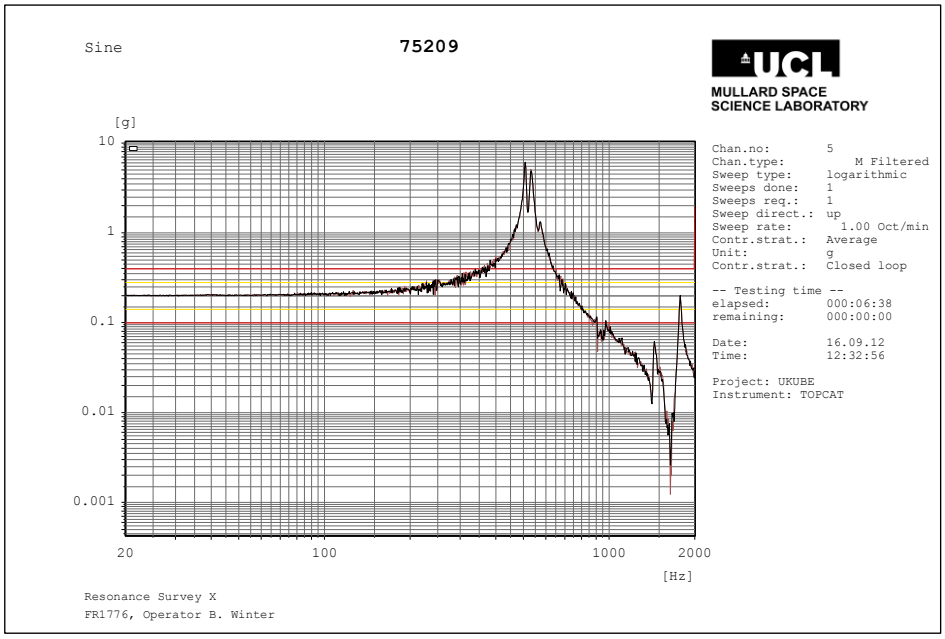

C:\M+P Tests\2012-09-16 TOPCAT\X Axis\SineSweep_004.rsn

Random Qualification

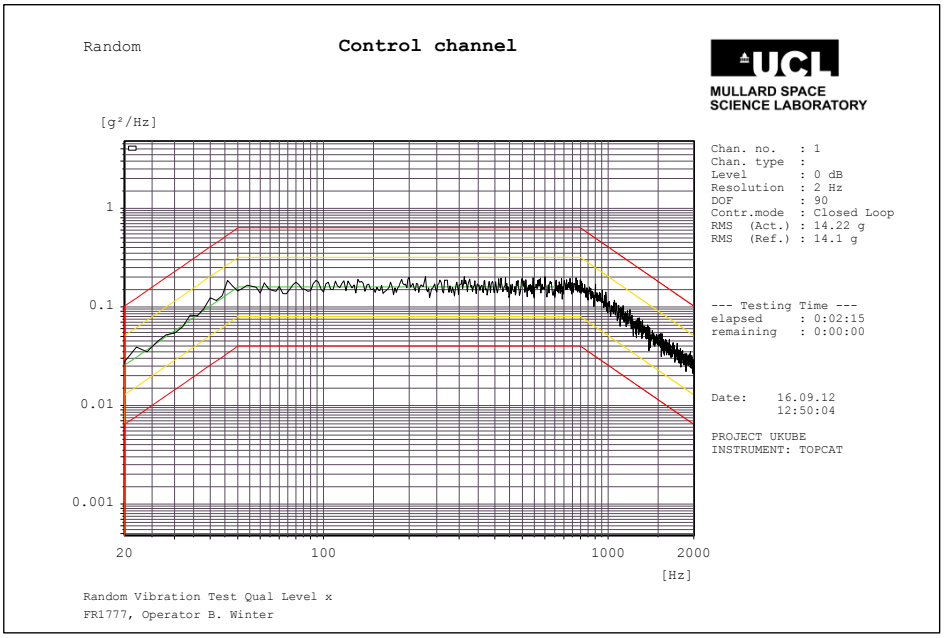

C:\M+P Tests\2012-09-16 TOPCAT\X Axis\RandomTest Qual X-Axis.trn

Sine survey comparison (pre-post test)

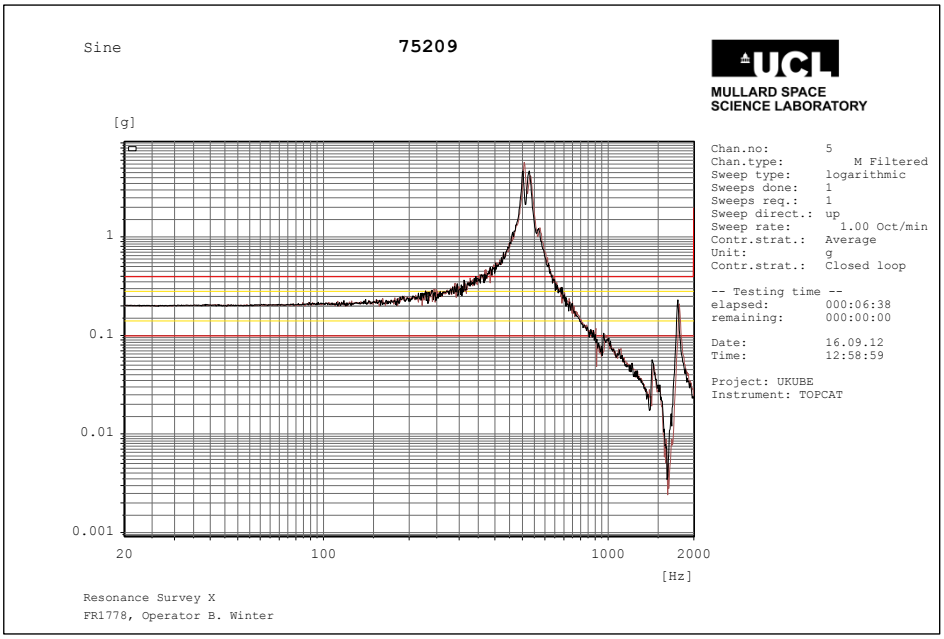

C:\M+P Tests\2012-09-16 TOPCAT\X Axis\SineSweep_005.rsn

There are a few small shifts, this is most likely due to settling of the PCB during the random vibration test. The frequency shifts (downwards) observed were between 0.5% to 1% and acceptable.

Y – Axis

	Project	**UKCUBE**					**University of Bath**	
	Model or Serial Number	**NA**						Add model or serial number
	Part/Drawing Number	**NA**						Add drawing number
	Date of manufacture	**?**						
	Mass	**? kg**						
	Y-AXIS						Notes	
	Pre-Test	Date	Time	Input	Units	Check		
1	Mass Measurement			?	kg			
2	Mount on Shaker	16/09/2012	13:00			BW		
3	Visual Inspection	16/09/2012				BW		Basic check to verify hardware looks ok, sensor wiring is secured and tools are removed from shaker and take photos
4	Torques checked	NA			Nm			Angular control, glue locked
5	Electrical Inspection	NA						At least a basic electrical health check
	Sine Sweep	16/09/2012		FR1779		BW		Add FR number (facility run number) and add to facility log book
6	Control							Check for control (10.1 average)
7	Charge Amplifier					BW		Check it is working and that the filter and integration settings are correct
8	Input Levels			0.2	g	BW		Check max input levels (prevent clipping)
9	Sweep Rate			1	oct/min	BW		
10	Levels					BW		Check Levels are according to spec (sec 19)
11	Test run File		13:19	SineSweep_001		BW		
12	Short Visual					BW		
	Sine Qual	16/09/2012		FR1780				Add FR number (facility run number) and add to facility log book
13	Control					BW		Check for control (10.1 average)
14	Charge Amplifier					BW		Check it is working and that the filter and integration settings are correct
15	Input Levels					BW		Check max input levels (prevent clipping)
16	Sweep Rate			2	oct/min	BW		
17	Levels			4	g	BW		Check Levels are according to spec (sec 19)
18	Frequency			50	Hz			
19	Test run File		13:23	SineQualTest Y-Axis_001				
20	Short Visual							
	Sine Sweep			FR1781		BW		Add FR number (facility run number) and add to facility log book
21	Control							Check for control (10.1 average)
22	Charge Amplifier					BW		Check it is working and that the filter and integration settings are correct
23	Input Levels			0.2	g	BW		Check max input levels (prevent clipping)
24	Sweep Rate			1	oct/min	BW		
25	Levels					BW		Check Levels are according to spec (sec 19)
26	Test run File		13:56	SineSweep_002		BW		
27	Short Visual					BW		
	Sine Burst		13:57	FR1782				Add FR number (facility run number) and add to facility log book
28	Control							Check for average control
29	Charge Amplifier							Check it is working and that the filter and integration settings are correct
30	Input Levels							Check max input levels (prevent clipping)
31	Sweep Rate			0.8	oct/min			Check sweep rate according to spec
32	Levels			15	g			Check Levels are according to spec
33	Test run File		13:59	Sine Burst_001				
34	Short Visual							
	Sine Sweep		14:00	FR1783		BW		Add FR number (facility run number) and add to facility log book
35	Control							Check for control (10.1 average)
36	Charge Amplifier					BW		Check it is working and that the filter and integration settings are correct
37	Input Levels			0.2	g	BW		Check max input levels (prevent clipping)
38	Sweep Rate			1	oct/min	BW		
39	Levels					BW		Check Levels are according to spec (sec 19)
40	Test run File		14:09	SineSweep_003		BW		
41	Short Visual					BW		
	Random Qual		14:10	FR1784				Add FR number (facility run number) and add to facility log book
42	Control					BW		Check for average control
43	Charge Amplifier					BW		
43	Channel Input Levels					BW		
44	Duration			120	sec	BW		
45	Levels			14.1	g-rms	BW		
46	Test run File		14:14	RandomTest Qual Y-Axis_001		BW		
47	Short Visual					BW		
	Sine Sweep		14:15	FR1785		BW		Add FR number (facility run number) and add to facility log book
48	Control							Check for control (10.1 average)
49	Charge Amplifier					BW		Check it is working and that the filter and integration settings are correct
50	Input Levels			0.2	g	BW		Check max input levels (prevent clipping)
51	Sweep Rate			1	oct/min	BW		
52	Levels					BW		Check Levels are according to spec (sec 19)
53	Test run File		14:24	SineSweep_004		BW		
54	Short Visual					BW		

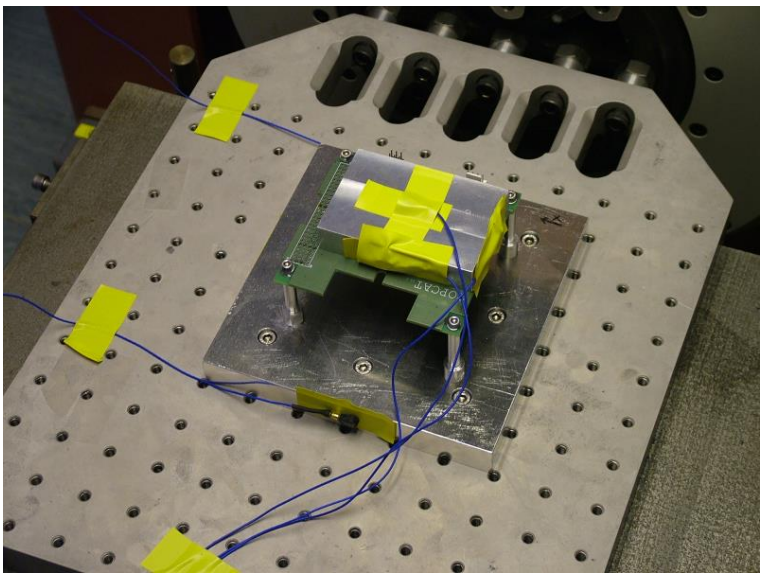

Y-axis test configuration

Initial sine survey

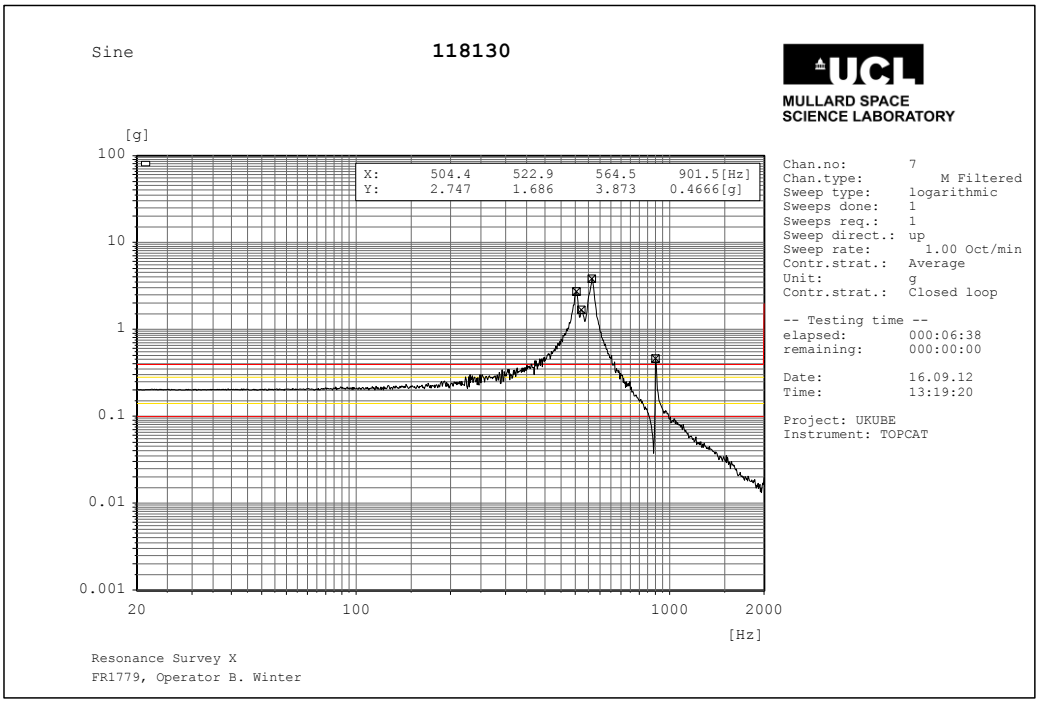

C:\M+P Tests\2012-09-16 TOPCAT\Y AXIS\SineSweep_001.rsn

Sine Qualification

C:\M+P Tests\2012-09-16 TOPCAT\Y AXIS\SineQualTest Y-Axis_001.rsn

Sine survey comparison (Pre-Post Sine Qualification)

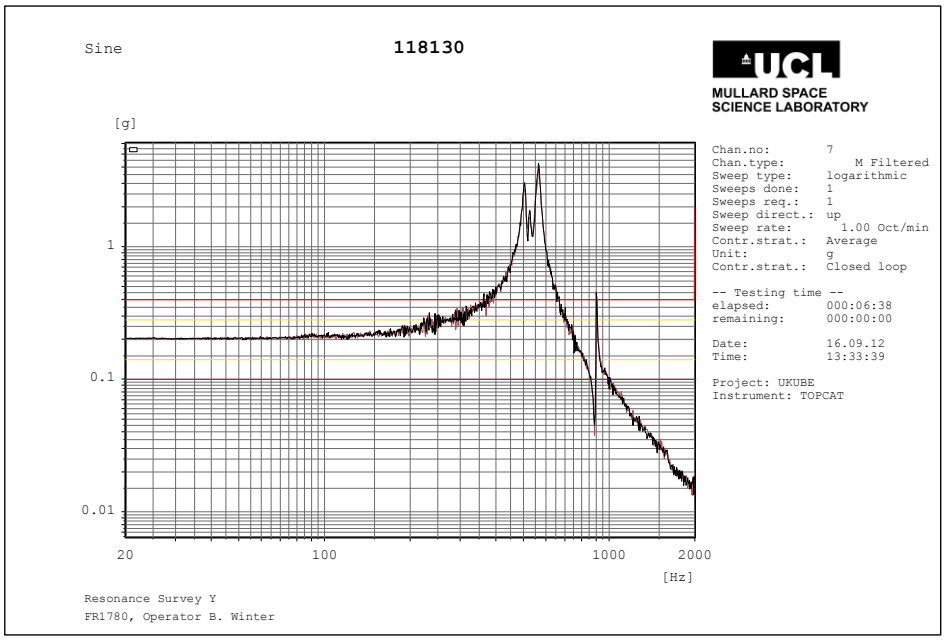

C:\M+P Tests\2012-09-16 TOPCAT\Y AXIS\SineSweep_002.rsn

Sine Burst

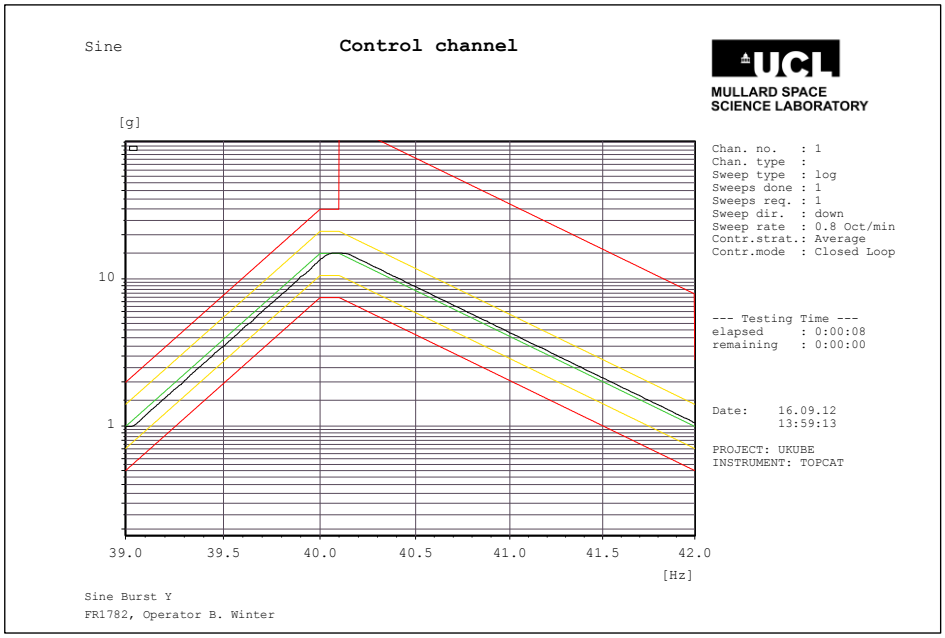

C:\M+P Tests\2012-09-16 TOPCAT\Y AXIS\Sine Burst.tsn

Sine survey comparison (Pre-Post Sine Burst)

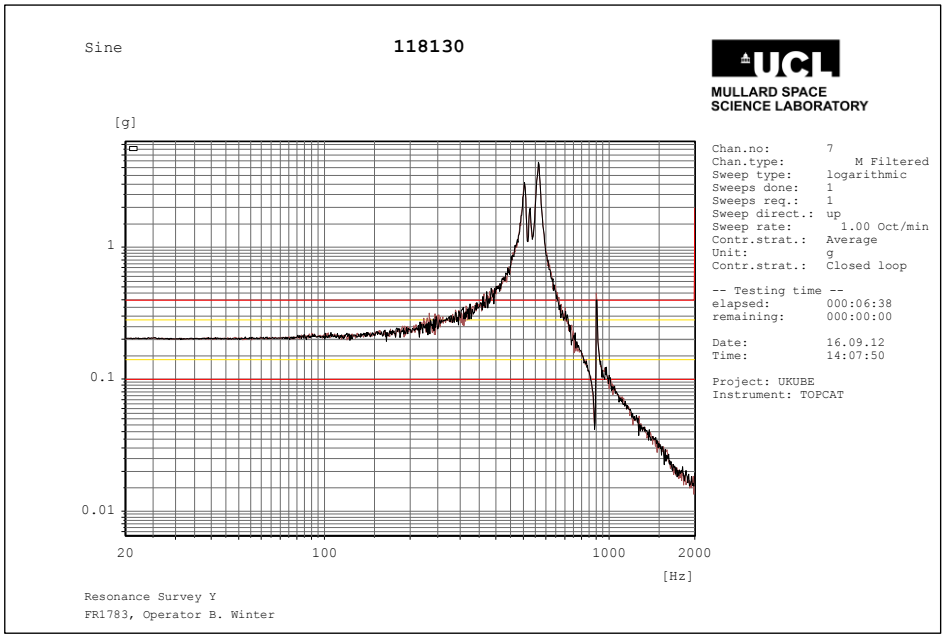

C:\M+P Tests\2012-09-16 TOPCAT\Y AXIS\SineSweep_003.rsn

Pre-Post verification

Random Vibration

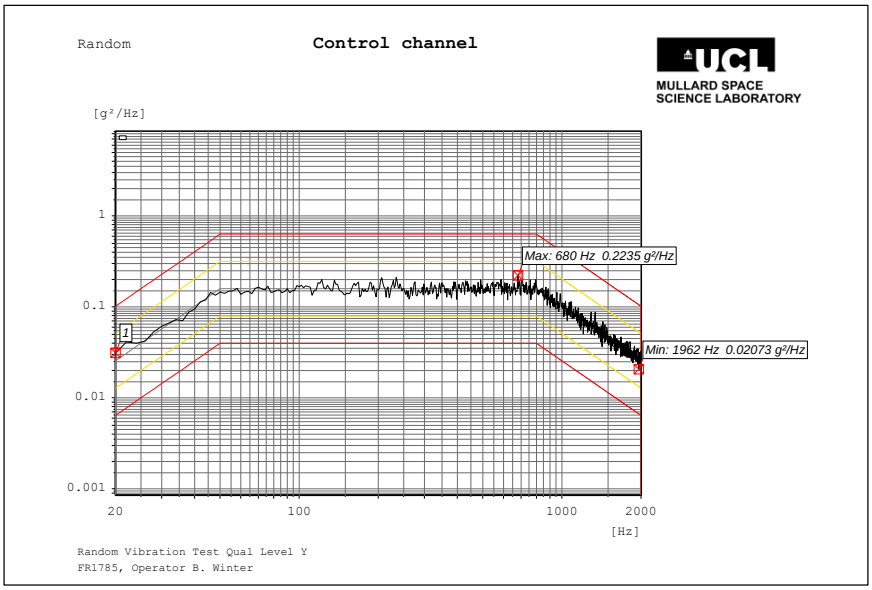

Sine survey comparison (Pre-Post Axis)

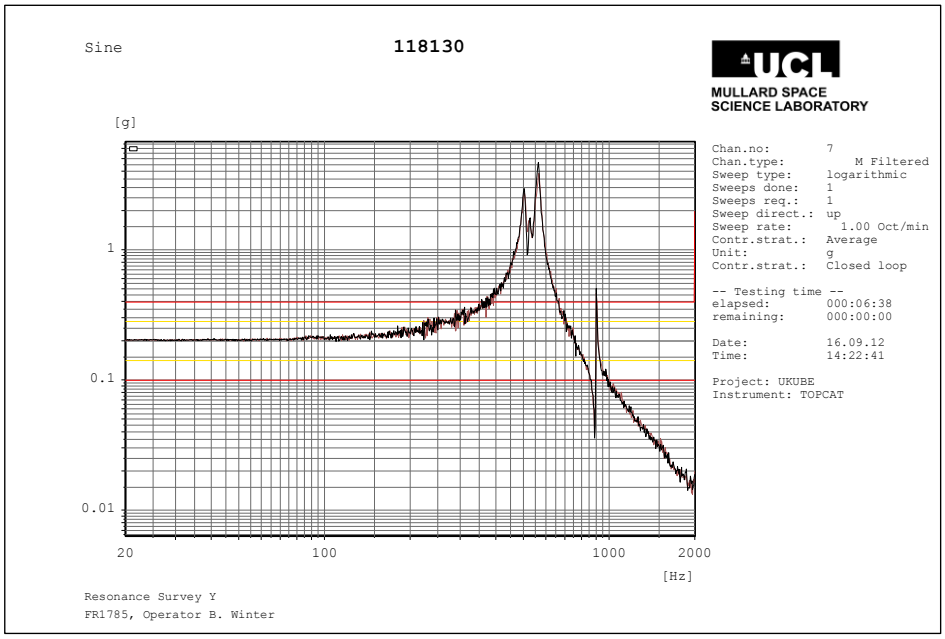

No shifts discernible, supporting the idea that the minor frequency shifts we saw during the previous axis after the random vibration run were are result of settling and not evidence of structure degradation.

Z – Axis

	Project	**UKCUBE**					**University of Bath**	
	Model or Serial Number	**NA**						Add model or serial number
	Part/Drawing Number	**NA**						Add drawing number
	Date of manufacture	**?**						
	Mass	**? kg**						
	Z-AXIS						Notes	
	Pre-Test	Date	Time	Input	Units	Check		
1	Mass Measurement			?	kg			
2	Mount on Shaker	16/09/2012	14:49			BW		
3	Visual Inspection	16/09/2012				BW		Basic check to verify hardware looks ok, sensor wiring is secured and tools are removed from shaker and take photos
4	Torques checked	NA			Nm			Angular control, glue locked
5	Electrical Inspection	NA						At least a basic electrical health check
	Sine Sweep	16/09/2012	15:00	FR1786		BW		Add FR number (facility run number) and add to facility log book
6	Control							Check for control (10.1 average)
7	Charge Amplifier					BW		Check it is working and that the filter and integration settings are correct
8	Input Levels			0.2	g	BW		Check max input levels (prevent clipping)
9	Sweep Rate			1	oct/min	BW		
10	Levels					BW		Check Levels are according to spec (sec 19)
11	Test run File		15:14	SineSweep_002		BW		
12	Short Visual					BW		
	Sine Qual	16/09/2012	15:15	FR1787				Add FR number (facility run number) and add to facility log book
13	Control					BW		Check for control (10.1 average)
14	Charge Amplifier					BW		Check it is working and that the filter and integration settings are correct
15	Input Levels					BW		Check max input levels (prevent clipping)
16	Sweep Rate			2	oct/min	BW		
17	Levels			4	g	BW		Check Levels are according to spec (sec 19)
18	Frequency			50	Hz			
19	Test run File		15:21	SineQualTest Z-Axis_004				
20	Short Visual							
	Sine Sweep	16/09/2012	15:21	FR1788		BW		Add FR number (facility run number) and add to facility log book
21	Control							Check for control (10.1 average)
22	Charge Amplifier					BW		Check it is working and that the filter and integration settings are correct
23	Input Levels			0.2	g	BW		Check max input levels (prevent clipping)
24	Sweep Rate			1	oct/min	BW		
25	Levels					BW		Check Levels are according to spec (sec 19)
26	Test run File		15:31	SineSweep_001		BW		
27	Short Visual					BW		
	Sine Burst	16/09/2012		FR1789				Add FR number (facility run number) and add to facility log book
28	Control							Check for average control
29	Charge Amplifier							Check it is working and that the filter and integration settings are correct
30	Input Levels							Check max input levels (prevent clipping)
31	Sweep Rate			0.8	oct/min			Check sweep rate according to spec
32	Levels			15	g			Check Levels are according to spec
33	Test run File		15:36	Sine Burst_002				
34	Short Visual							
	Sine Sweep	16/09/2012	15:37	FR1788		BW		Add FR number (facility run number) and add to facility log book
35	Control							Check for control (10.1 average)
36	Charge Amplifier					BW		Check it is working and that the filter and integration settings are correct
37	Input Levels			0.2	g	BW		Check max input levels (prevent clipping)
38	Sweep Rate			1	oct/min	BW		
39	Levels					BW		Check Levels are according to spec (sec 19)
40	Test run File		15:45	SineSweep_003		BW		
41	Short Visual					BW		
	Random Qual	16/09/2012	15:46	FR1784				Add FR number (facility run number) and add to facility log book
42	Control					BW		Check for average control
43	Charge Amplifier					BW		
43	Channel Input Levels					BW		
44	Duration			120	sec	BW		
45	Levels			14.1	g-rms	BW		
46	Test run File		15:50	RandomTest Qual Z-Axis_001		BW		
47	Short Visual					BW		
	Sine Sweep	16/09/2012		FR1785		BW		Add FR number (facility run number) and add to facility log book
48	Control							Check for control (10.1 average)
49	Charge Amplifier					BW		Check it is working and that the filter and integration settings are correct
50	Input Levels			0.2	g	BW		Check max input levels (prevent clipping)
51	Sweep Rate			1	oct/min	BW		
52	Levels					BW		Check Levels are according to spec (sec 19)
53	Test run File		16:03	SineSweep_004		BW		
54	Short Visual					BW		

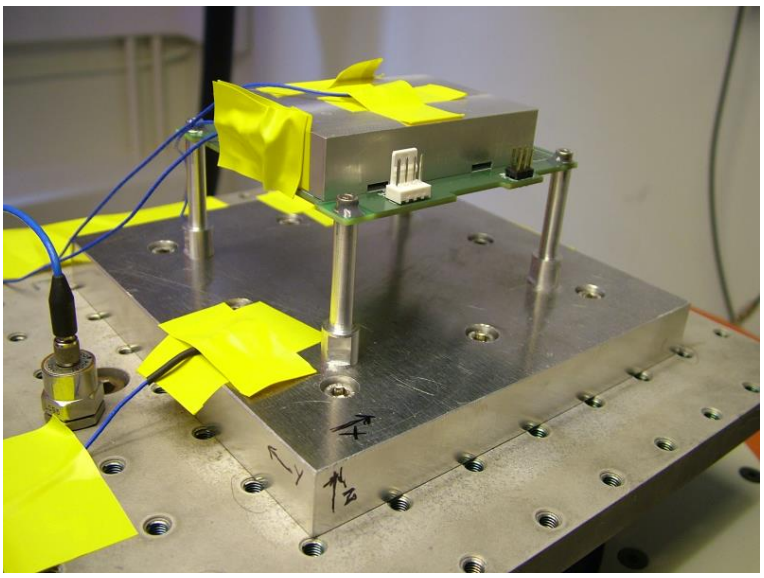

Z axis configuration

Initial sine survey

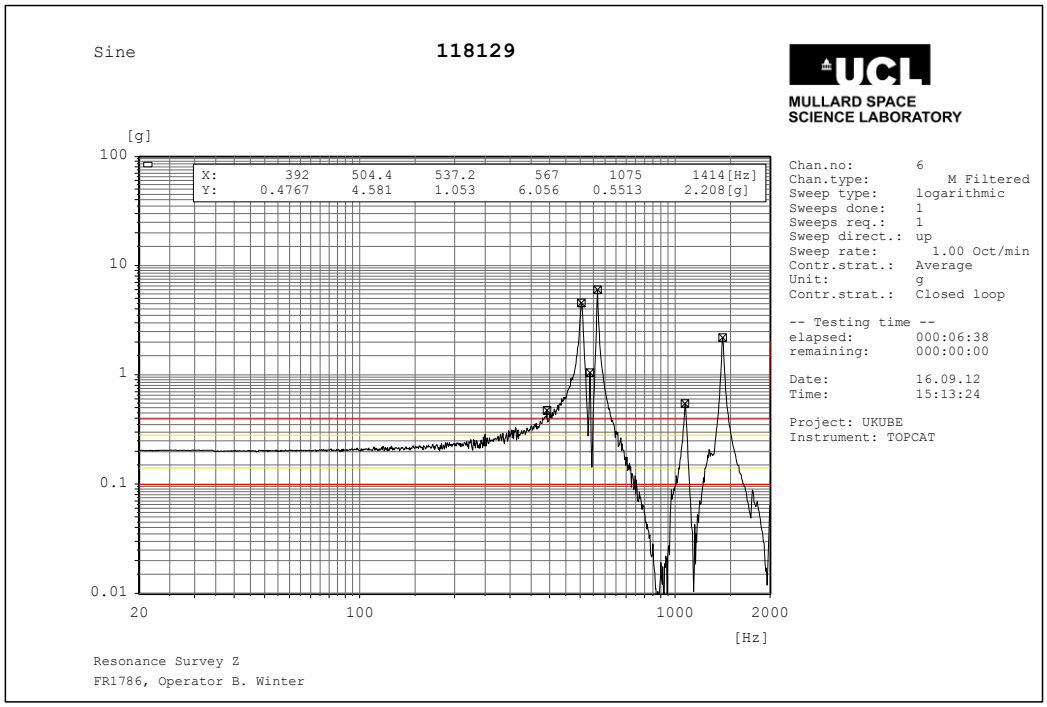

C:\M+P Tests\2012-09-16 TOPCAT\Z AXIS\SineSweep_002.rsn

Sine Qualification

C:\M+P Tests\2012-09-16 TOPCAT\Z AXIS\SineQualTest Z-Axis_004.rsn

Sine survey comparison (Pre-Post Sine Qualification)

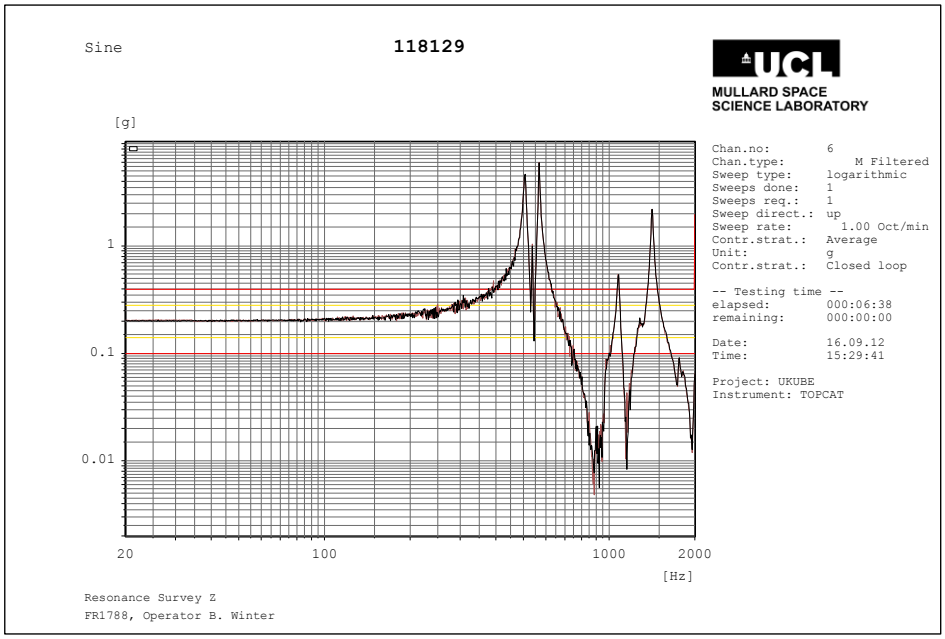

C:\M+P Tests\2012-09-16 TOPCAT\Z AXIS\SineSweep_001.rsn

Sine Burst

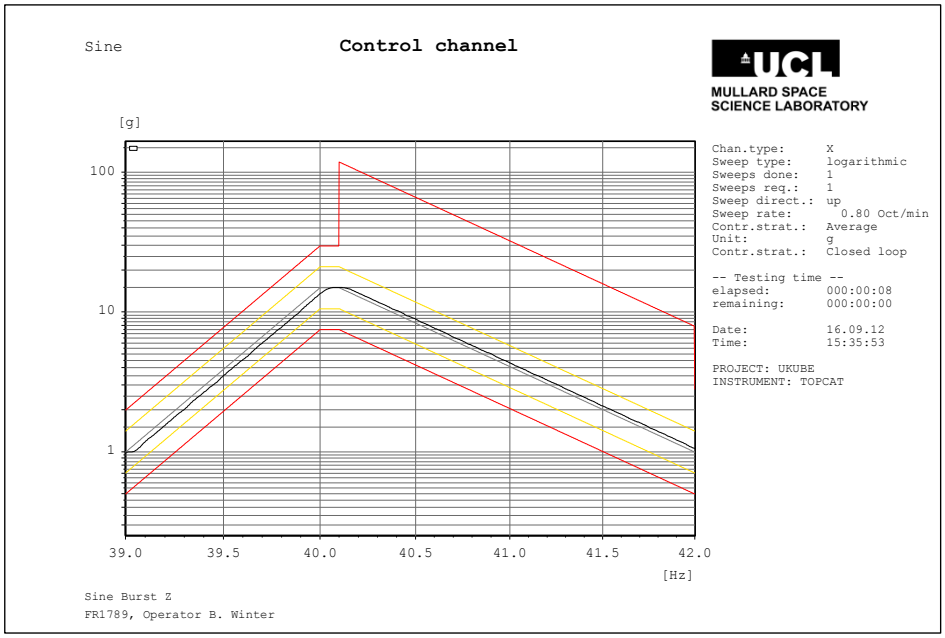

C:\M+P Tests\2012-09-16 TOPCAT\Z AXIS\Sine Burst_002.rsn

Sine survey comparison (Pre-Post Sine Burst)

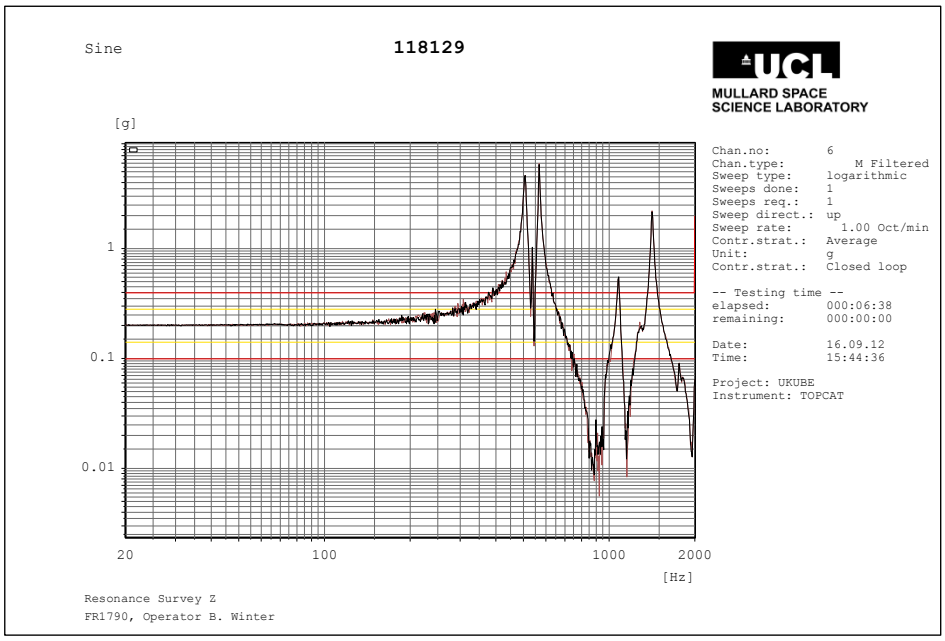

C:\M+P Tests\2012-09-16 TOPCAT\Z AXIS\SineSweep_003.rsn

Random Qualification

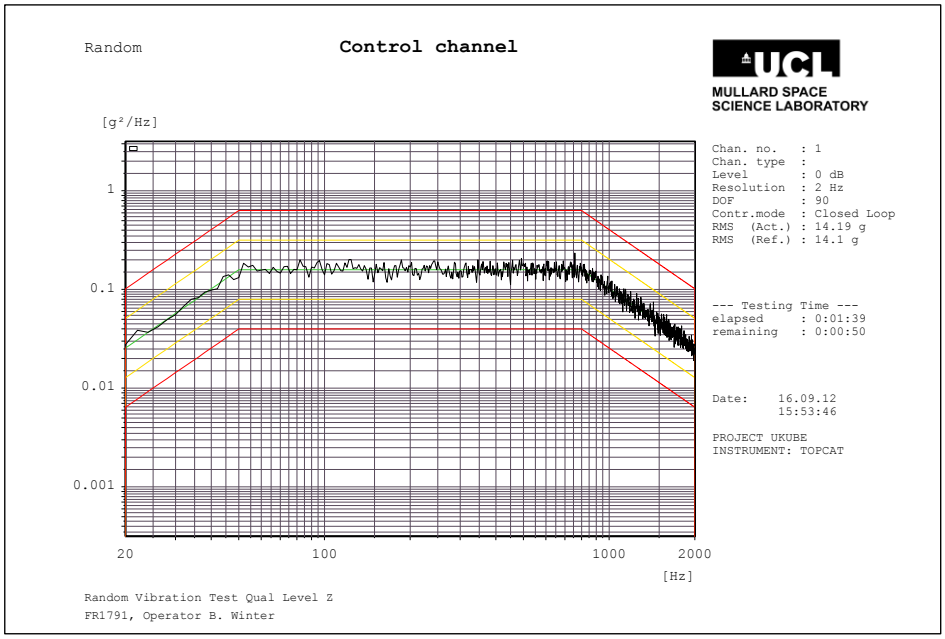

C:\M+P Tests\2012-09-16 TOPCAT\Z AXIS\RandomTest Qual Z-Axis.trn

Sine survey comparison (Pre-Post Axis)

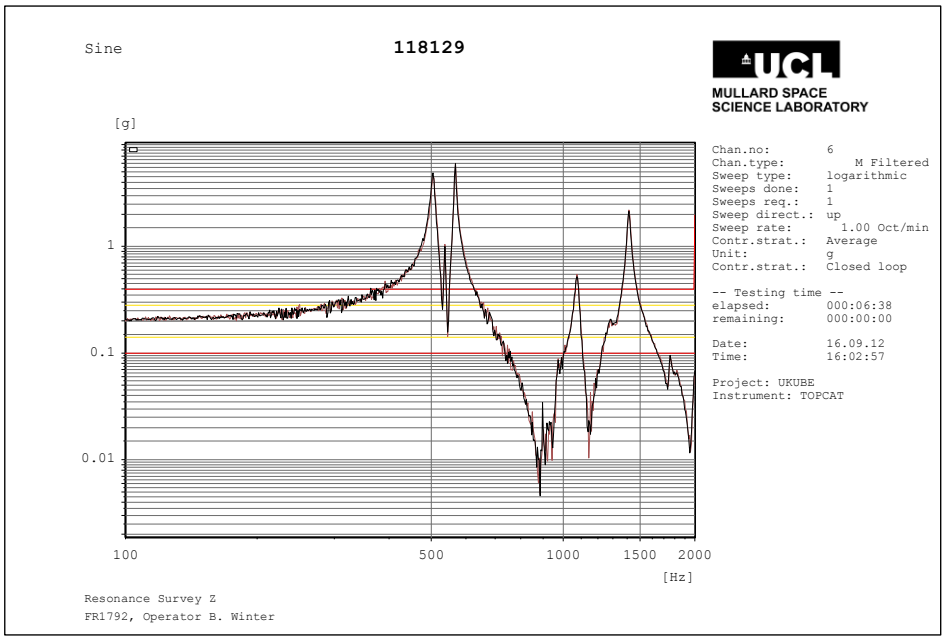

C:\M+P Tests\2012-09-16 TOPCAT\Z AXIS\SineSweep_004.rsn

After the vibration test a functional test was performed and all was found to be in order. On Monday morning the 17th of September 2012 the PCB was removed from the shaker at 09:30 to be further cleaned prior to thermal vacuum testing later in the week.

Conclusions

The requirements as outlined in section 5 were met for the TOPCAT instrument, excluding the antenna.

A2.2 Thermal/Vacuum Test Results

Table A2.1 Thermal/vacuum test report.

18/09/12 11:00	TOPCAT installed in MSC1, wrapped in 10 layers of MLI. 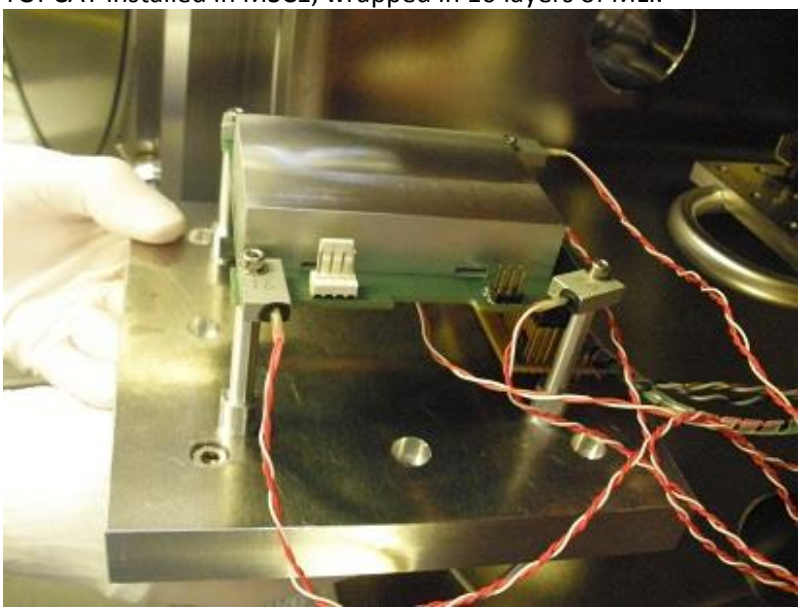 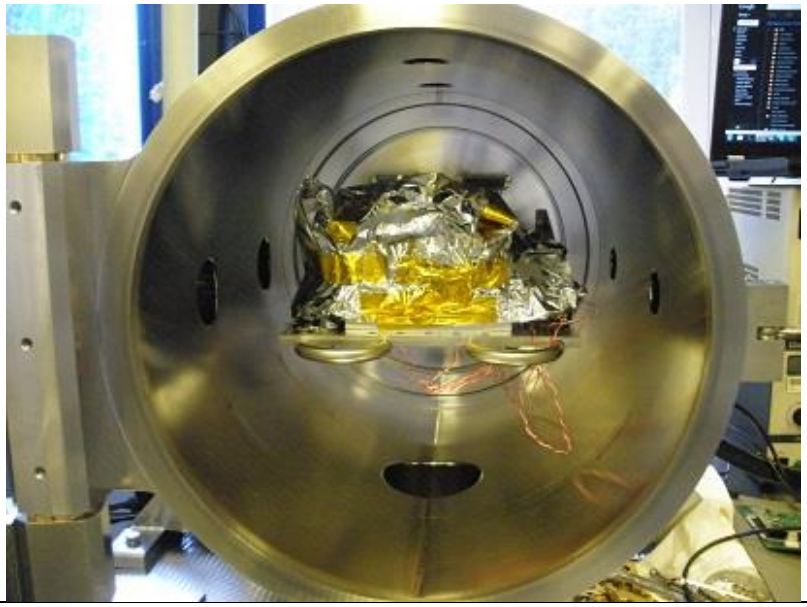	AJM
18/09/12 14:20	Scroll pump started PRT 15 on plate PRTs 14, 16, 17 and 18 on topcat pillars. These appear to be channel 3, 5, 6 and 7 on the data logger.	AJM
18/09/12 14:43	P = 8.5mBar Turbo pump switched on	AJM
18/09/12 15:08	P = 6.2e-5mBar Functional check performed under vacuum conditions : 5V – 80mA; 8V – 170-230mA; 3.3V – 1mA; Auto mode functions successfully. Manual mode used to test EEPROM functionality. **NB: 3.3V->5.7V boost converter not checked due to setup. Need to test post-T/V cycling** Ambient temperature = 20°C	TSPJ

18/09/12 15:28	TCS set to 73°C for hot non-op soak	AJM
19/09/12 08:00	P = 1.0E-5 mBar CH1 = 73.55°C CH2 = 69.68°C CH3 = 67.88°C CH4 = 69.42°C CH5 = 64.52°C CH6 = 65.30°C CH7 = 67.88°C TCS set to 58°C for hot op soak	AJM
19/09/12 08:57	P = 6.5E-6 mBar CH1 = 57.62°C CH2 = 55.32°C CH3 = 61.20°C CH4 = 57.87°C CH5 = 59.67°C CH6 = 60.18°C CH7 = 61.46°C Start of 55°C soak	AJM
19/09/12 09:28	P = 5.0E-6 mBar CH1 = 57.87°C CH2 = 54.55°C CH3 = 56.60°C CH4 = 55.32°C CH5 = 55.06°C CH6 = 55.32°C CH7 = 56.60°C	AJM
19/09/12 09:39	P = 5.1e-6mBar Functional check performed: 5V – 70mA; 8.1V – 175-230mA; 3.3V – 1mA Auto mode functions successfully. Manual mode used to test EEPROM functionality – successful. 10min continuous operation (manual) conducted – successful. **NB: 3.3V->5.7V boost converter not checked due to setup. Need to test post-T/V cycling** Temperature = 57.5°C	TSPJ
19/09/12 10:33	P = 5.9E-6 mBar CH1 = 58.13°C CH2 = 55.32°C CH3 = 56.60°C CH4 = 55.57°C CH5 = 57.62°C CH6 = 56.08°C CH7 = 56.34°C	AJM
19/09/12 11:23	TCS set to -38°C for cold non-op soak	AJM
19/09/12 12:39	P = 8.2E-7 mBar CH1 = 11.81°C CH2 = 4.25°C CH3 = 36.41°C	AJM

	CH4 = 14.34°C CH5 = 38.95°C CH6 = 37.42°C CH7 = 35.90°C	
19/09/12 13:20	P = 1.5E-6 mBar CH1 = -16.13°C CH2 = -23.12°C CH3 = 7.53°C CH4 = -12.38°C CH5 = 13.83°C CH6 = 12.06°C CH7 = 7.27°C It doesn't look like we will be able to fit the cold non-op and cold op in today so I will set the TCS for -23°C for the cold op soak, and after the tests are complete, set the chamber to -38°C again for the cold non-op soak overnight.	AJM
19/09/12 13:57	P = 8.6E-7 mBar CH1 = -12.38°C CH2 = -15.63°C CH3 = -4.07°C CH4 = -9.61°C CH5 = 1.73°C CH6 = -0.03°C CH7 = -4.57°C	AJM
19/09/2012 14:30	Changed set point to -60 in order to provoke a reaction from the control.	BW/AJM
19/09/2012 14:34	Setpoint now back at -30. We didn't see a significant response. Pipe work at back of the chamber not really cold, It appears no LN2 is flowing, mostly GN2.	BW/AJM
14:36	LN2 appears to flow again. Pipes are freezing up	BW/AJM
19/09/12 15:39	P = 7.0E-7 mBar CH1 = -27.61°C CH2 = -30.35°C CH3 = --20.11°C CH4 = --25.36°C CH5 = -14.62°C CH6 = -15.37°C CH7 = -20.11°C Start of cold operational soak	AJM
19/09/12 15:52	P = 7e-7mBar Functional check performed: 5V – 90mA; 8.1V – 175-210mA; 3.3V – 1mA Auto mode functions successfully. Manual mode used to test EEPROM functionality – successful. 10min continuous operation (manual) conducted – successful. **NB: 3.3V->5.7V boost converter not checked due to setup. Need to test post-T/V cycling** Temperature = -21.36°C	TSPJ

19/09/12 16:22	P = 7.4E-7 mBar CH1 = -22.87°C CH2 = -23.37°C CH3 = -19.12°C CH4 = -21.37°C CH5 = -12.38°C CH6 = -13.88°C CH7 = -19.38°C **End of cold op soak.** **TCS set to 58°C for hot op soak.**	AJM
20/09/12 09:58	P = 3.2E-6 mBar CH1 = 58.64°C,CH2 = 55.82°C, **CH3 = 54.80°C,** CH4 = 55.31°C, **CH5 = 52.75°C, CH6 = 52.75°C, CH7 = 54.55°C** **TCS @ 58°C set to -45°C**	VMB
20/09/12 11:35	P = 3.4E-7 mBar CH1 = -11.62°C,CH2 = -19.87°C, **CH3 = 20.42°C,** CH4 = -9.10°C, **CH5 = 25.24°C, CH6 = 23.72°C, CH7 = 19.66°C** **TCS @ -45°C**	VMB
20/09/12 13:03	P = 5.1E-7 mBar CH1 = -30.60°C,CH2 = -34.34°C, **CH3 = -18.86°C,** CH4 = -28.35°C, **CH5 =-12.11°C, CH6 = -13.61°C, CH7 = -19.11°C** **TCS @ -45°C**	VMB
20/09/12 14:16	P = 4.7E-7 mBar CH1 = -37.10°C,CH2 = -39.59°C, **CH3 = -30.11°C,** CH4 = -34.60°C, **CH5 =-24.36°C, CH6 = -24.62°C, CH7 = -30.36°C** **TCS @ -45°C set to -43°C**	

20/09/12 15:54	P = 4.7E-7 mBar CH1 = -38.86°C,CH2 = -40.59°C, **CH3 = -35.12°C,** CH4 = -37.11°C, **CH5 =-30.12°C, CH6 = -29.62°C, CH7 = -34.87°C** **TCS @ -43°C** **Start of cold non-operational soak**	VMB
20/09/12 16:27	P = 4.6E-7 mBar CH1 = -39.84°C,CH2 = -40.83°C, **CH3 = -36.10°C,** CH4 = -37.60°C, **CH5 =-31.11°C, CH6 = -30.86°C, CH7 = -35.85°C** **TCS @ -43°C set to -28°C** **End of cold non-operational soak**	VMB
20/09/12 17:30	P = 4.9E-7 mBar CH1 = -31.86°C,CH2 = -30.86°C, **CH3 = -32.36°C,** CH4 = -30.61°C, **CH5 =-28.61°C, CH6 = -28.11°C, CH7 = -32.36°C** **TCS @ -28°C set to -20°C**	VMB
20/09/12 18:05	P=5.1E-7mBar CH1 = -24.12°C,CH2 = -24.12°C, **CH3 = -27.86°C,** CH4 =-24.62°C, **CH5 =-25.11°C, CH6 = -24.86°C, CH7 = -27.86°C** **TCS @ -20°C set to 58°C**	VMB
21/09/12 08:11	P = 2.8E-6 mBar CH1 = 58.64°C,CH2 = 56.08°C, **CH3 = 54.55°C,** CH4 = 55.57°C, **CH5 = 52.50°C, CH6 = 52.76°C, CH7 = 54.80°C** TCS set to -35°C for transition to cold op soak at -20°C	AJM
21/09/12 13:04	P = 4.2E-7 mBar CH1 = -29.12°C,CH2 = -30.61°C, **CH3 = -23.87°C,** CH4 = -26.87°C, **CH5 = -19.12°C, CH6 = -19.38°C, CH7 = -23.87°C** TCS set to -28°C	AJM

21/09/12 14:12	P = 4.4E-7 mBar TCS set to 58° for transition to hot soak	AJM
22/09/12 09:20	P=2.3E-6 mBar. CH1 = 58.91°C,CH2 = 55.84°C, **CH3 = 54.56°C,** CH4 = 55.84°C, **CH5 = 52.77°C, CH6 = 52.77°C, CH7 = 54.82°C** **End of hot soak, cycle 3** **TCS set to -28, start transition to cold soak cycle 3.**	ADR
23/09/12 09:20	P=3.0E-7 mBar CH1 = -26.60°C,CH2 = -27.60°C, **CH3 = -24.85°C,** CH4 = -25.10°C, **CH5 = -21.36°C, CH6 = -21.36°C, CH7 = -24.60°C** **End of cold soak, TCS set to +58°C**	ADR
24/09/12 08:47	P=1.5E-6 mBar CH1 = 59.66°C,CH2 = 55.06°C, **CH3 = 47.89°C,** CH4 = 54.80°C, **CH5 = 43.55°C, CH6 = 44.82°C, CH7 = 48.41°C**	ADR
24/09/12 11:08	P = 2.2e-6mBar Functional check performed: 5V – 70mA; 8.1V – 170-200mA; 3.3V – 1mA Auto mode functions successfully. Manual mode used to test EEPROM functionality – successful. 10min continuous operation (manual) conducted – successful. **NB: 3.3V->5.7V boost converter not checked due to setup. Need to test post-T/V cycling** Temperature = 54.58°C (CH3)	TSPJ

24/09/12 11:34	P = 2.8E-6 mBar TCS set to -50°C to ensure that the instrument reaches cold soak in good time.	AJM
24/09/12 12:03	P=2.3E-7 mBar CH1 = 11.82°C,CH2 = 4.77°C, **CH3 = 50.98°C,** CH4 = 8.29°C, **CH5 = 51.24°C, CH6 = 50.47°C, CH7 = 50.22°C** TCS set to -35°C	AJM
24/09/12 13:20	P=3.8E-7 mBar CH1 = -13.62°C,CH2 = -17.87°C, **CH3 = 2.24°C,** CH4 = -10.85°C, **CH5 = 8.29°C, CH6 = 6.28°C, CH7 = 1.49°C** TCS set to -40°C	AJM
24/09/12 14:10	P=2.9E-7 mBar CH1 = -24.86°C,CH2 = -28.11°C, **CH3 = -13.87°C,** CH4 = -22.11°C, **CH5 = -7.83°C, CH6 = -9.09°C, CH7 = -14.67°C**	AJM
24/09/12 14:48	P=2.7E-7 mBar CH1 = -29.12°C,CH2 = -31.36°C, **CH3 = -20.38°C,** CH4 = -26.62°C, **CH5 = -14.88°C, CH6 = -15.88°C, CH7 = -20.62°C** TCS set to -28°C	AJM
24/09/12 15:15	P = 2.2e-6mBar Functional check performed: 5V – 100mA; 8.1V – 170-200mA; 3.3V – 1mA Auto mode functions successfully. Manual mode used to test EEPROM functionality – successful. Payload restart was seen when BATV was switched on. Repeat of the power on sequence did not restart the payload. 10min continuous operation (manual) conducted – successful. **NB: 3.3V->5.7V boost converter not checked due to setup. Need**	TSPJ

	to test post-T/V cycling Temperature = -22.26°C (CH3)	
24/09/12 15:42	P=3.0E-7 mBar CH1 = -23.11°C,CH2 = -23.11°C, **CH3 = -19.36°C,** CH4 = -21.61°C, **CH5 = -12.62°C, CH6 = -14.62°C, CH7 = -20.36°C** TCS set to 20°C for venting tomorrow	AJM
25/09/12 09:48	P = 5.7e-7mBar (in vacuum) Functional check performed: 5V – 75mA; 8.1V – 160-200mA; 3.3V – 1mA Auto mode functions successfully. Manual mode used to test EEPROM functionality – successful. 10min continuous operation (manual) conducted – successful. **NB: 3.3V->5.7V boost converter not checked due to setup. Need to test post-T/V cycling** Temperature = 21.72°C (CH3)	TSPJ
25/09/12 10:25	Chamber vented and TOPCAT removed Logging halted	AJM
25/09/12 10:27	P = 1000mBar Functional check performed: 5V – 80mA; 8.1V – 170-200mA; 3.3V – 1mA Auto mode functions successfully. Manual mode used to test EEPROM functionality – successful. 10min continuous operation (manual) conducted – successful. **NB: 3.3V->5.7V boost converter Vout checked. Output is 5.7V as expected.** Temperature = -22.26°C (CH3)	TSPJ

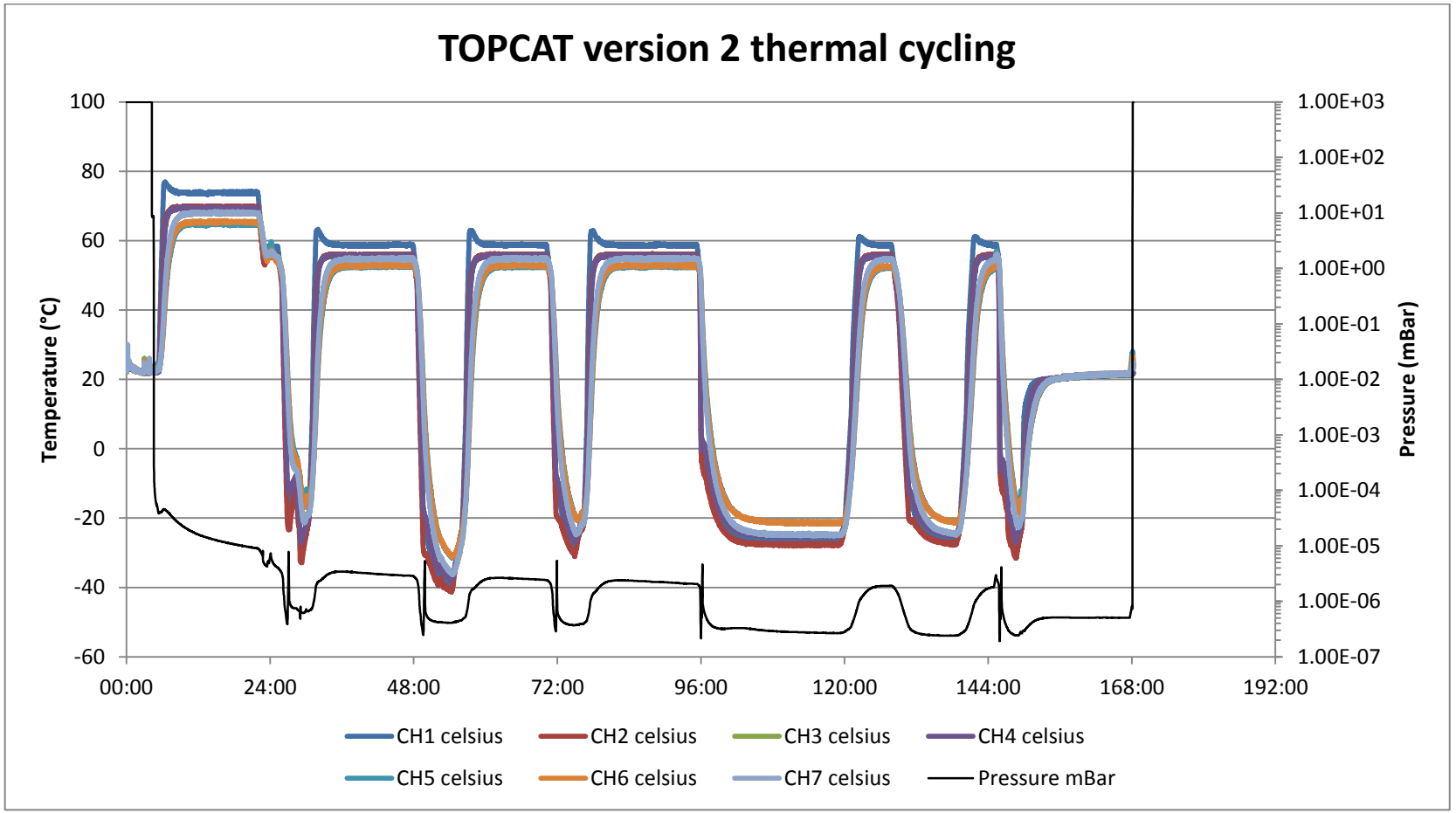
TOPCAT version 2 thermal cycling
Temperature (°C)
100
80
60
40
20
0
-20
-40
-60
Pressure (mBar)
1.00E+03
1.00E+02
1.00E+01
1.00E+00
1.00E-01
1.00E-02
1.00E-03
1.00E-04
1.00E-05
1.00E-06
1.00E-07
00:00
24:00
48:00
72:00
96:00
120:00
144:00
168:00
192:00
CH1 celsius
CH2 celsius
CH3 celsius
CH4 celsius
CH5 celsius
CH6 celsius
CH7 celsius
Pressure mBar